Fast One-dimensional Finite Element Approximation of Geophysical Measurements

Mostafa Shahriari

Supervised by *David Pardo* and *Shaaban A. Bakr*

October 1, 2018

basque center for applied mathematics

EXCELENCIA SEVERO OCHOA

Fast One-dimensional Finite Element Approximation of Geophysical Measurements

Mostafa Shahriari

Supervised by *David Pardo* and *Shaaban A. Bakr*

October 1, 2018

eman ta zabal zazu

Universidad del País Vasco

Euskal Herriko Unibertsitatea

This dissertation has been possible with the support of the Project of the Spanish Ministry of Economy and Competitiveness with reference MTM2016-76329-R (AEI/FEDER, EU), and MTM2016-81697-ERC/AEI, the BCAM "Severo Ochoa" accreditations of excellence SEV-2013-0323 and SEV-2018-0718, and the Basque Government through the BERC 2014-2017 program and the Consolidated Research Group Grant IT649-13 on "Mathematical Modeling, Simulation, and Industrial Applications (M2SI)"; the European Union's Horizon 2020 research and innovation program under the Marie Sklodowska-Curie grant agreements No 644602 and 777778.

Acknowledgements

First of all, I would like to offer my eternal gratitude to Professor David Pardo for his genuine support and help during all of my Ph.D. His excellent guidance was of paramount importance to create this scientific work and help me grow personally and professionally. I should also reckon his admirable patience. After four years, I am privileged to call him my mentor and my friend.

I also would like to give a special thanks to Dr. Shaaban A. Bakr. He was always available to help me, even with the shortest notice. In particular, at the beginning of the work, he helped me to learn faster and move in the right directions. I am sincerely grateful for his support and guidance during these four years.

I am deeply thankful to Dr. Angel Rodríguez-Rozas for giving me fantastic advice during the work, especially in the area of scientific programming. Additionally, his forever friendship is the most important outcome of this collaboration which I cherish dearly. I also thank my good friends Dr. Sergio Rojas and Dr. Théophile Chaumont-Frelet for the great discussions we had, and for the help they gave me in the theoretical parts of my work.

I wish to offer a special thank to Professor Ignacio Muga for hosting me at Instituto de Matemáticas at Pontificia Universidad Católica de Chile for three months, and for his help during this work. His sincere friendship and the great discussions we had made my trip much more enjoyable. I would also like to thank Professor Maciej Paszynski for hosting me for two weeks at AGH University. The times we shared made the trip more productive and adventurous.

I wish to thank all the colleagues from the Mathematical Modeling, Simulation, and Industrial Applications (M^2SI) group for their friendship, support, and help. I forever hold dear the friendship we achieved during these years, and the great times we shared during this long journey.

I also like to thank the staff in BCAM for making all the effort to make our lives easier. They do their best to make every process as smooth as possible and give all the support we need. All their help made it easier for me to focus entirely on my work.

I need to thank my parents whom their support and sacrifices made me who I am today. Last but not least, I want to give my forever lasting gratitude to my beautiful and intelligent wife for her unconditional love and support. Her

support made my success possible and gave me hope during difficult times. During this journey, she was always my rock and my inspiration. I love you forever.

Abstracts

There exist a wide variety of geophysical prospection methods. In this work, we focus on resistivity methods. We categorize these resistivity prospection methods according to their acquisition location as (a) *on surface*, such as the ones obtained using Controlled Source Electromagnetics (CSEM) and magnetotelluric, and (b) *in the borehole*, such as the ones obtained using Logging-While-Drilling (LWD) devices. LWD devices are useful both for reservoir characterization and geosteering purposes, which is the act of adjusting the tool direction to travel within a specific zone.

When inverting LWD resistivity measurements, it is a common practice to consider a one-dimensional (1D) layered media to reduce the problem dimensionality using a Hankel transform. Using orthogonality of Bessel functions, we arrive at a system of Ordinary Differential Equations (ODEs); one system of ODEs per Hankel mode. The dimensionality of the resulting problem is referred to as 1.5D since the computational cost to resolve it is in between that needed to solve a 1D problem and a 2D problem. When material properties (namely, resistivity, permittivity, and magnetic permeability) are piecewise-constant, we can solve the resulting ODEs either (a) analytically, which leads to a so-called semi-analytic method after performing a numerical inverse Hankel transform, or (b) numerically. Semi-analytic methods are faster, but they also have important limitations, for example, (a) the analytical solution can only account for piecewise constant material properties, and other resistivity distributions cannot be solved analytically, which prevents to accurately model, for example, an Oil-Water Transition (OWT) zone when fluids are considered to be immiscible; (b) a specific set of cumbersome formulas has to be derived for each physical process (e.g., electromagnetism, elasticity, etc.), anisotropy type, etc.; (c) analytical derivatives of specific models (e.g., cross-bedded formations, or derivatives with respect to the bed boundary positions) are often difficult to obtain and have not been published to the best of our knowledge.

In view of the above limitations, we propose to solve our forward problems using a numerical solver. A traditional Finite Element Method (FEM) is slow, which makes it unfeasible for our application. To achieve high performance, we developed a multiscale FEM that pre-computes a set of optimal local basis functions that are used at all logging positions. The resulting method is slow when compared to a semi-analytic approach for a single logging position, but it

becomes highly competitive for a large number of logging positions, as needed for LWD geosteering applications. Moreover, we can compute the derivatives using an adjoint state method at almost zero additional cost in time. We describe an adjoint-based formulation for computing the derivatives of the electromagnetic fields with respect to the bed boundary positions. The key idea to obtain this adjoint-based formulation is to separate the tangential and normal components of the field, and treat them differently. We then apply this method to a 1.5D borehole resistivity problem. Moreover, we compute the adjoint-state formulation to compute the derivative of the magnetic field with respect to the resistivity value of each layer. We verify the accuracy of our formulations via synthetic examples.

When simulating borehole resistivity measurements in a reservoir, it is common to consider an Oil-Water Contact (OWC) planar interface. However, this consideration can lead to an unrealistic model since, in the presence of capillary pressure, the mix of two immiscible fluids (oil and water) often appears as an OWT zone. These transition zones may be large in the vertical direction (20 meters or above), and in context of geosteering, an efficient method to simulate an OWT zone can maximize the production of an oil reservoir. In this work, we prove that by using our proposed 1.5D numerical method, we can easily consider arbitrary resistivity distributions in the vertical direction, as it occurs in an OWT zone. Numerical results on synthetic examples demonstrate significant differences between the results recorded by a geosteering device when considering a realistic OWT zone vs. an OWC sharp interface.

As an additional piece of work of this Ph.D. Dissertation, we explore the possibility of using a Deep Neural Network (DNN) to perform a rapid inversion of borehole resistivity measurements. Herein, we build a DNN that approximates the following inverse problem: given a set of borehole resistivity measurements, the DNN is designed to deliver a physically meaningful and data-consistent piecewise one-dimensional layered model of the surrounding subsurface. Once the DNN is built, the actual inversion of the field measurements is efficiently performed in real time. We illustrate the performance of a DNN designed to invert LWD measurements acquired on high-angle wells via synthetic examples.

Resumen

Las mediciones de resistividad geofísica se utilizan para mapear el subsuelo, explorar depósitos de nuevos hidrocarburos y maximizar la producción de los ya existentes. Categorizamos las mediciones de resistividad existentes de acuerdo a su zona de adquisición: (1) *en la superficie*, como aquellas obtenidas usando un método de fuentes controladas (CSEM por sus siglas en inglés) [8, 76, 19, 64, 40] y Magnetotelúrica [56, 5]; y (2) *mediciones de resistividad de pozo*, por ejemplo, aquellas adquiridas usando herramientas petrolíferas de medición a la vez que se perfora (LWD por sus siglas en inglés) [65, 23, 80, 38, 22, 74, 10, 13, 16, 20, 21, 75], incluidos los denominados dispositivos de registro profundo y extra profundo [68, 13].

LWD es una tecnología que incorpora herramientas de registro de pozos (por ejemplo, rayos gamma, resistividad, densidad y sónicos) y registra mediciones y las transmite a la superficie para su interpretación en tiempo real mientras se perfora el pozo [65, 63, 4, 9, 45, 87, 43, 28]. Estas herramientas proporcionan dos elementos de información: (a) datos en tiempo real, que se procesan en el campo durante la perforación, y (b) datos que se almacenan en el dispositivo para procesarlos después de extraerlo del pozo petrolífero. Se utilizan datos en tiempo real para evaluar la formación de subsuelo y realizar geonavegación, que es el acto de ajustar la inclinación y el ángulo acimutal del pozo para alcanzar un objetivo geológico [65, 63, 4, 9, 45, 87, 43].

La primera herramienta LWD comercial apareció en la década de los setenta. Se usaron para la evaluación de formaciones, especialmente en pozos de alto ángulo. Hoy en día, los LWDs se utilizan tanto para la caracterización de subsuelo [63, 4, 9] como para las aplicaciones de geonavegación [45, 87, 43]. Los instrumentos modernos de resistividad de pozo convencionales pueden medir los nueve acoplamientos del campo magnético, a saber xx, xy, xz, yx, yy, yz, zx, zy y zz (la primera letra indica la orientación del transmisor y la segunda indica la orientación del receptor) [80, 22]. Recientemente, se han introducido dispositivos de registro acimutal profundos y extraprofundos como un nuevo tipo de herramienta LWD [10, 13]. Además de mapear la subsuelo, nos ayudan a seleccionar la trayectoria del pozo correctamente en el depósito de hidrocarburos para aumentar la productividad del mismo [16, 10, 20, 21]. Existen varias diferencias entre los LWD convencionales y los acimutales profundos, por ejemplo, la cantidad de transmisores y receptores, la distancia entre ellos,

que son significativamente mayores en configuraciones acimutales profundas, y la presencia de receptores inclinados que nos ayudan en la navegación del subsuelo. La principal ventaja de los instrumentos de resistividad profundos y extraprofundos en comparación con los dispositivos LWD convencionales es que su profundidad de investigación es significativamente más larga, lo que permite realizar geonavegación sin cruzar una roca saturada de agua [13, 10].

Matemáticamente, identificamos dos problemas diferentes al interpretar mediciones geofísicas de pozo:

Problema directo: Dado un transmisor t y propiedades del material conocidas (en nuestro caso, una distribución de resistividad y las características geométricas de los medios $\mathbf{P}$), el problema directo proporciona el campo magnético (o una cantidad postprocesada) indicada por $\mathbf{M}$ (medida) en un receptor r. Denotando por $\mathbf{T}$ a una trayectoria de pozo compuesta de varias ubicaciones de transmisor y receptor (es decir, $\mathbf{T} = \{(t_i, r_i)\}_{i=1}^{N}$, donde N es el número de mediciones), tenemos:

$$\boldsymbol{\mathcal{M}} = \mathbf{F}(\mathbf{P}; \mathbf{T}), \tag{1}$$

donde $\mathbf{F}$ representa la ecuación diferencial parcial (PDE por sus siglas en inglés) basada en las ecuaciones de Maxwell y las condiciones de contorno que rigen los fenómenos de propagación de ondas electromagnéticas, y $\boldsymbol{\mathcal{M}} = \{\mathbf{M}_i\}_{i=1}^{N}$ es el vector de medidas adquiridas a lo largo de la trayectoria del pozo $\mathbf{T}$ (ver p. ej., [23, 22, 75]).

Problema inverso: Dado un conjunto de mediciones $\boldsymbol{\mathcal{M}}$ obtenidas a lo largo de una trayectoria de registro especificada $\mathbf{T}$, el problema inverso proporciona una distribución subsuperficial del material $\mathbf{P}$ (ver, por ejemplo, [38, 65, 41]). Se desconoce una expresión analítica de la ecuación gobernante $\mathbf{I}$ que relaciona estas variables. No obstante, para mayor comodidad, expresamos este problema como:

$$\mathbf{P} = \mathbf{I}(\boldsymbol{\mathcal{M}}; \mathbf{T}). \tag{2}$$

Un problema de inversión se plantea matemáticamente como uno de minimización. Existen múltiples enfoques en la literatura para resolver tales problemas de minimización. Un método popular es el uso de un algoritmo basado en gradiente (ver, por ejemplo, [77, 79]). Sin embargo, sólo garantizan un mínimo local, que puede estar muy lejos del global. Otra familia de métodos se basa en algoritmos estadísticos (véase, por ejemplo, [77, 79, 83]). Sin embargo, a menudo requieren una gran cantidad de simulaciones, lo que aumenta el tiempo de cálculo. Además, para cada nuevo conjunto de datos de mediciones, es necesario repetir todo el proceso de inversión, que podría ser computacionalmente costoso. Esto ocurre porque ninguno de estos métodos entrega

una aproximación completa de la función **I** en sí misma, sino que la evalúan sobre un conjunto particular de mediciones. Matemáticamente hablando, la función **I** no está bien definida. Para un conjunto dado de parámetros de entrada, puede no tener salida o, como ocurre con mayor frecuencia, puede proporcionar múltiples salidas. Estas bien conocidas propiedades no deseadas de los problemas inversos (ver, por ejemplo, [77, 79]) hacen que sean mucho más difíciles de tratar que los problemas directos. Existen varias téctinas, como la regularización, que ayudan a superar estas dificultades y simplificar la solución de problemas inversos. La incorporación de restricciones no lineales en **I** también es una técnica común para evitar soluciones no físicas (ver, por ejemplo, [77]).

Durante la geonavegación es necesario resolver múltiples problemas inversos en tiempo real [65, 38]. Para maximizar la producción del pozo y minimizar los gastos, necesitamos un método rápido de inversión (interpretación de las mediciones en tiempo real) para realizar dicha geonavegación. Una inversión tridimensional (3D) completa es costosa, lo que la hace a menudo inadecuada para esta aplicación. Sin embargo, dado que la profundidad de la investigación de mediciones de resistividad LWD es limitada en comparación con el espesor esperado de las capas geológicas. Por lo tanto, es común aproximar los modelos subsuperficiales en la proximidad del instrumento de registro con una secuencia de modelos 1D [65, 88]. En un modelo 1D, las propiedades del material varían solamente a lo largo de una dirección espacial.

En presencia de un transmisor puntual 3D, un modelo de formación 1D permite reducir la dimensionalidad del problema a la denominada una dimensión y media (1.5D). Dicha reducción se realiza a través de una transformada de Hankel o de una transformada de Fourier 2D a lo largo de las direcciones sobre las cuales suponemos que las propiedades del material son invariantes (ver p. ej., [75, 22, 53]). Esta aproximación 1.5D también se puede emplear para obtener una distribución de resistividad subsuperficial inicial a partir de mediciones CSEM marinas [78]. Al realizar esta reducción de dimensionalidad, obtenemos un sistema de ecuaciones diferenciales ordinarias (ODEs por sus siglas en inglés) que puede ser resuelto ya sea: (a) analíticamente, considerando un perfil de resistividad constante a trozos, que conduce a un llamado método semi-analítico después de una transformada inversa numérica de Hankel [53, 48, 41, 70, 60], o (b) numéricamente, lo que lleva a un método puramente numérico [23].

A pesar de la alta eficiencia de los métodos semianalíticos, resolver los ODEs analíticamente tiene algunas limitaciones importantes. Por ejemplo, (a) a veces pueden conducir a un mapeo poco realista del subsuelo, ya que tienen que considerar los perfiles de resistividad a trozos constantes. Como resul-

tado, a menudo emplean un contacto de petróleo-agua (OWC por sus siglas en inglés) abrupto, es decir, los modelos pasan de rocas saturadas al 100% con petróleo a otras saturandas al 100% con agua. Sin embargo, en muchos modelos de subsuelos realistas, el OWC a menudo aparece como una zona transición petróleo-agua (OWT por sus siglas en inglés) con un perfil de resistividad variable debido a la presión capilar y la existencia de fluidos inmiscibles (petróleo y agua) [49, 29, 55, 12]. Para modelizar esto con un código semianalítico 1.5D, es necesario aproximar el modelo real en la zona OWT utilizando múltiples capas de resistividad constante, lo que aumenta el costo computacional, la implementación, el error de modelización y la complejidad de la implementación; (b) debe derivarse un conjunto específico de fórmulas complejas para cada proceso físico (por ejemplo, electromagnetismo, elasticidad, etc.) tipo de anisotropía, etc.; (c) las derivadas analíticas de ciertos modelos (por ejemplo, formaciones de capas con anisotropía no vertical, o derivadas con respecto a las posiciones de cada capa del modelo) a menudo son difíciles de obtener [80] y no se han publicado.

También es posible resolver numéricamente los ODEs resultantes. Dicho método numérico también exhibe un costo lineal con respecto al tamaño de discretización, ya que consiste en una secuencia de problemas 1D independientes. Un ejemplo de este enfoque se puede encontrar en [23], donde Davydycheva et al. usan una transformada de Fourier 2D para reducir la dimensión del problema. Luego, emplean un método 1D de diferencias finitas (FDM por sus siglas en inglés) altamente preciso para resolver los ODEs resultantes. Este método es relativamente simple de implementar. Sin embargo, esta metodología combinada requiere un costo computacional que es más de 1000 veces mayor que el observado en métodos semi-analíticos. Esto ocurre debido al elevado número de incógnitas necesarias para discretizar correctamente las ODEs. Si una factorización común de la matriz del sistema basada en una matriz triangular inferior y superior (la denominada factorización LU) fuera precalculada para todas las posiciones de la fuente, la situación empeoraría: se necesitaría un mallado refinado para modelizar correctamente todos los transmisores y dado que el costo de la eliminación gaussiana también es proporcional al tamaño de discretización (como ocurre con la factorización LU), el gran costo computacional requerido para realizar la eliminación gaussiana aumentaría significativamente el costo total del resolvedor. El uso de otras técnicas tradicionales, como un método de elementos finitos (FEM por sus siglas en inglés) (ver, por ejemplo, [25]) para resolver las ODEs resultantes no atenuaría estos problemas. Además, en [23], el uso de una transformada de Fourier 2D presenta otra carga en el rendimiento del resolvedor, ya que el número de ODEs (y el costo total del resolvedor) aumenta cuadráticamente con respecto al número de puntos de

integración de una transformada inversa de Fourier 1D, mientras que en el caso de una transformada de Hankel, el costo sólo crece linealmente con respecto al número de puntos de integración de la transformada inversa de Hankel.

Uno de los objetivos de este trabajo es superar las limitaciones mencionadas tanto de los métodos numéricos existentes como de los semi-analíticos resolviendo cada problema 1D (asociado con cada modo de Hankel) usando un FEM eficiente multiescala. Además, buscamos un método con las siguientes características: (a) que pueda considerar distribuciones de resistividad arbitrarias a lo largo de la dirección 1D (como ocurre en una zona de OWT), y no sólo una distribución constante a trozos como en el caso de métodos semi-analíticos, y (b) que pueda construir derivadas fácil y rápidamente con respecto a las propiedades del material y la posición de los límites de cada capa mediante el uso de una formulación adjunta, para así calcular numéricamente la matriz jacobiana necesaria para el método de inversión de Gauss-Newton sin costo adicional. Además, utilizando un método método multiescala, alcanzamos la alta eficiencia requerida para la aplicación, al tiempo que evitamos las aproximaciones innecesarias del modelo de resistividad en la zona OWT. A pesar de estos avances, actualmente nuestro método propuesto multiescala es más lento que el semi-analítico. Sin embargo, es aproximadamente dos órdenes de magnitud más rápido que un 1D FEM tradicional o un 1D FDM, como el presentado en [23]. Esta aceleración es esencial para aplicaciones prácticas, ya que a menudo se necesitan simular miles de posiciones de registro y estimar millones de derivadas para resolver problemas de inversión en tiempo real en el campo para operaciones de geonavegación. Además, empleamos una transformada de Hankel en lugar de dos transformadas de Fourier. Esto conduce a una formulación matemática más compleja, pero el método resultante muestra un rendimiento superior debido a la menor cantidad de ODEs que deben resolverse.

Otra contribución de esta tesis doctoral se centra en el área de los problemas inversos. Aquí, proponemos un enfoque diferente basado en aproximar la función $\mathbf{I}$ *offline* usando una red neuronal profunda (DNN por sus siglas en inglés), y después, durante la inversión en tiempo real (*online*), evaluamos esta aproximación para cada conjunto de mediciones registradas $\boldsymbol{\mathcal{M}}$.

El primer DNN se publicó en 1965 [39]. El término *Deep Learning* se introdujo en 1986 [24], y más tarde en 2000 [3] para referirse a las redes neuronales que contienen una gran cantidad de capas [54]. Una DNN permite detectar y extraer automáticamente características complejas que pueden estar presentes en un conjunto de datos determinado. Esto no fue posible con las redes neuronales tradicionales. En la última década, los DNNs han demostrado ser útiles en múltiples áreas de conocimiento (incluida la visión por ordenador

[54], reconocimiento de voz [86] y biométrica [11]) para aproximar complejas funciones con propiedades desconocidas. En los últimos años, el uso de algoritmos de aprendizaje automático [15, 6, 46, 32, 7, 14] y Deep Learning [81, 33] en mecánica computacional y geofísica computacional se han convertido en un área activa de estudio. Sin embargo, hasta donde sabemos, los algoritmos de Deep Learning no se han aplicado a la inversión de mediciones de resistividad de pozo, y por lo tanto, sus ventajas y limitaciones no han sido exploradas.

En este trabajo, introducimos el uso de DNNs para resolver problemas inversos y analizamos sus principales características y limitaciones cuando se aplican a la interpretación rápida de mediciones de resistividad de pozo para propósitos de geonavegación. Para simplificar el problema y aumentar la velocidad de los cálculos, nos restringimos a formaciones de la Tierra compuestas por una secuencia de capas 1D, como se describe en [65]. El uso de estos modelos simplificados es común en la industria del petróleo y gas en el contexto de la inversión de las medidas de resistividad de pozo [38, 40].

Contents

List of Figures

Acronyms

PDEs	Partial Differential Equations
ODEs	Ordinary Differential Equations
FDM	Finite Difference Method
FE	Finite Element
FEM	Finite Element Method
HFE	Hankel Finite Element
Ms-HFEM	Multiscale Hankel Finite Element Method
BCs	Boundary Conditions
IFT	Inverse Fourier Transform
IHT	Inverse Hankel Transform
OWC	Oil-Water Contact
OWT	Oil-Water Transition
LWD	Logging-While-Drilling
MT	Magnetotellurics
CSEM	Controlled Source Electromagnetics
TI	Transversaly Isotropic
NN	Neural Network
DNN	Deep Neural Network
RNNs	Recurrent Neural Networks
CNN	Convolutional Neural Network
FC-NN	Fully-Connected Neural Network
BRNNs	Bidirectional Recurrent Neural Networks

1. Introduction

1.1. Motivation

Geophysical resistivity measurements are used to map the subsurface, explore hydrocarbon reservoirs, and maximize the production of the existing ones. We categorize existing resistivity measurements as: (1) *on surface*, such as those obtained using Controlled Source Electromagnetics (CSEM) [8, 76, 19, 64, 40] and Magnetotellurics (MT) [56, 5]; and (2) *borehole resistivity measurements*, for example, those acquired using Logging-While-Drilling (LWD) devices [65, 23, 80, 38, 22, 74, 10, 13, 16, 20, 21, 75], including the so-called deep and extra-deep [68, 13] logging devices.

LWD is a technology that conveys borehole logging tools (e.g., gamma ray, resistivity, density, and sonic) downhole, record measurements, and transmit them to the subsurface for real-time interpretation while the hole is being drilled [65, 63, 4, 9, 45, 87, 43, 28]. These tools provide two pieces of information: (a) real-time data, which is processed on the field while drilling, and (b) data that is stored in the device to process after pulling it out from the hole. We use real-time data to evaluate the formation for geosteering, which is the act of adjusting inclination and azimuth angles of the borehole to reach a geological target (see Figure 1.1) [65, 63, 4, 9, 45, 87, 43].

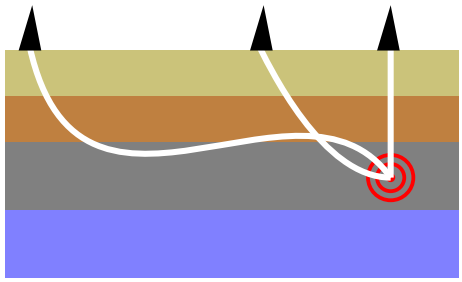

Figure 1.1.: Drawing representing three well trajectories that reach the same target using geosteering techniques.

The first commercial LWD device appeared in the 1970s. It was commercially used for formation evaluation, especially in high-angle wells. Nowadays, LWD devices are employed both for reservoir characterization [63, 4, 9] and

geosteering applications [45, 87, 43]. Modern conventional borehole resistivity instruments can measure all nine couplings of the magnetic field, namely, xx, xy, xz, yx, yy, yz, zx, zy and zz (the first letter indicates the orientation of the transmitter and the second one corresponds to the receiver orientation) [80, 22]. Recently, deep and extra-deep azimuthal logging devices have been introduced as a new type of LWD instruments [10, 13]. Besides, to map the subsurface, they help us to select the well trajectory properly within the hydrocarbon reservoir in order to increase the productivity of the well [16, 10, 20, 21]. There exist several differences between conventional LWD devices and deep azimuthal devices, e.g., the number of transmitters and receivers, the spacings between them, which are significantly more abundant in deep azimuthal configurations, and the presence of tilted receivers which facilitate the reservoir navigation. The main advantage of deep and extra-deep resistivity instruments, in comparison to conventional LWD devices, is their significantly longer depth of investigation, which enables to perform geosteering without crossing a water-saturated rock [13, 10, 52].

From the mathematical point of view, we identify two different problems when interpreting borehole geophysical measurements:

Forward problem: Given a transmitter t and known material properties (in our case, a resistivity distribution and the geometrical characteristics of the media $\mathbf{P}$), the forward problem delivers the magnetic field (or a post-processed quantity of it) denoted by $\mathbf{M}$ (measurement) at a receiver r. Denoting by $\mathbf{T}$ to a well trajectory composed of several transmitter and receiver locations (i.e., $\mathbf{T} = \{(t_i, r_i)\}_{i=1}^{N}$, where N is the number of measurements), we have:

$$\boldsymbol{\mathcal{M}} = \mathbf{F}(\mathbf{P}; \mathbf{T}), \tag{1.1}$$

where $\mathbf{F}$ accounts for the Partial Differential Equations (PDEs) based on Maxwell's equations and boundary conditions governing the electromagnetic wave propagation phenomena, and $\boldsymbol{\mathcal{M}} = \{\mathbf{M}_i\}_{i=1}^{N}$ is the vector of measurements acquired along the well trajectory $\mathbf{T}$ (see, e.g., [23, 22, 75]).

Inverse problem: Given a set of measurements $\boldsymbol{\mathcal{M}}$ obtained over a specified logging trajectory $\mathbf{T}$, the inverse problem delivers a material subsurface distribution $\mathbf{P}$ (see, e.g., [38, 65, 41]). An analytical expression of the governing equation $\mathbf{I}$ that relates these variables is unknown. Nonetheless, for convenience, we express this problem as:

$$\mathbf{P} = \mathbf{I}(\boldsymbol{\mathcal{M}}; \mathbf{T}). \tag{1.2}$$

An inversion problem is mathematically posed as a minimization one. There exist multiple approaches in the literature to solve such minimization problems. One popular method is the use of a gradient-based algorithm (see, e.g., [77, 79]). Unfortunately, they only guarantee a local minimum, which can be far away from the global one. Another family of methods is based on statistical algorithms (see, e.g., [77, 79, 83]). However, they often require a large number of simulations, which increases the computational time. Moreover, for each new dataset of measurements, one needs to repeat the entire inversion process, which could be computationally intensive. This occurs because none of these methods deliver a full approximation of function **I** itself, but rather they evaluate it over a particular set of measurements. Mathematically speaking, the above function **I** is not well-defined. For a given set of input parameters, it may have no output or, as it occurs more frequently, it can provide multiple outputs. These well-known undesirable properties of inverse problems (see, e.g., [77, 79]) make them much more difficult to treat than forward problems. Various techniques such as regularization are intended to overcome these challenges and simplify the solution of inverse problems. The incorporation of nonlinear constraints into **I** is also a common technique to prevent unphysical solutions (see, e.g., [77]).

Figure 1.2 depicts both forward and inverse problems.

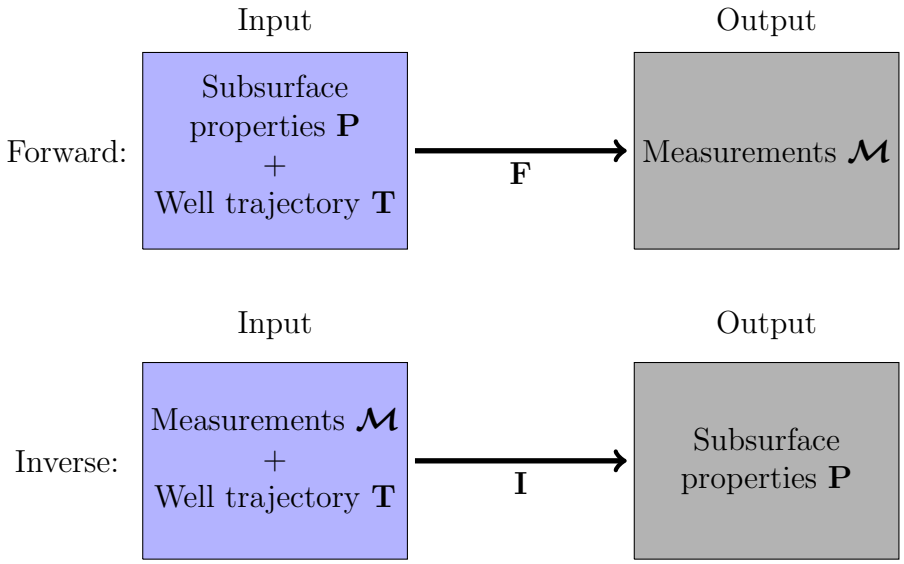

Figure 1.2.: High-level description of a forward and an inverse problem in borehole geophysics.

Geosteering is an expensive process that requires solving multiple inverse problems in real time [65, 38]. To maximize the production from the well

while minimizing the expenses, we need a fast and accurate method to interpret the recorded measurements. A full three-dimensional (3D) inversion is costly, which makes it often unsuitable for this application. However, since the depth of investigation of LWD resistivity measurements is limited compared to the assumed thickness of the geological layers, it is common to approximate the subsurface layers in the proximity of the logging instrument with a sequence of 1D models (see Figures 1.3 and 1.4) [65, 88]. In a 1D model, the material properties vary only along one direction.

(a) Two-dimensional model problem

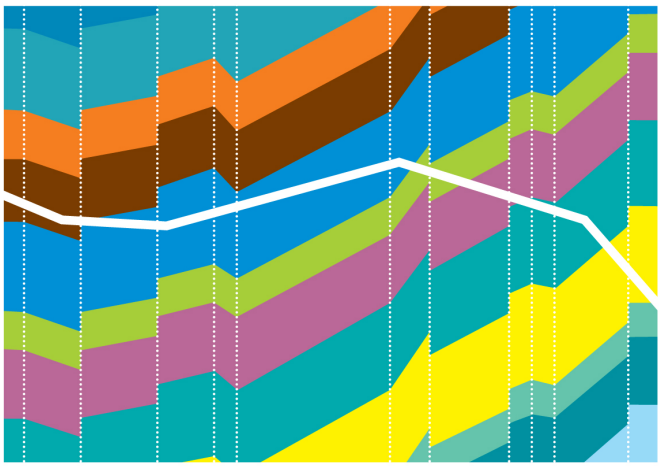

(b) Sequence of one-dimensional problems

Figure 1.3.: Approximating a 2D media using a sequence of 1D media.

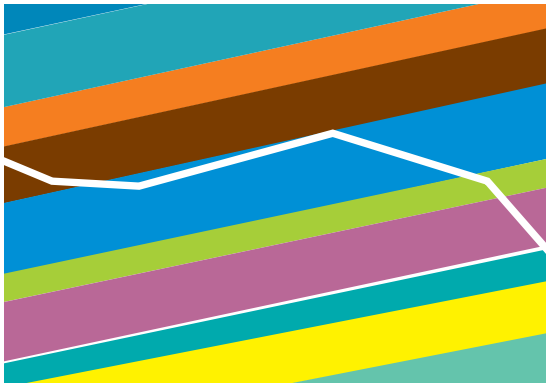

(a) Positive dipping of the layers

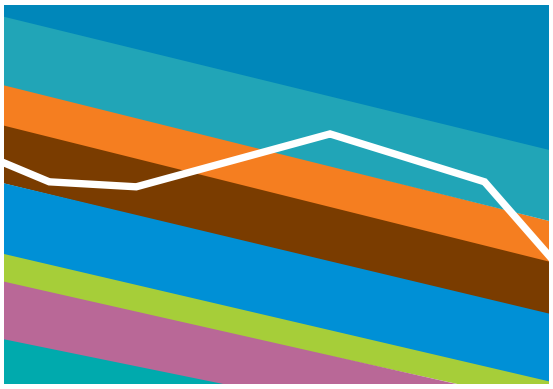

(b) Negative dipping of the layers

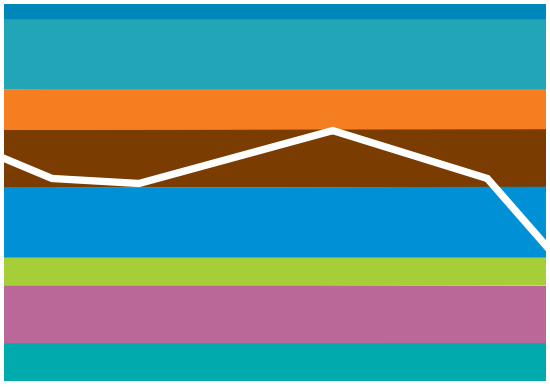

(c) Zero dipping of the layers

Figure 1.4.: Different scenarios of a 1D media for a specific trajectory.

In the presence of a 3D point source, a 1D formation model allows to reduce

the dimensionality of the problem from 3D to the so-called one and a half dimensional (1.5D) problem via a Hankel or a 2D Fourier transform along the directions over which we assume the material properties to be invariant (see e.g., [75, 22, 53]). This 1.5D approximation can also be used to obtain an initial subsurface resistivity distribution for marine CSEM measurements [78]. By performing this dimensionality reduction, we obtain a system of Ordinary Differential Equations (ODEs) that can be solved either: (a) analytically, by considering a piecewise constant resistivity profile, which leads to a so-called semi-analytic approach after the numerical inversion of a Hankel transform [53, 48, 41, 70, 60], or (b) numerically, leading to a numerical approach [23, 75] (see Figure 1.5).

Despite the high efficiency of semi-analytic methods, solving the ODEs analytically has some significant limitations, for example, (a) they may sometimes lead to an unrealistic mapping of the reservoir since they have to consider piecewise constant resistivity profiles, and as a result, they often employ a sharp Oil-Water Contact (OWC). However, in many realistic reservoir models, the OWC often appears as an Oil-Water Transition (OWT) zone with a variable resistivity profile because of capillary pressure and the existence of immiscible fluids (oil and water) (see Figure 5.3) [49, 29, 55, 12]. To model this with a 1.5D semi-analytical code, it is necessary to approximate the real model in the OWT zone using multiple constant-resistivity layers, which increases the computational cost, implementation, modeling error, and complexity of computing derivatives needed by gradient-based inversion methods; (b) a specific set of cumbersome formulas has to be derived for each physical process (e.g., electromagnetism, elasticity, etc.) anisotropy type, etc.; (c) analytical derivatives of specific models (e.g., cross-bedded formations, or derivatives with respect to bed boundary positions) are often difficult to obtain and have not been published to the best of our knowledge [80, 67, 61] which one needs them for a gradient-based inversion techniques (e.g., Gauss-Newton).

Solving the resulting ODEs numerically is also possible. The corresponding method also exhibits a linear cost with respect to the discretization size, since it consists of a sequence of independent 1D problems. An example of this approach can be found in [23], where Davydycheva et al. use a 2D Fourier transform to reduce the dimension of the problem. Then, they employ a highly accurate 1D Finite Difference Method (FDM) to solve the resulting ODEs. This method is relatively simple to implement. However, it requires a computational cost that is over 1000 times larger than that observed in semi-analytic methods. This occurs due to the high number of unknowns required to discretize the ODEs properly. If a common factorization of the system matrix based on a lower and an upper triangular matrix (the so-called LU factoriza-

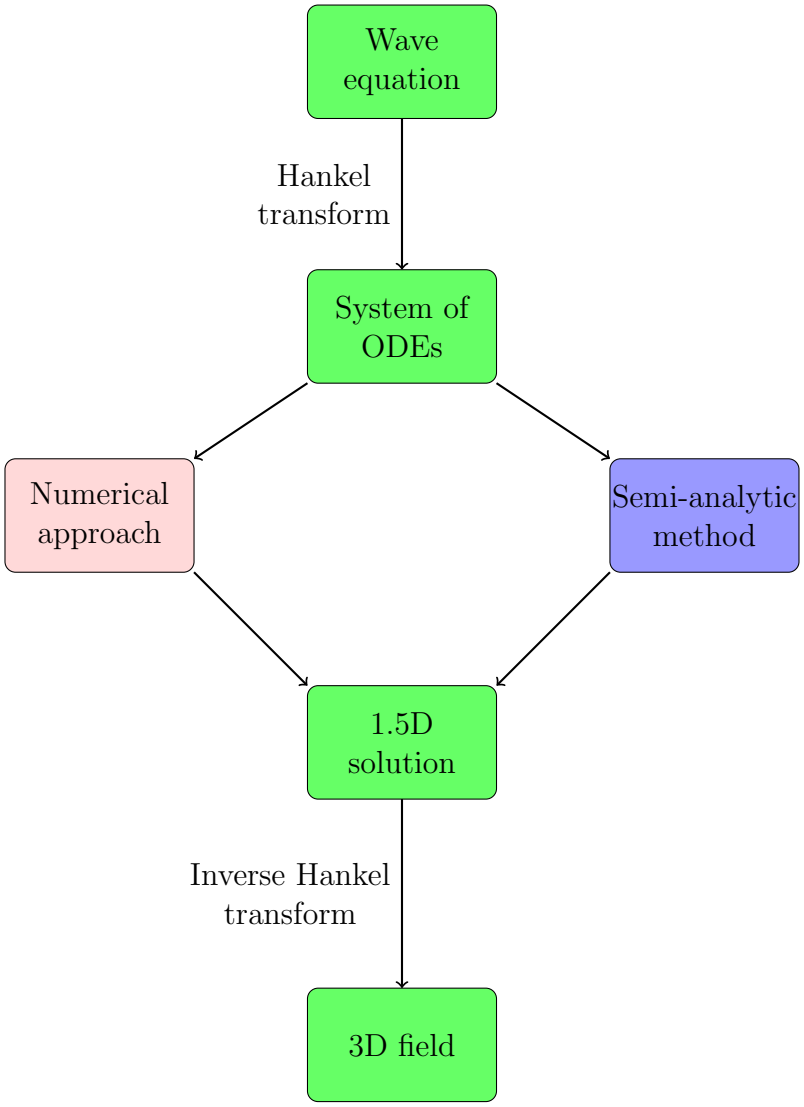

Figure 1.5.: 1.5D Dimensionality Reduction.

tion) would be precomputed for all source positions, the situation would only worsen: one would need a refined grid to model all sources accurately, and since the cost of backward substitution is also proportional to the discretization size (as it occurs with the LU factorization), the large computational cost required to perform backward substitution would significantly increase the total cost of the solver. The use of other traditional techniques such as a Finite Element Method (FEM) (see, e.g., [25]) to solve the resulting ODEs would not alleviate those problems. Additionally, in [23], the use of a 2D Fourier transform presents another burden on the performance of the solver, since the number of

ODEs (and the total solver cost) increases quadratically with respect to the number of integration points of the 1D Inverse Fourier Transform (IFT), while in the case of a Hankel Transform, the cost only grows linearly with respect to the number of integration points on the 1D Inverse Hankel Transform (IHT).

1.2. Main contribution

1.2.1. On the field of forward problems

One of the objectives of this work is to overcome the limitations of both semi-analytic and existing numerical methods by solving each 1D problem (associated with a Hankel mode) using an efficient multiscale FEM. Additionally, we seek a method that exhibits the following features: (a) it can consider arbitrary resistivity distributions along the 1D direction (as it occurs on an OWT zone), and not just a piecewise constant distribution as in the case of semi-analytic methods, and (b) it can easily and rapidly construct derivatives with respect to resistivity values and position of the bed boundaries by using an adjoint formulation, which allows us to compute numerically the derivatives forming the Jacobian matrix needed by the Gauss-Newton inversion method at (almost) no additional cost. Moreover, using a multiscale method, we reach the high efficiency required for the application while avoiding unnecessary approximations of the resistivity model in the OWT zone. Despite these advances, presently our proposed multiscale method is slower than the semi-analytic one. However, it is approximately two orders of magnitude faster than a traditional 1D FEM or a 1D FDM, like the one presented in [23]. This speedup is essential for practical applications since one often needs to simulate thousands of logging positions and estimate millions of derivatives to solve real-time inversion problems in the field for geosteering operations. Additionally, we employ a 1D Hankel transform rather than a 2D Fourier transform. This leads to a more complex mathematical formulation, but the resulting method exhibits a superior performance due to the lower number of ODEs that need to be solved.

1.2.2. On the field of inverse problems

In here, we propose a different approach to the conventional ones based on approximating function $\mathbf{I}$ *offline* (i.e., *a priori*) using a Deep Neural Network (DNN), and then, during field (*online*) operations, evaluate this approximation for each given set of recorded measurements $\boldsymbol{\mathcal{M}}$.

The first DNN was published in 1965 [39]. The term *Deep Learning* was introduced in 1986 [24], and later in 2000 [3] to refer to a Neural Network (NN)

that contains a large number of layers [54]. A DNN enables to automatically detect and extract complex features that may be present in a given dataset. This was not possible with traditional NNs. In the last decade, DNNs have proven to be useful in multiple areas of knowledge (including computer vision [54], speech recognition [86], and biometrics [11]) to approximate complex functions with unknown properties. In recent years, the use of machine learning algorithms [15, 6, 46, 32, 7, 14] and deep learning [81, 33] in computational mechanics and computational geophysics have become an active area of study. However, to the best of our knowledge, Deep Learning algorithms have not been applied to the inversion of borehole resistivity measurements, and therefore, its advantages and limitations remain unexplored.

In this work, we provide an introduction for geophysicists on the use of DNNs for solving inverse problems and analyze their main features and limitations when applied to the rapid interpretation of borehole resistivity measurements for geosteering purposes. To simplify the problem and increase the speed of computations, we restrict to the Earth formations composed by a sequence of 1D layers.

1.3. Outline

The remaining parts of this dissertation are organized as follows: Chapter 2 presents Maxwell's equation and the corresponding reduced wave equations, formulates a suitable 1.5D variational formulation, and provides a detailed description of the multiscale FEM. Chapter 3 computes the derivatives of the magnetic field with respect to bed boundary positions and resistivity value of each layer using an adjoint state method for the 3D and 1.5D variational formulations. Chapter 4 verifies our formulations and methods using synthetic examples. Chapter 5 demonstrates the application of our proposed numerical method for simulation of an OWT zone. We also investigate the capability of using deep learning for the inversion of resistivity measurements. Chapter 6 is devoted to the conclusions and future works. Chapter 7 provides a list of achievements of this dissertation. This work also contains two appendices. Appendix A describes the Bessel functions and illustrates their main properties employed in this work. Appendix B explains the DNN that we used for the inversion of borehole resistivity measurements.

2. 1.5D Multiscale Finite Element Method

In this chapter, we introduce Maxwell's equations, which are the governing equations for electromagnetics,, and we compute the reduced wave equation and its variational formulation. Then, we derive a 1.5D variational formulation. Finally, we propose a Multiscale Hankel Finite Element Method (Ms-HFEM) for efficiently solving the 1.5D problem, and we describe the proposed method in detail.

2.1. Maxwell's equations

2.1.1. Strong formulation

Let $\boldsymbol{\sigma}(x, y, z)$ be a real-valued conductivity tensor with positive determinant. Let $\mathbf{J}$ be a volumetric current source density and $\mathbf{M}$ a magnetic volumetric current source. Then, the EM fields satisfy Maxwell's equations in 3D space [62]:

$$\nabla \times \boldsymbol{\mathcal{H}} = (\boldsymbol{\sigma} - i\omega\boldsymbol{\varepsilon})\,\boldsymbol{\mathcal{E}} + \mathbf{J}, \tag{2.1}$$

$$\nabla \times \boldsymbol{\mathcal{E}} = i\omega\boldsymbol{\mu}\boldsymbol{\mathcal{H}} + i\omega\boldsymbol{\mu}\mathbf{M}, \tag{2.2}$$

where $\boldsymbol{\mathcal{E}}$ and $\boldsymbol{\mathcal{H}}$ are the time-harmonic (sinusoidal) complex-valued electric and magnetic fields, respectively, $\omega = 2\pi f$ is the angular frequency, where $f > 0$ is the frequency of the transmitter, $\boldsymbol{\varepsilon}$ and $\boldsymbol{\mu}$ are the permittivity and magnetic permeability tensors of the media, respectively, and i is the imaginary unit, $i^2 = -1$. The problem domain is $\Omega = \mathbb{R}^3$. By pre-multiplying (2.1) by $\tilde{\boldsymbol{\sigma}}^{-1} = (\boldsymbol{\sigma} - i\omega\boldsymbol{\varepsilon})^{-1}$, applying the curl operator, and substituting (2.2) into the result, we arrive at the following reduced wave equation for the magnetic field:

$$\nabla \times \tilde{\boldsymbol{\sigma}}^{-1}\nabla \times \boldsymbol{\mathcal{H}} - i\omega\boldsymbol{\mu}\boldsymbol{\mathcal{H}} = \mathbf{R}, \tag{2.3}$$

where the right-hand side is:

$$\mathbf{R} = i\omega\boldsymbol{\mu}\mathbf{M} + \nabla \times \tilde{\boldsymbol{\sigma}}^{-1}\mathbf{J}.$$

In order to ensure the uniqueness of the magnetic field, we use the Silver-Müller radiation condition [44, 42, 25, 82].

2.1.2. Variational formulation

Let $\boldsymbol{\mathcal{F}}$ be an arbitrary test function and $\boldsymbol{\mathcal{F}}^*$ its conjugate transpose. Premultiplying Equation (2.3) by $\boldsymbol{\mathcal{F}}^*$ and integrating over the domain Ω, we obtain the following equation:

$$\int_\Omega \boldsymbol{\mathcal{F}}^*(\nabla \times \tilde{\boldsymbol{\sigma}}^{-1}\nabla \times \boldsymbol{\mathcal{H}})d\Omega - i\omega \int_\Omega \boldsymbol{\mathcal{F}}^*\boldsymbol{\mu}\boldsymbol{\mathcal{H}}d\Omega = \int_\Omega \boldsymbol{\mathcal{F}}^*\mathbf{R}d\Omega. \tag{2.4}$$

In the above, as a sufficient condition to ensure integrability, we select $\boldsymbol{\mathcal{F}} \in H(\mathbf{curl};\Omega)$, where:

$$H(\mathbf{curl};\Omega) = \{\boldsymbol{\mathcal{F}} \in (L^2(\Omega))^3 : \nabla \times \boldsymbol{\mathcal{F}} \in (L^2(\Omega))^3\}.$$

Using integration by parts assuming that the solution and its flux are continuous, and considering the radiation condition, we obtain the following variational formulation:

$$\int_\Omega (\nabla \times \boldsymbol{\mathcal{F}})^*(\tilde{\boldsymbol{\sigma}}^{-1}\nabla \times \boldsymbol{\mathcal{H}})d\Omega - i\omega \int_\Omega \boldsymbol{\mathcal{F}}^*\boldsymbol{\mu}\boldsymbol{\mathcal{H}}d\Omega = \int_\Omega \boldsymbol{\mathcal{F}}^*\mathbf{R}d\Omega. \tag{2.5}$$

2.2. 1.5D variational formulation

In this work, we consider 3D Maxwell's equations in a 1D Transversaly Isotropic (TI) layered formation. That is, the formation conductivity is constant along the x and y directions, and the conductivity tensor is defined as:

$$\boldsymbol{\sigma}(z) = \begin{pmatrix} \sigma_h(z) & 0 & 0 \\ 0 & \sigma_h(z) & 0 \\ 0 & 0 & \sigma_v(z) \end{pmatrix}, \tag{2.6}$$

where $\sigma_h > 0$ is the conductivity of the media along the x and y directions, and $\sigma_v > 0$ is the conductivity along z direction. Our formulation allows for variations in the parameters along the z-axis. Analogously, $\boldsymbol{\varepsilon}(z)$ and $\boldsymbol{\mu}(z)$ are assumed to be 1D TI tensors.

Since material properties are uniform in the xy-plane, it is convenient to use a Hankel transform to represent the magnetic field along x and y directions.

2.2.1. Hankel transform

We consider $\widehat{\boldsymbol{H}}$ to be the 2D Fourier transform of $\boldsymbol{\mathcal{H}}$ along x and y directions, where the material properties are homogeneous. We have:

$$\boldsymbol{\mathcal{H}}(\boldsymbol{x}, z) = \frac{1}{4\pi^2}\int_{-\infty}^{+\infty}\int_{-\infty}^{+\infty} \widehat{\boldsymbol{H}}(\mathbf{k}, z)e^{i\mathbf{k}\cdot\mathbf{x}}d\mathbf{k}, \tag{2.7}$$

where $\mathbf{x} = (x, y)$ and $\mathbf{k} = (k_x, k_y)$ (see Figure 2.1). We switch from the Cartesian system of coordinates to a cylindrical one according to the following transformations:

$$\begin{aligned} x &= \rho \cdot \cos\phi, \;\; y = \rho \cdot \sin\phi, \\ k_x &= \xi \cdot \cos\theta, \;\; k_y = \xi \cdot \sin\theta. \end{aligned} \tag{2.8}$$

Substituting (2.8) into (2.7), we obtain:

$$\boldsymbol{\mathcal{H}}(\boldsymbol{\rho}) = \frac{1}{4\pi^2} \int_0^{+\infty} \int_0^{2\pi} \widehat{\boldsymbol{H}}(\xi, \theta, z) e^{i\xi\rho(\cos\theta\cos\phi + \sin\theta\sin\phi)} d\theta \xi d\xi, \tag{2.9}$$

where $\boldsymbol{\rho} = (\rho, \phi, z)$. Using the trigonometric identity:

$$\cos(\phi - \theta) = \cos\theta\cos\phi + \sin\theta\sin\phi, \tag{2.10}$$

we obtain:

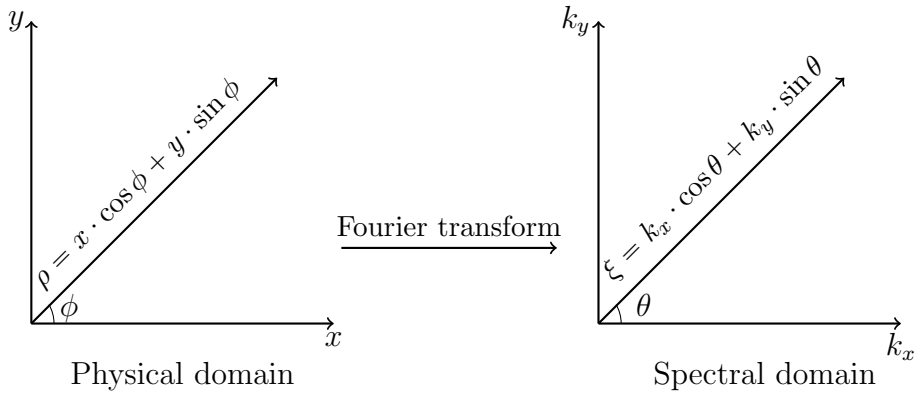

Figure 2.1.: Cartesian and cylindrical systems of coordinates.

$$\boldsymbol{\mathcal{H}}(\boldsymbol{\rho}) = \frac{1}{4\pi^2} \int_0^{+\infty} \int_0^{2\pi} \widehat{\boldsymbol{H}}(\xi, \theta, z) e^{i\xi\rho\cos(\phi-\theta)} d\theta \xi d\xi. \tag{2.11}$$

We now use the following relation between exponentials and Bessel functions:

$$e^{i\xi\rho\cos(\phi-\theta)} = \sum_{m=-\infty}^{\infty} i^m J_m(\xi\rho) e^{-im(\phi-\theta)} \tag{2.12}$$

to obtain

$$\boldsymbol{\mathcal{H}}(\boldsymbol{\rho}) = \frac{1}{2\pi} \sum_{m=-\infty}^{\infty} \int_0^{+\infty} \boldsymbol{H}^m(\xi, z) J_m(\xi\rho) e^{-im\phi} \xi d\xi, \tag{2.13}$$

where

$$\boldsymbol{H}^m(\xi, z) = \frac{1}{2\pi} \int_0^{2\pi} \widehat{\boldsymbol{H}}(\xi, \theta, z) i^m e^{im\theta} d\theta. \tag{2.14}$$

We compute the cylindrical components of the magnetic field as follows:

$$\begin{aligned} H_\rho^m &= \cos\phi \cdot H_x^m + \sin\phi \cdot H_y^m \\ &= e^{i\phi}(\frac{H_x^m - iH_y^m}{2}) + e^{-i\phi}(\frac{H_x^m + iH_y^m}{2}) \\ &= e^{i\phi} H_+^m + e^{-i\phi} H_-^m, \end{aligned} \tag{2.15}$$

where

$$\begin{aligned} H_+^m &= \frac{H_x^m - iH_y^m}{2}, \\ H_-^m &= \frac{H_x^m + iH_y^m}{2}. \end{aligned} \tag{2.16}$$

Similarly, for $\mathcal{H}_\phi$, we have:

$$H_\phi^m = -\sin\phi \cdot H_x^m + \cos\phi \cdot H_y^m = i\left(e^{i\phi} H_+^m - e^{-i\phi} H_-^m\right). \tag{2.17}$$

By substituting (2.15) and (2.17) into (2.13), the Hankel representation of the magnetic field becomes:

$$\begin{aligned} \mathcal{H}_\rho(\boldsymbol{\rho}) &= \frac{1}{2\pi} \sum_{m=-\infty}^{+\infty} e^{-im\phi} \int_0^{+\infty} \Big(H_+^m(\xi, z) J_{m+1}(\xi\rho) + H_-^m(\xi, z) J_{m-1}(\xi\rho) \Big) \xi d\xi, \\ \mathcal{H}_\phi(\boldsymbol{\rho}) &= \frac{i}{2\pi} \sum_{m=-\infty}^{+\infty} e^{-im\phi} \int_0^{+\infty} \Big(H_+^m(\xi, z) J_{m+1}(\xi\rho) - H_-^m(\xi, z) J_{m-1}(\xi\rho) \Big) \xi d\xi, \\ \mathcal{H}_z(\boldsymbol{\rho}) &= \frac{1}{2\pi} \sum_{m=-\infty}^{+\infty} e^{-im\phi} \int_0^{+\infty} H_z^m(\xi, z) J_m(\xi\rho) \xi d\xi. \end{aligned} \tag{2.18}$$

The curl of the magnetic field in cylindrical coordinates is:

$$\begin{aligned} \nabla \times \boldsymbol{\mathcal{H}} = &\left(\frac{1}{\rho} \frac{\partial \mathcal{H}_z}{\partial \phi} - \frac{\partial \mathcal{H}_\phi}{\partial z} \right) \hat{\boldsymbol{\rho}} + \left(\frac{\partial \mathcal{H}_\rho}{\partial z} - \frac{\partial \mathcal{H}_z}{\partial \rho} \right) \hat{\boldsymbol{\phi}} \\ &+ \frac{1}{\rho} \left(\mathcal{H}_\phi + \rho \frac{\partial \mathcal{H}_\phi}{\partial \rho} - \frac{\partial \mathcal{H}_\rho}{\partial \phi} \right) \hat{\boldsymbol{z}}. \end{aligned} \tag{2.19}$$

By substituting (2.18) into (2.19), the first component of the curl becomes:

$$\begin{aligned} (\nabla \times \boldsymbol{\mathcal{H}})_\rho = \frac{-i}{2\pi} \sum_{m=-\infty}^{+\infty} e^{-im\phi} \int_\xi \Bigg(&\frac{m}{\rho} H_z^m(\xi, z) J_m(\xi\rho) \\ &+ \frac{\partial H_+^m(\xi, z)}{\partial z} J_{m+1}(\xi\rho) - \frac{\partial H_-^m(\xi, z)}{\partial z} J_{m-1}(\xi\rho) \Bigg) \xi d\xi. \end{aligned} \tag{2.20}$$

By using the property of Bessel functions given by Equation (A.6) of Appendix A, we obtain:

$$(\nabla \times \boldsymbol{\mathcal{H}})_\rho = \frac{-i}{2\pi} \sum_{m=-\infty}^{+\infty} e^{-im\phi} \int_\xi \left[H_z^m(\xi,z) \left(\xi J_{m-1}(\xi\rho) - \xi \frac{\partial J_m(\xi\rho)}{\partial(\xi\rho)} \right) + \frac{\partial H_+^m(\xi,z)}{\partial z} J_{m+1}(\xi\rho) - \frac{\partial H_-^m(\xi,z)}{\partial z} J_{m-1}(\xi\rho) \right] \xi d\xi. \tag{2.21}$$

Using the formula of the derivative of the Bessel function given by Equation (A.4) of Appendix A, we have:

$$(\nabla \times \boldsymbol{\mathcal{H}})_\rho = \frac{-i}{2\pi} \sum_{m=-\infty}^{+\infty} e^{-im\phi} \int_\xi \left[H_z^m(\xi,z) \left(\xi J_{m-1}(\xi\rho) - \frac{\xi}{2} J_{m-1}(\xi\rho) + \frac{\xi}{2} J_{m+1}(\xi\rho) \right) + \frac{\partial H_+^m(\xi,z)}{\partial z} J_{m+1}(\xi\rho) - \frac{\partial H_-^m(\xi,z)}{\partial z} J_{m-1}(\xi\rho) \right] \xi d\xi. \tag{2.22}$$

For an arbitrary function $\mathbf{g}(\xi,z) = (g_-(\xi,z), g_+(\xi,z), g_z(\xi,z))$ in the spectral domain, we introduce the following notation to simplify computations:

$$\begin{aligned} \Pi_+^\xi(\mathbf{g}(\xi,z)) &= \frac{\partial g_+(\xi,z)}{\partial z} + \frac{\xi}{2} g_z(\xi,z), \\ \Pi_-^\xi(\mathbf{g}(\xi,z)) &= \frac{\partial g_-(\xi,z)}{\partial z} - \frac{\xi}{2} g_z(\xi,z), \\ \Pi_z^\xi(\mathbf{g}(\xi,z)) &= \xi\left(g_-(\xi,z) + g_+(\xi,z)\right). \end{aligned} \tag{2.23}$$

Using (2.23), we obtain:

$$(\nabla \times \boldsymbol{\mathcal{H}})_\rho = -\frac{i}{2\pi} \sum_{m=-\infty}^{+\infty} e^{-im\phi} \int_\xi \left(\Pi_+^\xi(\mathbf{H}^m(\xi,z)) J_{m+1}(\xi\rho) - \Pi_-^\xi(\mathbf{H}^m(\xi,z)) J_{m-1}(\xi\rho) \right) \xi d\xi. \tag{2.24}$$

For the second component of (2.19), using (2.18), we have:

$$(\nabla \times \boldsymbol{\mathcal{H}})_\phi = \frac{1}{2\pi} \sum_{m=-\infty}^{+\infty} e^{-im\phi} \int_\xi \left[\left(\frac{\partial H_+^m(\xi,z)}{\partial z} J_{m+1}(\xi\rho) + \frac{\partial H_-^m(\xi,z)}{\partial z} J_{m-1}(\xi\rho) \right) - H_z^m(\xi,z) \frac{\partial J_{m+1}(\xi\rho)}{\partial(\xi\rho)} \xi \right] \xi d\xi. \tag{2.25}$$

Using the property of the Bessel functions given by Equation (A.4) of Appendix A and (2.23), we obtain:

$$(\nabla \times \boldsymbol{\mathcal{H}})_{\phi} = \frac{1}{2\pi} \sum_{m=-\infty}^{+\infty} e^{-im\phi} \int_{\xi} \Big(\Pi_{+}^{\xi} \left(\mathbf{H}^{m}(\xi, z) \right) J_{m+1}(\xi\rho) + \Pi_{-}^{\xi} \left(\mathbf{H}^{m}(\xi, z) \right) J_{m-1}(\xi\rho) \Big) \xi d\xi. \tag{2.26}$$

The third component of (2.19) becomes after using (2.18):

$$\begin{aligned} (\nabla \times \boldsymbol{\mathcal{H}})_{z} = & \frac{i}{2\pi} \sum_{m=-\infty}^{+\infty} e^{-im\phi} \\ & \cdot \int_{\xi} \left[\left(\frac{J_{m+1}(\xi\rho)}{\rho} + \xi \frac{\partial J_{m+1}(\xi\rho)}{\partial (\xi\rho)} + \frac{m}{\rho} J_{m+1}(\xi\rho) \right) H_{+}^{m}(\xi, z) \right. \\ & \left. - \left(\frac{J_{m-1}(\xi\rho)}{\rho} + \xi \frac{\partial J_{m-1}(\xi\rho)}{\partial (\xi\rho)} - \frac{m}{\rho} J_{m-1}(\xi\rho) \right) H_{-}^{m}(\xi, z) \right] \xi d\xi. \end{aligned} \tag{2.27}$$

For the derivative of J_{m+1}, we use Equation (A.6) of Appendix A, and for the derivative of J_{m-1}, we use Equation (A.4) of the same appendix. Then,

$$\begin{aligned} (\nabla \times \boldsymbol{\mathcal{H}})_{z} = & \frac{i}{2\pi} \sum_{m=-\infty}^{+\infty} e^{-im\phi} \\ & \cdot \int_{\xi} \left[\left(\frac{J_{m+1}(\xi\rho)}{\rho} + \xi J_{m}(\xi\rho) - \frac{m+1}{\rho} J_{m+1}(\xi\rho) + \frac{m}{\rho} J_{m+1}(\xi\rho) \right) H_{+}^{m}(\xi, z) \right. \\ & \left. - \left(\frac{J_{m-1}(\xi\rho)}{\rho} + \frac{\xi}{2} J_{m-2}(\xi\rho) - \frac{\xi}{2} J_{m}(\xi\rho) - \frac{m}{\rho} J_{m-1}(\xi\rho) \right) H_{-}^{m}(\xi, z) \right] \xi d\xi. \end{aligned} \tag{2.28}$$

We use Equation (A.1) of Appendix A to simplify J_{m-2}. As a result, we obtain:

$$(\nabla \times \boldsymbol{\mathcal{H}})_{z} = \frac{i}{2\pi} \sum_{m=-\infty}^{+\infty} e^{-im\phi} \int_{\xi} \Pi_{z}^{\xi} \left(\mathbf{H}^{m}(\xi, z) \right) J_{m}(\xi\rho) \xi d\xi. \tag{2.29}$$

2.2.2. Hankel Finite Element (HFE) full field formulation

L^2-orthogonality holds for Bessel functions of the same order (see Equation (A.3) of Appendix A). Hence, in order to simplify the terms of the variational formulation containing Bessel functions, we introduce the following matrix:

$$Q = \frac{1}{\sqrt{2}} \begin{pmatrix} 1 & i & 0 \\ i & 1 & 0 \\ 0 & 0 & \sqrt{2} \end{pmatrix}. \tag{2.30}$$

Q is a unitary matrix, since:

$$QQ^* = Q^*Q = I.$$

Hence, the change of coordinates implied by Q preserves the inner product. In particular, for arbitrary vector-valued functions $\mathbf{U}$ and $\mathbf{V}$, we have:

$$\mathbf{V}^*\mathbf{U} = (Q\mathbf{V})^*(Q\mathbf{U}).$$

By using the above matrix, we obtain the following equalities:

$$\begin{aligned}
\Big(Q\widetilde{\boldsymbol{\sigma}}^{-1}(z)\nabla\times\boldsymbol{\mathcal{H}}\Big)_\rho &= \frac{i}{\sqrt{2}\pi}\sum_{m=-\infty}^{+\infty} e^{-im\phi}\int_0^{+\infty}\widetilde{\sigma}_h^{-1}(z)\cdot\Pi_-^\xi\left(\mathbf{H}^m(\xi,z)\right)J_{m-1}(\xi\rho)\xi d\xi,\\
\Big(Q\widetilde{\boldsymbol{\sigma}}^{-1}(z)\nabla\times\boldsymbol{\mathcal{H}}\Big)_\phi &= \frac{1}{\sqrt{2}\pi}\sum_{m=-\infty}^{+\infty} e^{-im\phi}\int_0^{+\infty}\widetilde{\sigma}_h^{-1}(z)\cdot\Pi_+^\xi\left(\mathbf{H}^m(\xi,z)\right)J_{m+1}(\xi\rho)\xi d\xi,\\
\Big(Q\widetilde{\boldsymbol{\sigma}}^{-1}(z)\nabla\times\boldsymbol{\mathcal{H}}\Big)_z &= \frac{i}{2\pi}\sum_{m=-\infty}^{+\infty} e^{-im\phi}\int_0^{+\infty}\widetilde{\sigma}_v^{-1}(z)\cdot\Pi_z^\xi\left(\mathbf{H}^m(\xi,z)\right)J_m(\xi\rho)\xi d\xi,
\end{aligned} \tag{2.31}$$

where $\widetilde{\sigma}_h = \sigma_h - i\omega\varepsilon_h$ and $\widetilde{\sigma}_v = \sigma_v - i\omega\varepsilon_v$. For the L^2 terms, we obtain:

$$\begin{aligned}
(Q\boldsymbol{\mathcal{H}})_\rho &= \frac{1}{\sqrt{2}\pi}\sum_{m=-\infty}^{+\infty} e^{-im\phi}\int_0^{+\infty} H_-^m(\xi,z)J_{m-1}(\xi\rho)\xi d\xi,\\
(Q\boldsymbol{\mathcal{H}})_\phi &= \frac{i}{\sqrt{2}\pi}\sum_{m=-\infty}^{+\infty} e^{-im\phi}\int_0^{+\infty} H_+^m(\xi,z)J_{m+1}(\xi\rho)\xi d\xi,\\
(Q\boldsymbol{\mathcal{H}})_z &= \frac{1}{2\pi}\sum_{m=-\infty}^{+\infty} e^{-im\phi}\int_0^{+\infty} H_z^m(\xi,z)J_m(\xi\rho)\xi d\xi.
\end{aligned} \tag{2.32}$$

For a specific Hankel mode $\xi_q > 0$ and an exponential order t, we select a mono-modal test function of the form:

$$\boldsymbol{\mathcal{F}}^{q,t}(\boldsymbol{\rho}) = \mathcal{F}_\rho^{q,t}(\boldsymbol{\rho})\hat{\boldsymbol{\rho}} + \mathcal{F}_\phi^{q,t}(\boldsymbol{\rho})\hat{\boldsymbol{\phi}} + \mathcal{F}_z^{q,t}(\boldsymbol{\rho})\hat{\mathbf{z}}, \tag{2.33}$$

where:

$$\begin{aligned}
\mathcal{F}_\rho^{q,t}(\boldsymbol{\rho}) &= e^{-it\phi}\Big(F_+^t(\xi_q,z)J_{t+1}(\xi_q\rho) + F_-^t(\xi_q,z)J_{t-1}(\xi_q\rho)\Big),\\
\mathcal{F}_\phi^{q,t}(\boldsymbol{\rho}) &= ie^{-it\phi}\Big(F_+^t(\xi_q,z)J_{t+1}(\xi_q\rho) - F_-^t(\xi_q,z)J_{t-1}(\xi_q\rho)\Big),\\
\mathcal{F}_z^{q,t}(\boldsymbol{\rho}) &= e^{-it\phi}F_z^t(\xi_q,z)J_t(\xi_q\rho).
\end{aligned} \tag{2.34}$$

Using (2.31) and the test functions defined in (2.34), we have:

$$\int_{z,\phi,\rho} \left(Q\nabla \times \boldsymbol{\mathcal{F}}^{q,t}\right)_{\rho}^{*} \left(Q\widetilde{\boldsymbol{\sigma}}^{-1}(z)\nabla \times \boldsymbol{\mathcal{H}}\right)_{\rho} \rho d\rho d\phi dz = \frac{1}{\pi}\int_{z}\left(\sum_{m=-\infty}^{+\infty}\int_{\xi,\phi,\rho} e^{i(t-m)\phi} \cdot \left(\Pi_{-}^{\xi_q}\left(\mathbf{F}^{t}\right)\right)^{*} \widetilde{\sigma}_{h}^{-1}(z)\Pi_{-}^{\xi}(\mathbf{H}^{m}) \cdot J_{t-1}(\xi_q\rho)J_{m-1}(\xi\rho)\rho d\rho d\phi\xi d\xi\right)dz, \tag{2.35}$$

where $\mathbf{F}^t = (F_+^t, F_-^t, F_z^t)$. Separating the integrals according to each variable and using the L^2-orthogonality property of exponential functions, we have:

$$\int_{z,\phi,\rho} \left(Q\nabla \times \boldsymbol{\mathcal{F}}^{q,t}\right)_{\rho}^{*} \left(Q\widetilde{\boldsymbol{\sigma}}^{-1}(z)\nabla \times \boldsymbol{\mathcal{H}}\right)_{\rho} \rho d\rho d\phi dz = 2\int_{z}\left[\int_{\xi}\left(\left(\Pi_{-}^{\xi_q}\left(\mathbf{F}^{t}\right)\right)^{*} \widetilde{\sigma}_{h}^{-1}(z)\Pi_{-}^{\xi}(\mathbf{H}^{t}) \cdot \int_{\rho} J_{t-1}(\xi_q\rho)J_{t-1}(\xi\rho)\rho d\rho\right)\xi d\xi\right]dz. \tag{2.36}$$

By the orthogonality property of the Bessel functions given by Equation (A.3) of Appendix A, we obtain:

$$\int_{z,\phi,\rho} \left(Q\nabla \times \boldsymbol{\mathcal{F}}^{q,t}\right)_{\rho}^{*} \left(Q\widetilde{\boldsymbol{\sigma}}^{-1}(z)\nabla \times \boldsymbol{\mathcal{H}}\right)_{\rho} \rho d\rho d\phi dz = 2\int_{z}\left(\Pi_{-}^{\xi_q}\left(\mathbf{F}^{t}\right)\right)^{*} \widetilde{\sigma}_{h}^{-1}(z)\Pi_{-}^{\xi_q}(\mathbf{H}^{t})dz. \tag{2.37}$$

Similarly, for the other components of the curl, we have:

$$\int_{z,\phi,\rho} \left(Q\nabla \times \boldsymbol{\mathcal{F}}^{q,t}\right)_{\phi}^{*} \left(Q\widetilde{\boldsymbol{\sigma}}^{-1}(z)\nabla \times \boldsymbol{\mathcal{H}}\right)_{\phi} \rho d\rho d\phi dz = 2\int_{z}\left(\Pi_{+}^{\xi_q}\left(\mathbf{F}^{t}\right)\right)^{*} \widetilde{\sigma}_{h}^{-1}(z)\Pi_{+}^{\xi_q}(\mathbf{H}^{t})dz, \tag{2.38}$$

$$\int_{z,\phi,\rho} \left(Q\nabla \times \boldsymbol{\mathcal{F}}^{q,t}\right)_{z}^{*} \left(Q\widetilde{\boldsymbol{\sigma}}^{-1}(z)\nabla \times \boldsymbol{\mathcal{H}}\right)_{z} \rho d\rho d\phi dz = \int_{z}\left(\Pi_{z}^{\xi_q}\left(\mathbf{F}^{t}\right)\right)^{*} \widetilde{\sigma}_{v}^{-1}(z)\Pi_{z}^{\xi_q}\left(\mathbf{H}^{t}\right)dz. \tag{2.39}$$

For the L^2 terms, using (2.32) and the test functions defined in (2.34), and using L^2-orthogonality property of exponentials and orthogonality property of

the Bessel functions given by (A.3) of Appendix A, we obtain:

$$\begin{aligned}
\int_{z,\phi,\rho}\Big(Q\boldsymbol{\mathcal{F}}^{q,t}\Big)_{\rho}^{*}\Big(Q\boldsymbol{\mu}\boldsymbol{\mathcal{H}}\Big)_{\rho}\rho d\rho d\phi dz &= 2\int_{z}\left(F_{-}^{t}(\xi_q,z)\right)^{*}\mu_h(z)H_{-}^{t}(\xi_q,z)dz,\\
\int_{z,\phi,\rho}\Big(Q\boldsymbol{\mathcal{F}}^{q,t}\Big)_{\phi}^{*}\Big(Q\boldsymbol{\mu}\boldsymbol{\mathcal{H}}\Big)_{\phi}\rho d\rho d\phi dz &= 2\int_{z}\left(F_{+}^{t}(\xi_q,z)\right)^{*}\mu_h(z)H_{+}^{t}(\xi_q,z)dz,\\
\int_{z,\phi,\rho}\Big(Q\boldsymbol{\mathcal{F}}^{q,t}\Big)_{z}^{*}\Big(Q\boldsymbol{\mu}\boldsymbol{\mathcal{H}}\Big)_{z}\rho d\rho d\phi dz &= \int_{z}\left(F_{z}^{t}(\xi_q,z)\right)^{*}\mu_v(z)H_{z}^{t}(\xi_q,z)dz.
\end{aligned} \tag{2.40}$$

Using (2.37), (2.38), (2.39) and (2.40), for each Hankel mode $\xi_q > 0$ and exponential order t, the stiffness matrix becomes:

$$b(\boldsymbol{\mathcal{F}}^{q,t},\boldsymbol{\mathcal{H}}) = b(\mathbf{F}^t,\mathbf{H}^t) = b_1(\mathbf{F}^t,\mathbf{H}^t) - b_2(\mathbf{F}^t,\mathbf{H}^t), \tag{2.41}$$

where

$$\begin{aligned}
b_1(\mathbf{F}^t,\mathbf{H}^t) =& 2\langle\Pi_{-}^{\xi_q}\left(\mathbf{F}^t\right),\widetilde{\sigma}_h^{-1}\Pi_{-}^{\xi_q}\left(\mathbf{H}^t\right)\rangle_{L^2} + 2\langle\Pi_{+}^{\xi_q}\left(\mathbf{F}^t\right),\widetilde{\sigma}_h^{-1}\Pi_{+}^{\xi_q}\left(\mathbf{H}^t\right)\rangle_{L^2}\\
&+\langle\Pi_{z}^{\xi_q}\left(\mathbf{F}^t\right),\widetilde{\sigma}_v^{-1}\Pi_{z}^{\xi_q}\left(\mathbf{H}^t\right)\rangle_{L^2},\\
b_2(\mathbf{F}^t,\mathbf{H}^t) =& i\omega\left(2\langle F_{-}^{t},\mu_h H_{-}^{t}\rangle_{L^2} + 2\langle F_{+}^{t},\mu_h H_{+}^{t}\rangle_{L^2} + \langle F_{z}^{t},\mu_v H_{z}^{t}\rangle_{L^2}\right).
\end{aligned} \tag{2.42}$$

Symbol $< .,. >_{L^2}$ represents the L^2 inner product given by:

$$\langle f,g\rangle_{L^2} = \int_{z} f^{*}g dz.$$

A sufficient condition to guarantee that the above integrals are finite is to require $\mathbf{H}^t,\mathbf{F}^t \in V(\mathbb{R})$, where $V(\mathbb{R}) = H^1(\mathbb{R})\times H^1(\mathbb{R})\times L^2(\mathbb{R})$, and

$$H^1(\mathbb{R}) = \{v\in L^2(\mathbb{R}) : \frac{\partial v}{\partial z}\in L^2(\mathbb{R})\}. \tag{2.43}$$

In (2.43), the weak derivative of the function is considered.

2.2.2.1. Load vector

In a 1D layered medium, we consider $(0,0,z_{Tx})$ to be the general representation of a point source location. We use the following identities to describe the right-hand side vector in cylindrical coordinates:

$$\begin{aligned}
\hat{\mathbf{x}} &= \cos(\phi)\hat{\boldsymbol{\rho}} - \sin(\phi)\hat{\boldsymbol{\phi}} = \frac{e^{-i\phi}}{2}(\hat{\boldsymbol{\rho}} - i\hat{\boldsymbol{\phi}}) + \frac{e^{i\phi}}{2}(\hat{\boldsymbol{\rho}} + i\hat{\boldsymbol{\phi}}),\\
\hat{\mathbf{y}} &= \sin(\phi)\hat{\boldsymbol{\rho}} + \cos(\phi)\hat{\boldsymbol{\phi}} = \frac{e^{-i\phi}}{2}(i\hat{\boldsymbol{\rho}} + \hat{\boldsymbol{\phi}}) - \frac{e^{i\phi}}{2}(i\hat{\boldsymbol{\rho}} - \hat{\boldsymbol{\phi}}),\\
\hat{\mathbf{z}} &= \hat{\mathbf{z}},
\end{aligned} \tag{2.44}$$

where $\hat{\mathbf{x}}$, $\hat{\mathbf{y}}$ and $\hat{\mathbf{z}}$ are the unitary vectors in Cartesian coordinates. The right-hand side of (2.3) in cylindrical coordinates for a z-oriented point source is:

$$\mathbf{R}_z = i\omega\mu_v(z)\frac{1}{2\pi\rho}\delta(\rho,0)\delta(z,z_{Tx})\hat{\boldsymbol{z}},$$

where δ is the Dirac delta distribution. We consider l to be the right-hand side of (2.5). Using $\boldsymbol{\mathcal{F}}^{q,t}$ as our test function and separating the integrals according to each variable, we obtain:

$$\begin{aligned} l(\mathbf{F}^t) =& \frac{i\omega}{2\pi}\int_{\phi=0}^{2\pi} e^{it\phi}d\phi \int_{\rho=0}^{+\infty} J_t(\xi_q\rho)\delta(\rho,0)\rho d\rho \\ & \cdot \int_{z=-\infty}^{+\infty} \mu_v(z)\left(F_z^t(\xi_q,z)\right)^*\delta(z,z_{Tx})dz. \end{aligned} \tag{2.45}$$

By L^2-orthogonality of the exponentials, the load vector is non-zero when $t=0$. Since $J_0(0)=1$, for a z-oriented point source, the right-hand side becomes:

$$l(\mathbf{F}^0) = i\omega\mu_v(z_{Tx})\left(F_z^0(\xi_q,z_{Tx})\right)^*. \tag{2.46}$$

Hence, we obtain the magnetic field by solving the following variational formulation:

$$b(\mathbf{F}^0,\mathbf{H}^0) = l(\mathbf{F}^0),\ \text{for all } \mathbf{F}^0 \in V(\mathbb{R}). \tag{2.47}$$

Lets consider $\mathbf{R}_x$ and $\mathbf{R}_y$ to be the right-hand sides of (2.3) for x and y-oriented sources, respectively. By using (2.44), we obtain:

$$\begin{aligned} \mathbf{R}_x &= \lim_{\rho_{Tx}\to 0^+} \frac{i\omega\mu_h(z)}{2\pi\rho}\delta(\rho,\rho_{Tx})\delta(z,z_{Tx})\left(\frac{e^{-i\phi}}{2}(\hat{\boldsymbol{\rho}}-i\hat{\boldsymbol{\phi}}) + \frac{e^{i\phi}}{2}(\hat{\boldsymbol{\rho}}+i\hat{\boldsymbol{\phi}})\right), \\ \mathbf{R}_y &= \lim_{\rho_{Tx}\to 0^+} \frac{i\omega\mu_h(z)}{2\pi\rho}\delta(\rho,\rho_{Tx})\delta(z,z_{Tx})\left(\frac{e^{-i\phi}}{2}(i\hat{\boldsymbol{\rho}}+\hat{\boldsymbol{\phi}}) - \frac{e^{i\phi}}{2}(i\hat{\boldsymbol{\rho}}-\hat{\boldsymbol{\phi}})\right). \end{aligned} \tag{2.48}$$

Similarly to (2.46), the right-hand side of the variational formulation is non-zero only when $t=-1,1$. For those values of t, and for each Hankel mode, we have:

$$b(\mathbf{F}^t,\mathbf{H}^t) = \lim_{\rho_{Tx}\to 0+} l(\mathbf{F}^t),\ \text{for all } \mathbf{F}^t \in V(\mathbb{R}), \tag{2.49}$$

where,

$$\begin{aligned} l(\mathbf{F}^t) &= i\omega\mu_h(z_{Tx})\Bigg[\frac{F_+^t(\xi_q,z_{Tx})}{2}J_{t+1}(\xi_q\rho_{Tx}) + \frac{F_-^t(\xi_q,z_{Tx})}{2}J_{t-1}(\xi_q\rho_{Tx}) \\ &\quad - t\left(\frac{F_+^t(\xi_q,z_{Tx})}{2}J_{t+1}(\xi_q\rho_{Tx}) - \frac{F_-^t(\xi_q,z_{Tx})}{2}J_{t-1}(\xi_q\rho_{Tx})\right)\Bigg]^* \\ &= i\omega\mu_h(z_{Tx})J_0(\xi_q\rho_{Tx})\begin{cases}\left(F_+^t(\xi_q,z_{Tx})\right)^*, & t=-1,\\ \left(F_-^t(\xi_q,z_{Tx})\right)^*, & t=1.\end{cases} \end{aligned} \tag{2.50}$$

Based on (2.18), we introduce the following notation:

$$\begin{aligned}
\mathcal{H}^t_\rho(\boldsymbol{\rho}) &= \frac{1}{2\pi} e^{-it\phi} \int_{\xi=0}^{+\infty} \Big(H^t_+(\xi, z) J_{t+1}(\xi\rho) + H^t_-(\xi, z) J_{t-1}(\xi\rho) \Big) \xi d\xi, \\
\mathcal{H}^t_\phi(\boldsymbol{\rho}) &= \frac{i}{2\pi} e^{-it\phi} \int_{\xi=0}^{+\infty} \Big(H^t_+(\xi, z) J_{t+1}(\xi\rho) - H^t_-(\xi, z) J_{t-1}(\xi\rho) \Big) \xi d\xi, \\
\mathcal{H}^t_z(\boldsymbol{\rho}) &= \frac{1}{2\pi} e^{-it\phi} \int_{\xi=0}^{+\infty} H^t_z(\xi, z) J_t(\xi\rho) \xi d\xi.
\end{aligned} \tag{2.51}$$

We have $\boldsymbol{\mathcal{H}}^t = (\mathcal{H}^t_\rho, \mathcal{H}^t_\phi, \mathcal{H}^t_z)$. Therefore, the magnetic field for the x-oriented source is:

$$\boldsymbol{\mathcal{H}} = \boldsymbol{\mathcal{H}}^1 + \boldsymbol{\mathcal{H}}^{-1}. \tag{2.52}$$

For a y-oriented source, the field is computed as:

$$\boldsymbol{\mathcal{H}} = i\boldsymbol{\mathcal{H}}^1 - i\boldsymbol{\mathcal{H}}^{-1}. \tag{2.53}$$

2.3. Multiscale Hankel Finite Element Method (Ms-HFEM)

We now describe our multiscale FE method in the Hankel domain. In order to make the computational problem tractable, we truncate our domain along the z direction. We consider $\Omega_z = (z_0, z_N)$ to be our problem domain along z direction and we have $-\infty < z_0$ and $z_N < \infty$. Moreover, we consider our solution to satisfy a zero Dirichlet boundary condition at both ends, since the waves amplitude rapidly decreases as we move away from the source. Thus, we have $\mathbf{H}^m, \mathbf{F}^m \in V_0(\Omega_z)$, where $V_0(\Omega_z) = H^1_0(\Omega_z) \times H^1_0(\Omega_z) \times L^2(\Omega_z)$, with:

$$H^1_0(\Omega_z) = \{v \in H^1(\Omega_z), v(z_i) = 0 \text{ for } z_i \in \partial\Omega_z\}. \tag{2.54}$$

In the following, for simplicity, we shall remove symbols ξ_q and t from the notation. For each Hankel mode, we need to solve three problems associated with $t = -1, 0, 1$. The curl operator is the one defined in (2.24), (2.26) and (2.29). Similarly, Π_+, Π_-, and Π_z are the symbols defined in Equation (2.23), and l is the right-hand side of the variational formulation described in Equations (2.46) and (2.50) for $t = -1, 0, 1$. Our multiscale approach consists of the following steps for each Hankel mode:

(a) **Divide the domain into a finite number of subdomains**. We consider $z_0, z_1, z_2, \cdots, z_{N-1}, z_N$ to be arbitrary real numbers such that

$z_0 < z_1 < \cdots < z_N$ (see Figure 2.2). We refer to them as decomposition points. We define subdomains $\Omega_i = (z_{i-1}, z_i)$, and we have:

$$\overline{\Omega_z} = \bigcup_{i=1}^{N} \overline{\Omega_i}. \tag{2.55}$$

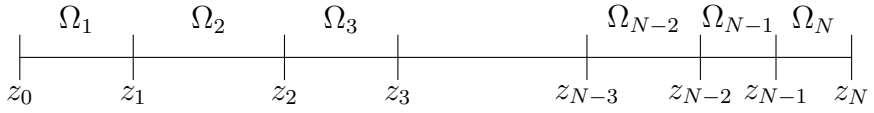

Figure 2.2.: Selected decomposition points $z_0, z_1, \cdots, z_{N-1}, z_N$ of the domain (z_0, z_N). $\Omega_1, \Omega_2, \cdots, \Omega_N$ are the subdomains associated with the decomposition points.

(b) **Decompose the magnetic field into primary and secondary fields**. For each Hankel mode, we decompose our magnetic field as follows:

$$\mathbf{H}(z) = \mathbf{H}^P(z) + \mathbf{H}^S(z), \tag{2.56}$$

where $\mathbf{H}^P$ and $\mathbf{H}^S$ are a primary and a secondary field, respectively.

(c) **Find a local primary field**. Lets assume that $z_{Tx} \in \Omega_p$ (see Figure 2.3). We define our local primary field $\mathbf{H}^P \in V_0(\Omega_p)$ as the one that satisfies:

$$b(\mathbf{F}, \mathbf{H}^P) = l(\mathbf{F}),\ \mathbf{F} \in V_0(\Omega_p). \tag{2.57}$$

Extending the local primary field to the entire domain with zero, we have $\mathbf{H}^P \in V_0(\Omega_z)$. The local primary field has a discontinuous flux at z_{p-1} and z_p. For the special case when the source is located at one decomposition point, we consider $z_{Tx} = z'_p$, where

$$z'_p = \begin{cases} z_{Tx} + 10^{-5}\text{meters} & z_{Tx} = z_{p-1}, \\ z_{Tx} - 10^{-5}\text{meters} & z_{Tx} = z_p. \end{cases} \tag{2.58}$$

The 10^{-5} displacement is an arbitrary choice. We use a small number compatible with our grid size, but other small values are also valid.

(d) **Solve** $(N-1)$ **pairs of local problems**. We consider $\Omega_i^M = \Omega_i \cup \Omega_{i+1} \cup \{z_i\}$, $i = 1, \cdots, (N-1)$. For each subdomain Ω_i^M, we solve a pair of local problems which correspond to a discontinuous flux at the

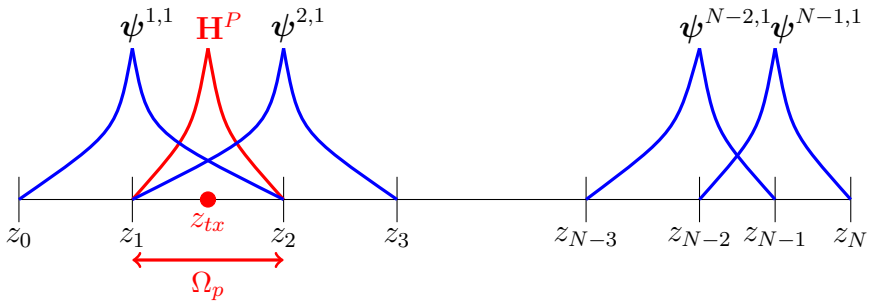

Figure 2.3.: Multiscale basis functions $\boldsymbol{\psi}^{1,1}, \boldsymbol{\psi}^{2,1}, \cdots, \boldsymbol{\psi}^{N-1,1}$ and local primary field $\mathbf{H}^P$. Ω_p is the domain occupied by the local primary field.

node $z = z_i$. Specifically, the flux of the first local problem has a jump equal to $\mathbf{1}_1 = (1, 0, 0)$, and the flux of the second local problem has a jump equal to $\mathbf{1}_2 = (0, 1, 0)$. The local functions $\boldsymbol{\psi}^{i,k} \in V_0(\Omega_i^M)$ solve the following variational problems:

$$b(\mathbf{F}, \boldsymbol{\psi}^{i,k}) = l^{M,k}(\mathbf{F}), \ \mathbf{F} \in V_0(\Omega_i^M), \ i = 1, \cdots, N-1, \ k = 1, 2, \quad (2.59)$$

where $\boldsymbol{\psi}^{i,k}(z) = (\psi_-^{i,k}(z), \psi_+^{i,k}(z), \psi_z^{i,k}(z))$, and $l^{M,k}$ corresponds to the jump of the flux of the solutions at $z = z_i$. Specifically:

$$\begin{aligned} l^{M,1}(\mathbf{F}) &= 2\left(F_-(z_i)\right)^*, \\ l^{M,2}(\mathbf{F}) &= 2\left(F_+(z_i)\right)^*, \\ &\text{for } i = 1, \cdots, N-1. \end{aligned} \quad (2.60)$$

Following a similar process as with the local primary field, we consider the extension by zero of the local solutions on Ω_z, and we have $\boldsymbol{\psi}^{i,k} \in V_0(\Omega_z)$. We denote the solutions of these local problems as multiscale basis functions. We define the following space of multiscale basis functions:

$$V_M = \text{span}\left\{ \left\{ \boldsymbol{\psi}^{i,k}(z) = \left(\psi_-^{i,k}(z), \psi_+^{i,k}(z), \psi_z^{i,k}(z)\right) \right\}_{i=1}^{N-1} \right\}_{k=1}^{2}. \quad (2.61)$$

(e) **Solve the secondary field formulation using the multiscale basis functions**. Since the flux components of the local primary field are discontinuous, we need our secondary field to balance these artificial discontinuities. Thus, by combining the primary and secondary fields, we recover a continuous flux for the full field. From (2.56), we obtain:

$$b(\mathbf{F}, \mathbf{H}^S) = b(\mathbf{F}, \mathbf{H}) - b(\mathbf{F}, \mathbf{H}^P) = l(\mathbf{F}) - b(\mathbf{F}, \mathbf{H}^P), \ \mathbf{F} \in V_0(\Omega_z). \quad (2.62)$$

We describe our secondary field as follows:

$$\mathbf{H}^S(z) = \sum_{i=1}^{N-1} \sum_{k=1}^{2} \alpha_{i,k} \boldsymbol{\psi}^{i,k}(z), \tag{2.63}$$

where $\mathbf{H}^S = (H_-^S, H_+^S, H_z^S)$, and $\boldsymbol{\psi}^{i,k} \in V_M$. By the definition of the multiscale basis functions, (2.63) satisfies the reduced wave equation. Moreover, we consider $\mathbf{F} \in V_M$. Therefore, by substituting (2.63) into (2.62), we have:

$$\begin{aligned} \sum_{i=1}^{N-1} \sum_{k=1}^{2} \alpha_{i,k} b(\boldsymbol{\psi}^{m,n}, \boldsymbol{\psi}^{i,k}) = l(\boldsymbol{\psi}^{m,n}) - b(\boldsymbol{\psi}^{m,n}, \mathbf{H}^P), \\ m = 1, \cdots, N-1, \ n = 1, 2. \end{aligned} \tag{2.64}$$

Finally, we add the local primary field and the secondary field to evaluate the full field.

In the next sections, we further describe the formulation for each step.

2.3.1. Local primary field

We consider the local primary field defined in Equation (2.57). We further decompose our primary field as follows:

$$\mathbf{H}^P = \mathbf{H}^F\Big|_{\Omega_p} + \mathbf{H}^C, \tag{2.65}$$

where $\mathbf{H}^F$ is the fundamental solution of the electromagnetic reduced wave equation and $\mathbf{H}^C$ is a correction field.

Since the fundamental field does not enforce any specific value at the boundaries of Ω_p, the correction field is intended to enforce the zero Dirichlet (tangential) boundary condition on $\mathbf{H}^P$ (see Figure 2.4). We define our correction field as follows:

$$\mathbf{H}^C = \sum_{i=p-1}^{p} \sum_{k=1}^{2} \beta_{i,k} \mathbf{H}^{C,i,k}, \tag{2.66}$$

where $\mathbf{H}^{C,i,k}$ ($i = p-1, p$ and $k = 1, 2$) are the correction basis functions. To define them, we perform the following decomposition:

$$\mathbf{H}^{C,i,k} = \mathbf{H}_0^{C,i,k} + \mathbf{H}_1^{C,i,k}, \ i = p-1, p, \ k = 1, 2, \tag{2.67}$$

where $\mathbf{H}_0^{C,i,k} \in V_0(\Omega_p)$, and $\mathbf{H}_1^{C,i,k} \in V^j(\Omega_p)$ for $j \neq i$ is a lift of the correction field at z_i to impose the non-zero Dirichlet boundary condition. $V^i(\Omega_p) \subset$

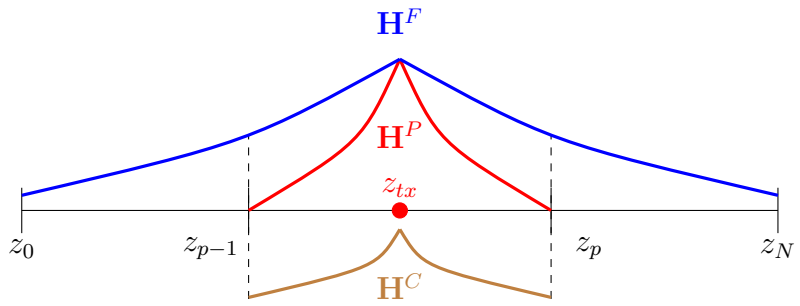

Figure 2.4.: Fundamental, correction and local primary fields.

$V(\Omega_p)$, for $i = p-1, p$ is the space of all vector-valued functions $\mathbf{F} \in V(\Omega_p)$ satisfying a zero Dirichlet (tangential) boundary condition at $z = z_i$. By substituting (2.67) into variational formulation (2.41), we arrive at:

$$b(\mathbf{F}, \mathbf{H}_0^{C,i,k}) = -b(\mathbf{F}, \mathbf{H}_1^{C,i,k}),\ \mathbf{H}_0^{C,i,k},\ \mathbf{F} \in V_0(\Omega_p),\ i = p-1, p,\ k = 1, 2. \quad (2.68)$$

In order to impose a zero Dirichlet (tangential) boundary condition for our local primary field, we enforce the following conditions:

$$\mathbf{n}_j \times \mathbf{H}^C(z_j) = -\mathbf{n}_j \times \mathbf{H}^F(z_j),\ j = p-1,\ p, \quad (2.69)$$

where $\mathbf{n}_{p-1} = -\hat{\mathbf{z}}$ and $\mathbf{n}_p = \hat{\mathbf{z}}$ are the outward unit normal vectors at z_{p-1} and z_p, respectively. Using (2.66), we obtain:

$$\sum_{i=p-1}^{p} \sum_{k=1}^{2} \beta_{i,k} \mathbf{n}_j \times \mathbf{H}^{C,i,k}(z_j) = -\mathbf{n}_j \times \mathbf{H}^F(z_j),\ j = p-1,\ p. \quad (2.70)$$

2.3.2. Secondary field formulation

We define the secondary field to be the difference between the full field and the local primary field. Therefore, we have:

$$\mathbf{H}^S = \mathbf{H} - \mathbf{H}^P. \quad (2.71)$$

Since the flux of the local primary field may be discontinuous on the boundaries of its domain, the flux of the secondary field should be discontinuous on the boundaries of the primary field's domain as follows:

$$[\mathbf{n}_i \times \nabla \times \mathbf{H}^S]_{z_i} = -[\mathbf{n}_i \times \nabla \times \mathbf{H}^P]_{z_i},\ i = p-1,\ p, \quad (2.72)$$

where $\mathbf{n}_{p-1} = -\hat{\mathbf{z}}$ and $\mathbf{n}_p = \hat{\mathbf{z}}$. Thus, the full field has a continuous flux on Ω_z. Hence, the secondary field formulation is given by:

$$\begin{aligned} b(\mathbf{F}, \mathbf{H}^S) = &- \left(Q \cdot \mathbf{F}(z_{p-1})\right)^* Q \cdot \left[\mathbf{n}_{p-1} \times \widetilde{\boldsymbol{\sigma}}^{-1}(z) \nabla \times \mathbf{H}^P\right]_{z_{p-1}} \\ &- \left(Q \cdot \mathbf{F}(z_p)\right)^* Q \cdot \left[\mathbf{n}_p \times \widetilde{\boldsymbol{\sigma}}^{-1}(z) \nabla \times \mathbf{H}^P\right]_{z_p}. \end{aligned} \tag{2.73}$$

We have:

$$\hat{\mathbf{z}} \times \nabla \times \mathbf{H}^P = -\left(\nabla \times \mathbf{H}^P\right)_\phi \hat{\boldsymbol{\rho}} + \left(\nabla \times \mathbf{H}^P\right)_\rho \hat{\boldsymbol{\phi}}. \tag{2.74}$$

Using the fact that $\mathbf{H}^P(z_{p-1}^-) = \mathbf{0}$, and considering (2.74), we obtain:

$$\begin{aligned} -\Big(Q\Big[\hat{\mathbf{z}} \times \widetilde{\boldsymbol{\sigma}}^{-1}(z) \nabla \times \mathbf{H}^P\Big]_{z_{p-1}}\Big)_\rho = \\ \frac{-1}{\sqrt{2}\pi} \widetilde{\sigma}_h^{-1}(z_{p-1}^+) \cdot \sum_{m=-\infty}^{+\infty} e^{-im\phi} \int_0^{+\infty} \Pi_- \left(\mathbf{H}^P\right)(z_{p-1}^+) J_{m-1}(\xi\rho) \xi d\xi. \end{aligned} \tag{2.75}$$

Using the first component of the curl (2.24), we have:

$$\begin{aligned} -\Big(Q\Big[\hat{\mathbf{z}} \times \widetilde{\boldsymbol{\sigma}}^{-1}(z) \nabla \times \mathbf{H}^P\Big]_{z_{p-1}}\Big)_\phi = \\ \frac{-i}{\sqrt{2}\pi} \widetilde{\sigma}_h^{-1}(z_{p-1}^+) \cdot \sum_{m=-\infty}^{+\infty} e^{-im\phi} \int_0^{+\infty} \Pi_+ \left(\mathbf{H}^P\right)(z_{p-1}^+) J_{m+1}(\xi\rho) \xi d\xi. \end{aligned} \tag{2.76}$$

Similarly, since $\mathbf{H}^P(z_p^+) = \mathbf{0}$, the jump on the right boundary of primary field's domain is equal to:

$$\begin{aligned} \Big(Q\Big[\hat{\mathbf{z}} \times \widetilde{\boldsymbol{\sigma}}^{-1}(z) \nabla \times \mathbf{H}^P\Big]_{z_p}\Big)_\rho = \\ \frac{1}{\sqrt{2}\pi} \widetilde{\sigma}_h^{-1}(z_p^-) \cdot \sum_{m=-\infty}^{+\infty} e^{-im\phi} \int_0^{+\infty} \Pi_- \left(\mathbf{H}^P\right)(z_p^-) J_{m-1}(\xi\rho) \xi d\xi, \end{aligned} \tag{2.77}$$

$$\begin{aligned} \Big(Q\Big[\hat{\mathbf{z}} \times \widetilde{\boldsymbol{\sigma}}^{-1}(z) \nabla \times \mathbf{H}^P\Big]_{z_p}\Big)_\phi = \\ \frac{i}{\sqrt{2}\pi} \widetilde{\sigma}_h^{-1}(z_p^-) \cdot \sum_{m=-\infty}^{+\infty} e^{-im\phi} \int_0^{+\infty} \Pi_+ \left(\mathbf{H}^P\right)(z_p^-) J_{m+1}(\xi\rho) \xi d\xi. \end{aligned} \tag{2.78}$$

By using the orthogonality of the Bessel functions and the exponentials, using similar computations to those employed to infer (2.41), we obtain:

$$b(\mathbf{F}, \mathbf{H}^S) = l_p^{S,-}(\mathbf{F}, \mathbf{H}^P) + l_p^{S,+}(\mathbf{F}, \mathbf{H}^P), \text{ for all } \mathbf{F} \in V_0(\Omega_z), \tag{2.79}$$

where

$$
\begin{aligned}
l_p^{S,+}(\mathbf{F},\mathbf{H}^P) =& 2\widetilde{\sigma}_h^{-1}(z_p^-)\Big(F_-^*\Pi_-\left(\mathbf{H}^P\right)+F_+^*\Pi_+\left(\mathbf{H}^P\right)\Big)(z_p^-),\\
l_p^{S,-}(\mathbf{F},\mathbf{H}^P) =& -2\widetilde{\sigma}_h^{-1}(z_{p-1}^+)\Big(F_-^*\Pi_-\left(\mathbf{H}^P\right)+F_+^*\Pi_+\left(\mathbf{H}^P\right)\Big)(z_{p-1}^+).
\end{aligned}
\tag{2.80}
$$

Analogously, by considering the jump condition of the flux of multiscale basis functions, we arrive at (2.60).

2.3.3. Global problem

Using (2.63), (2.79), and the definition of the multiscale basis functions, we obtain:

$$
b(\mathbf{F},\mathbf{H}^S)=\sum_{i=1}^{N-1}\sum_{k=1}^{2}\alpha_{i,k}\mathbf{m}(\mathbf{F},\boldsymbol{\psi}^{i,k}),
\tag{2.81}
$$

where, for an arbitrary test function $\mathbf{F}$ and a multiscale basis function $\boldsymbol{\psi}^{i,k}$:

$$
\mathbf{m}(\mathbf{F},\boldsymbol{\psi}^{i,k})=2\sum_{l=i-1}^{i+1}(Q\cdot\mathbf{F})^*\left[Q\cdot\mathbf{n}_l\times\widetilde{\boldsymbol{\sigma}}^{-1}(z)\nabla\times\boldsymbol{\psi}^{i,k}\right]_{z_l}.
\tag{2.82}
$$

We consider test functions $\mathbf{F}\in V_M$. Hence, by using (2.80), we have:

$$
\begin{aligned}
\sum_{i=1}^{N-1}\sum_{k=1}^{2}\alpha_{i,k}\mathbf{m}(\boldsymbol{\psi}^{m,n},\boldsymbol{\psi}^{i,k}) &= l_p^{S,-}(\boldsymbol{\psi}^{m,n},\mathbf{H}^P)+l_p^{S,+}(\boldsymbol{\psi}^{m,n},\mathbf{H}^P),\\
m=1,\cdots,(N-1),\ n=1,2.&
\end{aligned}
\tag{2.83}
$$

By using (2.23), we can further simplify $\mathbf{m}(.,.)$ to:

$$
\mathbf{m}(\boldsymbol{\psi}^{m,n},\boldsymbol{\psi}^{i,k})=\sum_{l=1}^{N-1}\sum_{s=-,+}(\psi_s^{m,n}(z_l))^*\left[\widetilde{\sigma}_h^{-1}(z)\Pi_s(\boldsymbol{\psi}^{i,k})\right]_{z_l}.
\tag{2.84}
$$

Figure 2.5 illustrates the multiscale Finite Element Method (FEM) described in this section and the dependency of each step of the method on the logging positions.

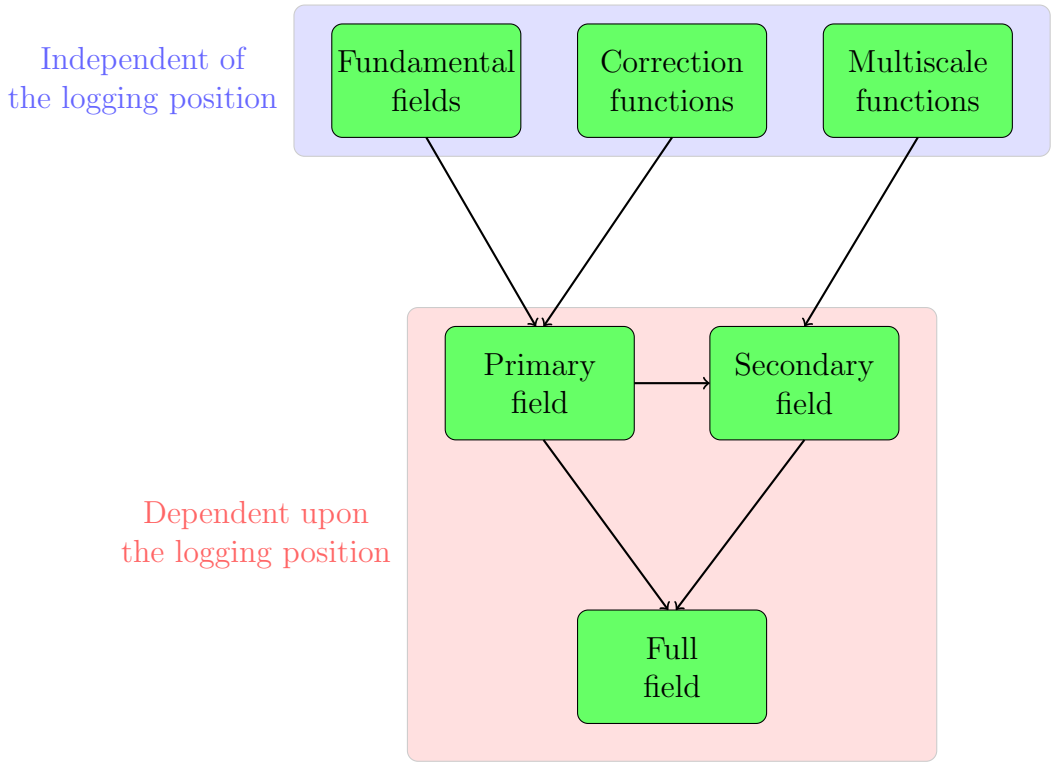

Figure 2.5.: Multiscale FEM. The blue square contains the steps which are independent of the logging position, and the pink square shows the ones which are dependent upon the logging position.

2.4. Implementation

In order to maximize the speed the method, we precompute common operations shared by all Hankel modes. We consider A to be the stiffness matrix obtained from (2.42). By analyzing the dependance upon the Hankel mode ξ, we express:

$$A(\xi, z) = A_0(z) + A_1(z)\xi + A_2(z)\xi^2, \tag{2.85}$$

where A_0, A_1, and A_2 are independent of the Hankel mode. Hence, we precompute the above matrices for all steps of our multiscale method and we reuse them for each Hankel mode. In this way, we only need to construct these stiffness matrices once for all Hankel modes. In addition, the Finite Element (FE) trial and test functions are the same for all Hankel modes. Therefore, we compute them once and reuse them for all Hankel modes.

We employ a direct solver based on LU factorization to solve our system of equations arisen from (2.42). Therefore, when we change the right-hand side of the system of equations, we only need to perform a forward and backward sub-

stitution to recover the solution. However, while performing the experiments, it turns out that in the case of solving the global problem for a large number of logging positions, the aforementioned LU factorization feature is insufficient to achieve the required efficiency for the application. As a partial remedy to this problem, we consider A_g to be the global stiffness matrix obtained using (2.81). Then, for each logging position i, we have:

$$A_g(\xi, z)\mathbf{x}_i = \mathbf{r}_i, \text{ for } i = 1, \cdots, n_p, \tag{2.86}$$

where n_p is the number of logging positions, and $\mathbf{x}_i$ and $\mathbf{r}_i$ are the solution and the right-hand side corresponding to the i-th logging position, respectively. We solve the following set of the system of equations:

$$A_g(\xi, z)\mathbf{y}_j = \mathbf{e}_j, \text{ for } j = 1, \cdots, 2N-2, \tag{2.87}$$

where $\mathbf{e}_j$ are the unit vectors. The right-hand side of (2.86) has only two non-zero components corresponding to the jump of the local primary field. Therefore, we arrive at:

$$\mathbf{x}_i = c_m\mathbf{y}_m + c_n\mathbf{y}_n, \tag{2.88}$$

where c_m and c_n are the non-zero components of the right-hand side of the global problem corresponding to (2.80). Using this approach, for any number of logging positions greater than $2N-2$ (which is usually a much smaller number than the number of logging positions), we save a considerable amount of computational time.

Algorithm 1 incorporates all implementation techniques explained in this section.

Algorithm 1: Multiscale Hankel Finite Element Method (Ms-HFEM).

```
Compute A_0, A_1, A_2, and FE trial and test functions for fundamental fields
Compute A_0, A_1, A_2, and FE trial and test functions for correction basis functions
Compute A_0, A_1, A_2, and FE trial and test functions for multiscale basis functions
for ξ ∈ {ξ_1, ··· , ξ_n} do
    Compute multiscale basis functions
    Compute fundamental fields
    Compute correction basis functions
    for i ∈ {1, ··· , n_p} do
        Compute the local primary field
    for e_j ∈ {e_1, ··· , e_{2N−2}} do
        Solve the global secondary field
    for i ∈ {1, ··· , n_p} do
        Compute the full field
Perform the inverse Hankel transform
```

3. Computing Derivatives

To perform the inversion of Logging-While-Drilling (LWD) resistivity measurements using a gradient-based method, we need to compute the derivatives of the measurements with respect to the inversion variables. In 1D layered media, the inversion variables for the resistivity measurements are the resistivity value of each layer and the bed boundary positions.

In this chapter, we provide an adjoint-state formulation to compute derivatives of resistivity measurements with respect to both the resistivity values and the bed boundary positions. The fundamental idea to obtain such derivatives for the bed boundary positions is to treat the tangential and normal components of the field separately. To do so, we employ a technique that is presented in [58] to compute the derivative of the measurements with respect to the conductivity values. It turns out that when computing derivatives with respect to the bed boundary positions, some adaptations are required in order to derive the correct formula carefully. We first compute the derivatives for a 3D variational formulation. Then, we extend the resulting formulas for the case of a 1.5D variational formulation.

For convenience and to more clearly emphasize the importance of separating the tangential and normal components, in this section, we denote a Transversaly Isotropic (TI) media

$$\boldsymbol{\sigma} = \begin{pmatrix} \sigma_{\mathbf{t}} & 0 & 0 \\ 0 & \sigma_{\mathbf{t}} & 0 \\ 0 & 0 & \sigma_{\mathbf{n}} \end{pmatrix}. \tag{3.1}$$

3.1. Derivatives with respect to bed boundary positions

For the sake of simplicity on the derivation of the adjoint formulation, in this Section we consider a media composed of only two layers, separated by a horizontal interface (see Figure 4.1). Nevertheless, the proposed method easily extends to an arbitrary number of interfaces. In Figure 4.1, z_i indicates the vertical location of the planar interface that separates the two materials. We

denote the corresponding material conductivity as $\boldsymbol{\sigma}_{z_i}$, which is given by:

$$\boldsymbol{\sigma}_{z_i} = \begin{cases} \boldsymbol{\sigma}^- & z < z_i \\ \boldsymbol{\sigma}^+ & z > z_i \end{cases}, \tag{3.2}$$

where $\boldsymbol{\sigma}^+$ and $\boldsymbol{\sigma}^-$ are strictly positive and constant TI tensors. In the following, subscript "z_i" will indicate the material properties, electromagnetic fields, and variational formulations corresponding to this two-layer model problem with the interface located at z_i. Thus, a subscript "$z_i + \epsilon$" indicates the materials, fields, or variational formulations in the same model problem where now the interface is located at $z_i + \epsilon$.

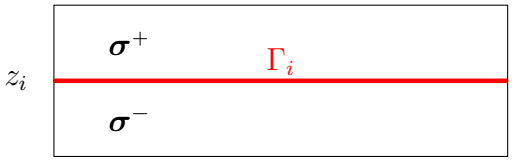

Figure 3.1.: 1D TI media composed of two different materials.

We consider (2.3) and its variational formulation (2.5). We assume that the recorded geophysical resistivity measurements are given by:

$$m(z_i) = \int_\Omega \overline{\mathbf{K}}^T \boldsymbol{\mathcal{H}}_{z_i} + \int_\Omega \overline{\mathbf{G}}^T (\widetilde{\rho}_{z_i} \nabla \times \boldsymbol{\mathcal{H}}_{z_i}), \tag{3.3}$$

for some user-prescribed vector $\mathbf{K}$ and $\mathbf{G}$. The first term in the right-hand-side of (3.3) corresponds to measurements of the magnetic field while the second one represents electric field measurements.

In order to obtain the adjoint-based formula that expresses the derivative of the measurements, it is convenient to introduce the adjoint solution $\boldsymbol{\mathcal{H}}^*_{z_i}$, which satisfies:

$$b_{z_i}(\boldsymbol{\mathcal{H}}^*_{z_i}, \boldsymbol{\mathcal{F}}) = \int_\Omega \overline{\mathbf{K}}^T \boldsymbol{\mathcal{F}} d\Omega + \int_\Omega \overline{\mathbf{G}}^T (\widetilde{\rho}_{z_i} \nabla \times \boldsymbol{\mathcal{F}}), \tag{3.4}$$

where $\boldsymbol{\mathcal{H}}^*_{z_i}$ is selected from the same space as $\boldsymbol{\mathcal{H}}_{z_i}$. From a physical point of view, we obtain the adjoint solution by switching the roles that transmitters and receivers play in our problem. Therefore, we only change the right-hand-side of the original problem (2.5) to obtain the adjoint solution. As a result, we can reuse the matrix factorization employed to solve (2.5), also for the adjoint problem (3.4). Thus, when considering a direct solver, the additional cost of obtaining the adjoint solution is negligible in comparison to that of solving the original forward simulation (see, e.g., [67]).

As a direct application of (3.3) and (3.4), we observe that we recover the measurement value by correlation of the direct and adjoint solutions:

$$b_{z_i}(\boldsymbol{\mathcal{H}}^*_{z_i}, \boldsymbol{\mathcal{H}}_{z_i}) = m(z_i). \tag{3.5}$$

We emphasize that (3.4) and (3.5) are valid for any interface position z_i.

Now, it is possible to differentiate (3.5) with respect to z_i formally. As shown in [58], this technique is very efficient to compute the derivative of the measurement with respect to the conductivity values. Here, we are also interested in computing the derivative with respect to the bed boundary position, and formally differentiate (3.5) leads to the introduction of non-trivial distributions. To avoid this, in here, for a given position z_i, we introduce a small perturbation ϵ and recover the derivative by letting $\epsilon \to 0$. Additionally, the approach presented in [58] requires that the interface must be infinitely long and assumes specific decaying conditions on the electromagnetic fields. On the other hand, the approached proposed here applies in more general settings, including bounded domains.

Since the right-hand-side of (3.4) is independent of $\boldsymbol{\mathcal{H}}^*_{z_i}$, if we select $\boldsymbol{\mathcal{F}} := \boldsymbol{\mathcal{H}}_{z_i+\epsilon}$, we obtain the following identity:

$$b_{z_i+\epsilon}(\boldsymbol{\mathcal{H}}^*_{z_i+\epsilon}, \boldsymbol{\mathcal{H}}_{z_i+\epsilon}) = b_{z_i}(\boldsymbol{\mathcal{H}}^*_{z_i}, \boldsymbol{\mathcal{H}}_{z_i+\epsilon}). \tag{3.6}$$

Similarly, by using (2.5), we have:

$$b_{z_i}(\boldsymbol{\mathcal{H}}^*_{z_i}, \boldsymbol{\mathcal{H}}_{z_i}) = b_{z_i+\epsilon}(\boldsymbol{\mathcal{H}}^*_{z_i}, \boldsymbol{\mathcal{H}}_{z_i+\epsilon}). \tag{3.7}$$

By using Equation (3.5), and subtracting (3.7) from (3.6), we obtain that the difference in the recorded measurements when the interface between the two layers is displaced by ϵ is given by the following integral:

$$\begin{aligned} m(z_i+\epsilon) - m(z_i) &= b_{z_i}(\boldsymbol{\mathcal{H}}^*_{z_i}, \boldsymbol{\mathcal{H}}_{z_i+\epsilon}) - b_{z_i+\epsilon}(\boldsymbol{\mathcal{H}}^*_{z_i}, \boldsymbol{\mathcal{H}}_{z_i+\epsilon}) \\ &= \int_\Omega \left(\nabla \times \overline{\boldsymbol{\mathcal{H}}^*_{z_i}}\right)^T (\widetilde{\boldsymbol{\rho}}_{z_i} - \widetilde{\boldsymbol{\rho}}_{z_i+\epsilon}) \left(\nabla \times \boldsymbol{\mathcal{H}}_{z_i+\epsilon}\right) d\Omega \\ &= \int_{\mathbf{x}_t} \int_{z_i}^{z_i+\epsilon} \left(\nabla \times \overline{\boldsymbol{\mathcal{H}}^*_{z_i}}\right)^T (\widetilde{\boldsymbol{\rho}}_{z_i} - \widetilde{\boldsymbol{\rho}}_{z_i+\epsilon}) \left(\nabla \times \boldsymbol{\mathcal{H}}_{z_i+\epsilon}\right) dx_{\mathbf{n}} d\mathbf{x_t}. \end{aligned} \tag{3.8}$$

At this point, it is critical to treat separately the normal and tangential components of the curl since they satisfy different continuity conditions.

The adequate treatment of the continuity conditions is crucial to obtain the correct formula for the derivative. As we shall see, we obtain different weightings for the normal and tangential contributions of the electromagnetic

fields at the interface. It turns out that it is easy to derive the correct formula with the approach presented in this work. On the other hand, it would be more challenging and mathematically technical to obtain the correct weightings when using a direct approach as in [58]. For each component of the electric field, continuity of the electric displacement implies the following continuity conditions:

$$\begin{aligned} &[(\mathbf{E}_{z_i+\epsilon})_{\mathbf{t}}]_{z_i+\epsilon} = \mathbf{0}, \\ &[\widetilde{\sigma}_{\mathbf{n},z_i+\epsilon}\,(\mathbf{E}_{z_i+\epsilon})_{\mathbf{n}}]_{z_i+\epsilon} = 0, \end{aligned} \tag{3.9}$$

where, symbol $[.]_{z_i+\epsilon}$ denotes the jump across the interface, and $\widetilde{\sigma}_{\mathbf{n},z_i+\epsilon} = \sigma_{\mathbf{n},z_i+\epsilon} - i\omega\varepsilon_0$. By using (2.1), we obtain the following continuity conditions for the curl of the magnetic field:

$$\begin{aligned} &[\widetilde{\rho}_{\mathbf{t},z_i+\epsilon}\,(\nabla \times \boldsymbol{\mathcal{H}}_{z_i+\epsilon})_{\mathbf{t}}]_{z_i+\epsilon} = \mathbf{0}, \\ &[(\nabla \times \boldsymbol{\mathcal{H}}_{z_i+\epsilon})_{\mathbf{n}}]_{z_i+\epsilon} = 0, \end{aligned} \tag{3.10}$$

where $\widetilde{\rho}_{\mathbf{t},z_i+\epsilon} = (\widetilde{\sigma}_{\mathbf{t},z_i+\epsilon})^{-1}$, and $\widetilde{\sigma}_{\mathbf{t},z_i+\epsilon} = \sigma_{\mathbf{t},z_i+\epsilon} - i\omega\varepsilon_0$. Then, we separate explicitly the tangential and normal components in (3.8), and re-arrange them to obtain the following expression:

$$\begin{aligned} m(z_i+\epsilon) - m(z_i) &= \int_{\mathbf{x_t}} \int_{z_i}^{z_i+\epsilon} (\nabla \times \overline{\boldsymbol{\mathcal{H}}^*_{z_i}})^T_{\mathbf{t}} (\widetilde{\rho}_{\mathbf{t},z_i} - \widetilde{\rho}_{\mathbf{t},z_i+\epsilon})(\nabla \times \boldsymbol{\mathcal{H}}_{z_i+\epsilon})_{\mathbf{t}} dx_{\mathbf{n}} d\mathbf{x_t} \\ &+ \int_{\mathbf{x_t}} \int_{z_i}^{z_i+\epsilon} (\nabla \times \overline{\boldsymbol{\mathcal{H}}^*_{z_i}})^T_{\mathbf{n}} (\widetilde{\rho}_{\mathbf{n},z_i} - \widetilde{\rho}_{\mathbf{n},z_i+\epsilon})(\nabla \times \boldsymbol{\mathcal{H}}_{z_i+\epsilon})_{\mathbf{n}} dx_{\mathbf{n}} d\mathbf{x_t} \\ &= -\int_{\mathbf{x_t}} \int_{z_i}^{z_i+\epsilon} (\widetilde{\sigma}_{\mathbf{t},z_i} - \widetilde{\sigma}_{\mathbf{t},z_i+\epsilon})(\widetilde{\rho}_{\mathbf{t},z_i} \nabla \times \overline{\boldsymbol{\mathcal{H}}^*_{z_i}})^T_{\mathbf{t}} (\widetilde{\rho}_{\mathbf{t},z_i+\epsilon} \nabla \times \boldsymbol{\mathcal{H}}_{z_i+\epsilon})_{\mathbf{t}} dx_{\mathbf{n}} d\mathbf{x_t} \\ &+ \int_{\mathbf{x_t}} \int_{z_i}^{z_i+\epsilon} \left(\nabla \times \overline{\boldsymbol{\mathcal{H}}^*_{z_i}}\right)^T_{\mathbf{n}} (\widetilde{\rho}_{\mathbf{n},z_i} - \widetilde{\rho}_{\mathbf{n},z_i+\epsilon}) \left(\nabla \times \boldsymbol{\mathcal{H}}_{z_i+\epsilon}\right)_{\mathbf{n}} dx_{\mathbf{n}} d\mathbf{x_t}, \end{aligned} \tag{3.11}$$

where $\widetilde{\rho}_{\mathbf{n},z_i} = (\widetilde{\sigma}_{\mathbf{n},z_i})^{-1}$. Recalling (3.10), we have:

$$\begin{aligned} \widetilde{\rho}_{\mathbf{t},z_i+\epsilon}\,(\nabla \times \boldsymbol{\mathcal{H}}_{z_i+\epsilon})_{\mathbf{t}} &= \widetilde{\rho}_{\mathbf{t},z_i}\,(\nabla \times \boldsymbol{\mathcal{H}}_{z_i})_{\mathbf{t}} + o(\epsilon), \\ (\nabla \times \boldsymbol{\mathcal{H}}_{z_i+\epsilon})_{\mathbf{n}} &= (\nabla \times \boldsymbol{\mathcal{H}}_{z_i})_{\mathbf{n}} + o(\epsilon). \end{aligned} \tag{3.12}$$

We point out that (3.12) implies that the tangential and normal components of the curl exhibit different convergence behaviors as $\epsilon \to 0$. These different behaviors are complicated to understand when differentiating (3.5) directly, and are of paramount importance to derive the correct formula.

Using Taylor's series expansion, we show that for any smooth function ψ, we have:

$$\begin{aligned}\int_{\Omega}(\widetilde{\rho}_{\mathbf{n},z_i}-\widetilde{\rho}_{\mathbf{n},z_i+\epsilon})\psi(\mathbf{x_t},z)d\mathbf{x} &= \int_{\mathbf{x_t}}\int_{z_i}^{z_i+\epsilon}(\widetilde{\rho}_{\mathbf{n},z_i}-\widetilde{\rho}_{\mathbf{n},z_i+\epsilon})\psi(\mathbf{x_t},z)dx_{\mathbf{n}}d\mathbf{x_t}\\ &= -\int_{\mathbf{x_t}}\int_{z_i}^{z_i+\epsilon}[\widetilde{\rho}_{\mathbf{n}}]\left(\psi(\mathbf{x_t},z_i)+o(\epsilon)\right)dx_{\mathbf{n}}d\mathbf{x_t}\\ &= -\int_{\mathbf{x_t}}\epsilon[\widetilde{\rho}_{\mathbf{n}}]\left(\psi(\mathbf{x_t},z_i)+o(\epsilon)\right)d\mathbf{x_t}\\ &= -\epsilon[\widetilde{\rho}_{\mathbf{n}}]\int_{\Gamma_{z_i}}\psi(\mathbf{x_t},z_i)d\Gamma_{z_i}+o(\epsilon^2),\end{aligned} \tag{3.13}$$

where Γ_{z_i} is the interface between the two materials. Following an analogous argument for the tangential component, and summing up both tangential and normal components according to (3.11), we obtain:

$$\begin{aligned}\frac{m(z_i+\epsilon)-m(z_i)}{\epsilon} =& [\widetilde{\sigma}_{\mathbf{t}}]\int_{\Gamma_{z_i}}\left(\widetilde{\rho}_{\mathbf{t},z_i}\left(\nabla\times\overline{\boldsymbol{\mathcal{H}}^*_{z_i}}\right)_{\mathbf{t}}\right)^T\left(\widetilde{\rho}_{\mathbf{t},z_i}\left(\nabla\times\boldsymbol{\mathcal{H}}_{z_i}\right)_{\mathbf{t}}\right)d\Gamma_{z_i}\\ &-[\widetilde{\rho}_{\mathbf{n}}]\int_{\Gamma_{z_i}}(\nabla\times\overline{\boldsymbol{\mathcal{H}}^*_{z_i}})^T_{\mathbf{n}}(\nabla\times\boldsymbol{\mathcal{H}}_{z_i})_{\mathbf{n}}d\Gamma_{z_i}+o(\epsilon).\end{aligned} \tag{3.14}$$

Finally, letting $\epsilon\to 0$, we have:

$$\begin{aligned}\frac{dm}{dz_i}(z_i) =& [\widetilde{\sigma}_{\mathbf{t}}]\int_{\Gamma_{z_i}}\left(\widetilde{\rho}_{\mathbf{t},z_i}\nabla\times\overline{\boldsymbol{\mathcal{H}}^*_{z_i}}\right)^T_{\mathbf{t}}\left(\widetilde{\rho}_{\mathbf{t},z_i}\nabla\times\boldsymbol{\mathcal{H}}_{z_i}\right)_{\mathbf{t}}d\Gamma_{z_i}\\ &-[\widetilde{\rho}_{\mathbf{n}}]\int_{\Gamma_{z_i}}(\nabla\times\overline{\boldsymbol{\mathcal{H}}^*_{z_i}})^T_{\mathbf{n}}(\nabla\times\boldsymbol{\mathcal{H}}_{z_i})_{\mathbf{n}}d\Gamma_{z_i}.\end{aligned} \tag{3.15}$$

From the geophysical point of view, Equation (3.15) implies that we need to treat differently the normal and tangential components of the electromagnetic fields in order to find the derivatives of the acquired measurements with respect to the bed boundary positions. This separate treatment is due to the different continuity conditions that exist for the different components of the electromagnetic fields.

Using (2.42) and (3.15), for each Hankel mode ξ_q, the 1.5D derivative of the magnetic field with respect to a bed boundary position becomes:

$$\begin{aligned}\frac{dm}{dz_i}(z_i) =& 2[\widetilde{\sigma}_{\mathbf{t}}]_{z_i}\left(\widetilde{\rho}_{\mathbf{t}}\overline{\Pi^{\xi_q}_{-}(\mathbf{H}^{*,m})}\widetilde{\rho}_{\mathbf{t}}\Pi^{\xi_q}_{-}(\mathbf{H}^{m})+\widetilde{\rho}_{\mathbf{t}}\overline{\Pi^{\xi_q}_{+}(\mathbf{H}^{*,m})}\widetilde{\rho}_{\mathbf{t}}\Pi^{\xi_q}_{+}(\mathbf{H}^{m})\right)(z_i)\\ &-[\widetilde{\rho}_{\mathbf{n}}]_{z_i}\left(\overline{\Pi^{\xi_q}_{z}(\mathbf{H}^{*,m})}\Pi^{\xi_q}_{z}(\mathbf{H}^{m})\right)(z_i).\end{aligned} \tag{3.16}$$

3.2. Derivatives with respect to resistivity values

In this section, for the sake of simplicity, we define $\widetilde{\boldsymbol{\rho}} = (\boldsymbol{\sigma} - i\omega\boldsymbol{\varepsilon})^{-1}$ to indicate the material property corresponding to a given electromagnetic field $\boldsymbol{\mathcal{H}}_{\widetilde{\rho}}$. Therefore, we have:

$$\widetilde{\boldsymbol{\rho}} - \boldsymbol{\epsilon}_i := \begin{cases} \widetilde{\boldsymbol{\rho}} - \epsilon\mathbf{I} & z \in \Omega_i \\ \widetilde{\boldsymbol{\rho}} & \text{otherwise} \end{cases}, \tag{3.17}$$

where for a 1D layered media consist of N layers Ω_i corresponds to i-th layer, and we have $\Omega = \bigcup_{i=1}^{N} \overline{\Omega_i}$.

Similar to (3.3), we have:

$$m(\widetilde{\boldsymbol{\rho}}) = \int_{\Omega} \overline{\mathbf{K}}^T \boldsymbol{\mathcal{H}}_{\widetilde{\rho}} + \int_{\Omega} \overline{\mathbf{G}}^T (\widetilde{\boldsymbol{\rho}} \nabla \times \boldsymbol{\mathcal{H}}_{\widetilde{\rho}}). \tag{3.18}$$

So the adjoint solution $\boldsymbol{\mathcal{H}}^*_{\widetilde{\rho}}$ satisfies (3.4). Therefore, we have the following:

$$b_{\widetilde{\rho}}(\boldsymbol{\mathcal{H}}^*_{\widetilde{\rho}}, \boldsymbol{\mathcal{H}}_{\widetilde{\rho}}) = m(\widetilde{\boldsymbol{\rho}}). \tag{3.19}$$

Relations similar to (3.6) and (3.7) hold for the above definition. Therefore, we have:

$$\begin{aligned} m(\widetilde{\boldsymbol{\rho}} + \boldsymbol{\epsilon}_i) - m(\widetilde{\boldsymbol{\rho}}) &= b_{\widetilde{\rho}}(\boldsymbol{\mathcal{H}}^*_{\widetilde{\rho}}, \boldsymbol{\mathcal{H}}_{\widetilde{\rho}+\boldsymbol{\epsilon}_i}) - b_{\widetilde{\rho}+\boldsymbol{\epsilon}_i}(\boldsymbol{\mathcal{H}}^*_{\widetilde{\rho}}, \boldsymbol{\mathcal{H}}_{\widetilde{\rho}+\boldsymbol{\epsilon}_i}) \\ &= \int_{\Omega} \left(\nabla \overline{\boldsymbol{\mathcal{H}}^*_{\widetilde{\rho}}}\right)^T \cdot ((\widetilde{\boldsymbol{\rho}} + \boldsymbol{\epsilon}_i) - \widetilde{\boldsymbol{\rho}}) \cdot \nabla \boldsymbol{\mathcal{H}}_{\widetilde{\rho}+\boldsymbol{\epsilon}_i} d\Omega. \end{aligned} \tag{3.20}$$

Since the perturbation $\boldsymbol{\epsilon}_i$ only changes the material property of the i-th layer, we arrive at:

$$m(\widetilde{\boldsymbol{\rho}} + \boldsymbol{\epsilon}_i) - m(\widetilde{\boldsymbol{\rho}}) = \epsilon \int_{\Omega_i} \left(\nabla \overline{\boldsymbol{\mathcal{H}}^*_{\widetilde{\rho}}}\right)^T \nabla \boldsymbol{\mathcal{H}}_{\widetilde{\rho}+\boldsymbol{\epsilon}_i} d\Omega. \tag{3.21}$$

By letting $\epsilon \to 0$, we obtain

$$\frac{dm(\widetilde{\boldsymbol{\rho}})}{d\widetilde{\boldsymbol{\rho}}_i} = \int_{\Omega_i} (\nabla \times \overline{\boldsymbol{\mathcal{H}}^*_{\widetilde{\rho}}})^T (\nabla \times \boldsymbol{\mathcal{H}}_{\widetilde{\rho}}) d\Omega_i. \tag{3.22}$$

Using the chain rule, we obtain:

$$\frac{dm(\widetilde{\boldsymbol{\rho}})}{d\boldsymbol{\rho}_i} = \int_{\Omega_i} (\nabla \times \boldsymbol{\mathcal{H}}^*_{\widetilde{\rho}})^T \boldsymbol{\sigma}_i^2 \widetilde{\boldsymbol{\rho}}_i^2 (\nabla \times \boldsymbol{\mathcal{H}}_{\widetilde{\rho}}) d\Omega_i, \tag{3.23}$$

where $\boldsymbol{\rho}_i = \boldsymbol{\sigma}_i^{-1}$ is the resistivity tensor of the media corresponding to the i-th layer.

Hence, by using (2.42), for each Hankel mode ξ_q, the derivative with respect to a resistivity value for a 1.5D variational formulation becomes:

$$\begin{aligned}\frac{dm(\widetilde{\boldsymbol{\rho}})}{d\boldsymbol{\rho}_i} &= 2\int_{z_{i-1}}^{z_i} \overline{\Pi_-^{\xi_q}\left(\mathbf{H}^{*,m}\right)}\left(\sigma_{i,t}^2\widetilde{\rho}_{i,t}^2\right)\Pi_-^{\xi_q}\left(\mathbf{H}^m\right)dz \\ &+ 2\int_{z_{i-1}}^{z_i} \overline{\Pi_+^{\xi_q}\left(\mathbf{H}^{*,m}\right)}\left(\sigma_{i,t}^2\widetilde{\rho}_{i,t}^2\right)\Pi_+^{\xi_q}\left(\mathbf{H}^m\right)dz \\ &+ \xi_q^2\int_{z_{i-1}}^{z_i} \overline{\Pi_z^{\xi_q}\left(\mathbf{H}^{*,m}\right)}\left(\sigma_{i,n}^2\widetilde{\rho}_{i,n}^2\right)\Pi_z^{\xi_q}\left(\mathbf{H}^m\right)dz.\end{aligned} \tag{3.24}$$

4. Numerical Results

In this chapter, we verify our formulations via numerical examples. We first consider measurements acquired with traditional Logging-While-Drilling (LWD) instruments. Then, we compute the derivatives of the aforementioned measurements and compare the results vs a finite difference approach.

4.1. Physical considerations and measurements

For simplicity and to compare our numerical method directly with state-of-the-art analytic implementations [53], we assume $\boldsymbol{\mu} = \mu_0 \mathbf{I}_3$ and $\boldsymbol{\varepsilon} = \varepsilon_0 \mathbf{I}_3$ ($\mathbf{I}_3$ is the 3D identity matrix) to be constant. ε_0 is set to $8.85 \times 10^{-12}(F/m)$, which corresponds to the free-space permittivity, while the magnetic permeability constant μ_0 is set to $4\pi \times 10^{-7}(H/m)$.

We consider each layer as a subdomain of our HFEM. Thus, the decomposition points coincide with the boundaries of our layers. By doing so, we can evaluate the local primary fields in subdomains which have smoothly varying materials. In particular, if we assume that the layer properties are homogeneous, the fundamental solution in (2.65) is independent of the tool position. Moreover, the correction basis functions are also independent of the tool position. Consequently, instead of solving one primary field for each tool position, we find one fundamental field and four correction basis functions per layer. This simplification allows us to increase the speed of the method almost by a factor equal to the number of tool positions.

In our model problem, we consider two different Cartesian coordinate systems: (a) a system of coordinates related to the Earth, and (b) a system of coordinates related to the logging device, which consists of a rotation of the Earth system of coordinates in a way that the logging device extends along the z direction. We denote the angle between the logging instrument and the z direction of the Earth system of coordinates as α (relative dip angle). β is the azimuthal angle (see Figure 4.1). The following rotation matrix gives the transformation between the systems of coordinates of the Earth and the logging device:

$$\boldsymbol{\mathcal{H}}_b = \mathbf{R}^{-1} \boldsymbol{\mathcal{H}}_e \mathbf{R}, \tag{4.1}$$

where rotation $\mathbf{R}$ is defined by the following composition of rotations:

$$\mathbf{R} = \begin{bmatrix} \cos\beta & -\sin\beta & 0 \\ \sin\beta & \cos\beta & 0 \\ 0 & 0 & 1 \end{bmatrix} \cdot \begin{bmatrix} \cos\alpha & 0 & \sin\alpha \\ 0 & 1 & 0 \\ -\sin\alpha & 0 & \cos\alpha \end{bmatrix}.$$

In this notation, subscripts e and b denote the Earth system of coordinates and the logging instrument system of coordinates, respectively. If the logging instrument is perpendicular to the layering of the medium, we have $\alpha = 0$.

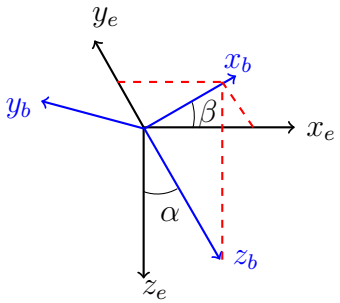

Figure 4.1.: x_e, y_e and z_e are the axes of the Cartesian coordinates. x_b, y_b and z_b are the axes of the borehole coordinates. α and β are the dip and azimuthal angles, respectively.

In this work, for simplicity, we consider $\beta = 0$. Hence, the possibly non-zero couplings of the magnetic field can only be xx, xz, yy, zx and zz, where the first and the second letters in the subscript indicate the transmitter and receiver directions, respectively.

In this work, we consider LWD tools equipped with magnetic dipole sources. We consider a traditional symmetric LWD instrument, which is a standard tool similar to those offered by oil service companies containing two transmitters and two receivers. In the aforementioned instrument, the receivers and transmitters are located symmetrically with respect to the tool center (see Figures 4.2 and 4.6) [52].

In practice, LWD tools often measure the so-called attenuation and phase difference because of their relative insensitivity to the borehole size and mud resistivity. Therefore, to analyze the result of our experiments and compare them against those typically obtained in borehole resistivity applications, we further postprocess the values of the magnetic field. For the most important component, namely the zz-coupling, we compute the magnetic field $\mathcal{H}_{zz}$ at two different receivers. We denote these values as $\mathcal{H}_{zz}(Rx_1)$ and $\mathcal{H}_{zz}(Rx_2)$, which correspond to the first and the second receiver, respectively. To simplify, we

introduce the notation

$$H_l^k = H_{zz}^k(Rx_l), \quad (1 \leqslant k, l \leqslant 2) \tag{4.2}$$

to denote the quantity measured at the receiver l when the transmitter k is active. For $l = 1, 2$, attenuation A^l and phase difference P^l are defined from H_1^l and H_2^l as:

$$\ln \frac{H_1^l}{H_2^l} = \underbrace{\ln \frac{\left|H_1^l\right|}{\left|H_2^l\right|}}_{\times 20\log(e)=A^l(dB)} + i \underbrace{\left(ph(H_1^l) - ph(H_2^l)\right)}_{\times \frac{180}{\pi}=P^l(\text{degree})}, \tag{4.3}$$

where ph denotes the phase of a complex number. The final attenuation A and phase difference P are defined by averaging:

$$A = \frac{1}{2}\left(A^1 + A^2\right), \quad P = \frac{1}{2}\left(P^1 + P^2\right). \tag{4.4}$$

Subsequently, we compute the relation between attenuation and resistivity in a homogeneous media using a table look-up algorithm. This transformation, when applied to a heterogeneous media, delivers the *apparent resistivity* based on attenuation (see [65, 31, 26]). We similarly define the so-called apparent resistivity based on the phase difference.

For the inverse Hankel transform, we use a fast Hankel transform algorithm based on digital filters (see [41] for details).

4.1.1. Derivatives of the measurements

Assuming we are able to compute the derivatives of the magnetic field components with respect to the bed boundary positions or resistivity values, in this section we obtain the derivatives of the attenuation and phase difference by repeatedly applying the chain rule. To do so, we recall:

$$\begin{aligned} A^l := \ln \frac{\left|H_1^l\right|}{\left|H_2^l\right|} &= \ln \frac{\sqrt{\left(H_1^{l,re}\right)^2 + \left(H_2^{l,im}\right)^2}}{\sqrt{\left(H_2^{l,re}\right)^2 + \left(H_2^{l,im}\right)^2}} \\ &= \frac{1}{2}\ln\left[\left(H_1^{l,re}\right)^2 + \left(H_1^{l,im}\right)^2\right] - \frac{1}{2}\ln\left[\left(H_2^{l,re}\right)^2 + \left(H_2^{l,im}\right)^2\right] \end{aligned} \tag{4.5}$$

where $H_1 = H_1^{l,re} + iH_1^{l,im}$ and $H_2 = H_2^{l,re} + iH_2^{l,im}$. Lets assume that $\mathcal{D}$ is the linear operator which delivers the derivative of the magnetic field with respect

to a bed boundary position or a resistivity value. Then, using the chain rule, we have:

$$\begin{aligned}\mathcal{D}(A) = &\frac{1}{\left|H_1^l\right|^2}\left(H_1^{l,re}\mathcal{D}(H_1^{l,re}) + H_1^{l,im}\mathcal{D}(H_1^{l,im})\right)\\ &- \frac{1}{\left|H_2^l\right|^2}\left(H_2^{l,re}\mathcal{D}(H_2^{l,re}) + H_2^{l,im}\mathcal{D}(H_2^{l,im})\right)\end{aligned} \tag{4.6}$$

For the phase difference, it holds that

$$P := ph(H_1) - ph(H_2) = \arctan\left(\frac{H_1^{l,im}}{H_1^{l,re}}\right) - \arctan\left(\frac{H_2^{l,im}}{H_2^{l,re}}\right). \tag{4.7}$$

Using again the chain rule, we obtain:

$$\begin{aligned}\mathcal{D}(P) = &\frac{1}{\left|H_1^l\right|^2}\left(H_1^{l,re}\mathcal{D}(H_1^{l,im}) - H_1^{l,im}\mathcal{D}(H_1^{l,re})\right)\\ &- \frac{1}{\left|H_2^l\right|^2}\left(H_2^{l,re}\mathcal{D}(H_2^{l,im}) - H_2^{l,im}\mathcal{D}(H_2^{l,re})\right).\end{aligned} \tag{4.8}$$

4.2. Verifications

4.2.1. Multiscale Hankel Finite Element Method (Ms-HFEM)

4.2.1.1. Model problem A: Two-layered media

We consider the logging instrument described in Figure 4.2. Figures 4.3 through 4.5 describe the apparent resistivities (logs) for different dip angles. The distance between two consecutive logging points is half a foot (0.1524 m), as this is the resolution provided by most commercial logging-while-drilling (LWD) devices. In all cases, our simulation framework delivers a perfect agreement with the semi-analytic solutions. The large apparent resistivity values observed in Figures 4.4 and 4.5 form the so-called horns. They are a typical artifact that appears due to the employed post-processing method [23, 87]. Moreover, they do not affect significantly to the interpretation of the results.

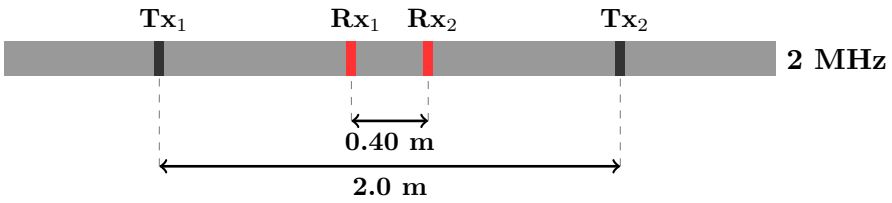

Figure 4.2.: Model problem A. Logging instrument. Tx_1 and Tx_2 are the induction transmitters, and Rx_1 and Rx_2 are the receivers.

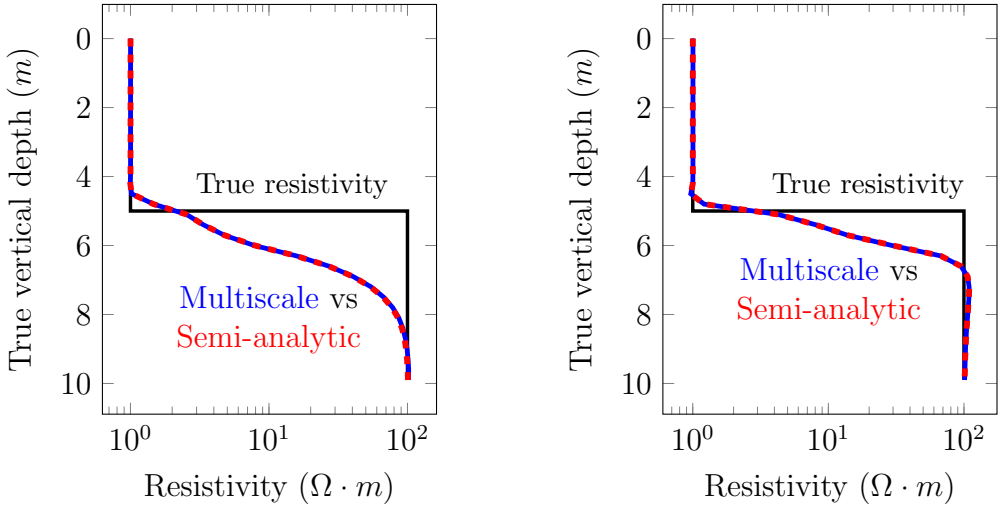

(a) Apparent resistivity based on attenuation

(b) Apparent resistivity based on phase difference

Figure 4.3.: Model problem A. Apparent resistivities for the zz coupling for a vertical well (dip angle = 0°).

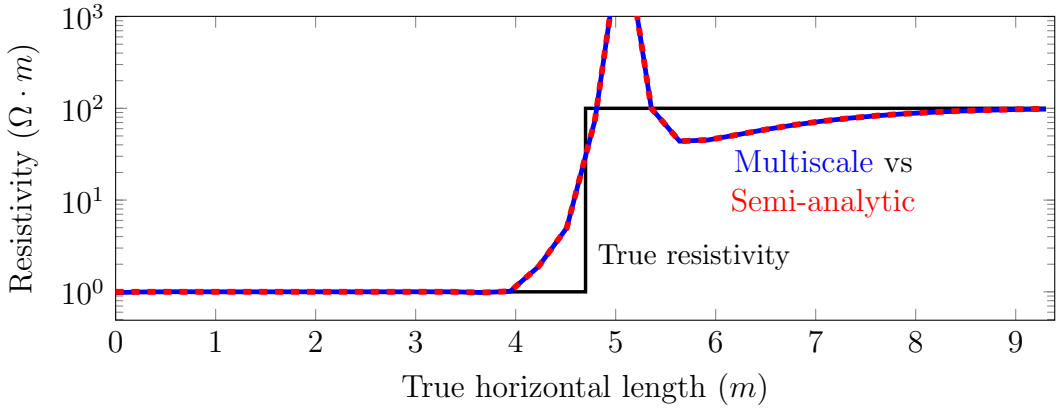

(a) Apparent resistivity based on attenuation

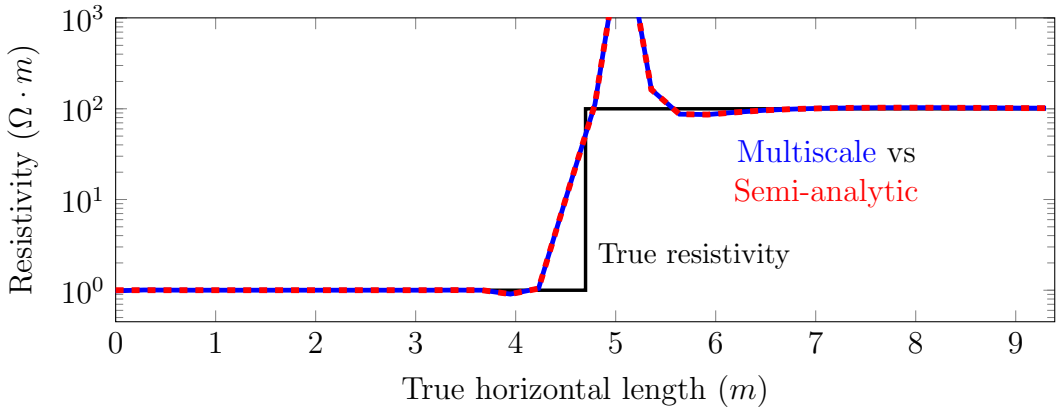

(b) Apparent resistivity based on phase difference

Figure 4.4.: Model problem A. Apparent resistivity for the zz coupling for a 70° deviated well.

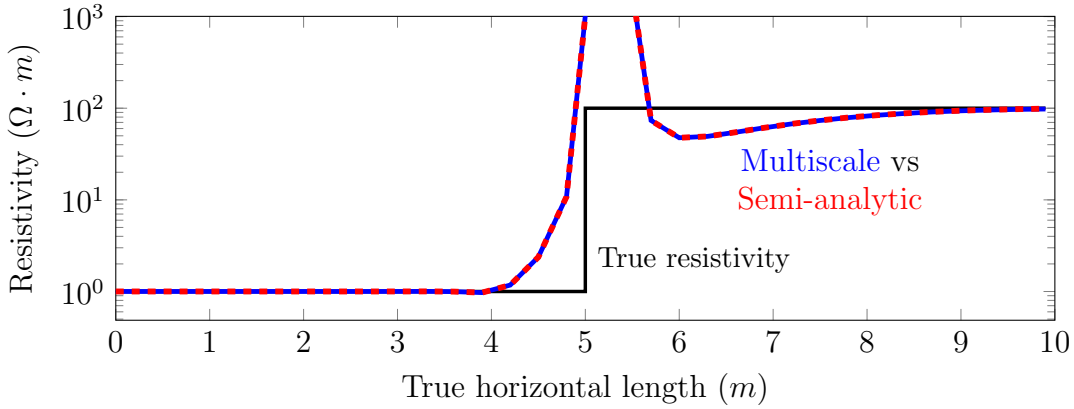

(a) Apparent resistivity based on attenuation

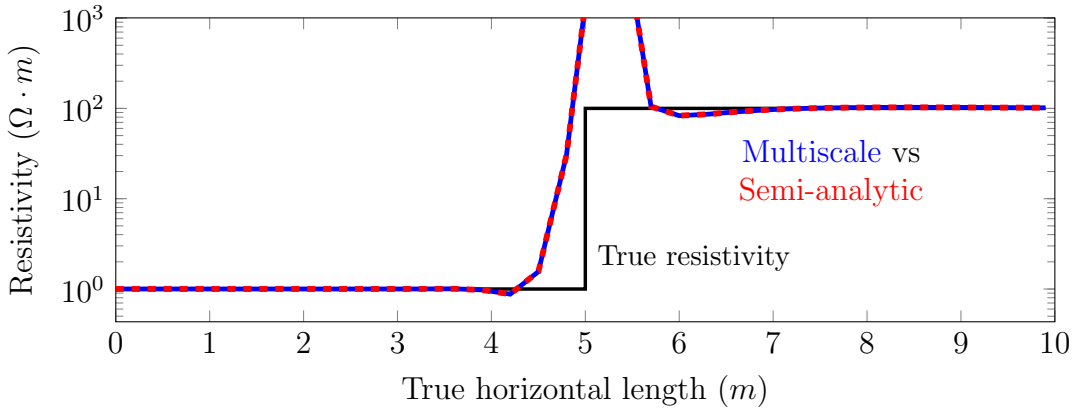

(b) Apparent resistivity based on phase difference

Figure 4.5.: Model problem A. Apparent resistivity for the zz coupling for a 89° deviated well.

4.2.1.2. Model problem B: Multi-layered media

Figure 4.6 describes the logging instrument employed for this example. As in our previous examples, the distance between two consecutive logging points is half a foot (0.1524 m). The main result in terms of apparent resistivities for this model problem for a vertical well is shown in Figure 4.7. The attenuations and phase differences for this case are shown in Figures 4.8 and 4.9, respectively. As before, the numerical solutions coincide with the semi-analytic ones.

Figure 4.10 compares the average computational time needed to solve one tool position using: (a) a traditional FE method, (b) a traditional FE method

when we reuse the LU factorization, and (c) our proposed multiscale method. As shown in the figure, reusing the LU factorization worsens the situation since we need a more refined grid to model for all source positions accurately. Table 4.1 provides a time comparison between a highly-optimized semi-analytic method and the proposed numerical method. For a single tool position, computing the local primary field and pre-computing the multiscale basis functions is computationally expensive and we observe a significant discrepancy between numerical and semi-analytic solutions. However, as expected, by increasing the number of tool positions, the ratio between the time of the proposed numerical method and the semi-analytic one is decreasing. Figure 4.11 shows the average time used to solve one tool position. Using a multiscale method, the average time per position rapidly decreases as we augment the total number of tool positions. This occurs because the pre-computed multiscale basis functions, fundamental fields, and correction basis functions only need to be computed once for any number of tool positions. The results in terms of apparent resistivities for this model problem for 60° and 89° deviated wells are shown in Figures 4.12 and 4.13, respectively. Again, the numerical and semi-analytic solutions coincide.

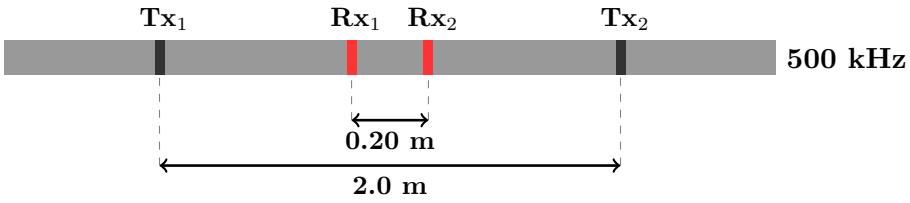

Figure 4.6.: Model problem B. Logging instrument. Tx_1 and Tx_2 are the induction transmitters, and Rx_1 and Rx_2 are the receivers.

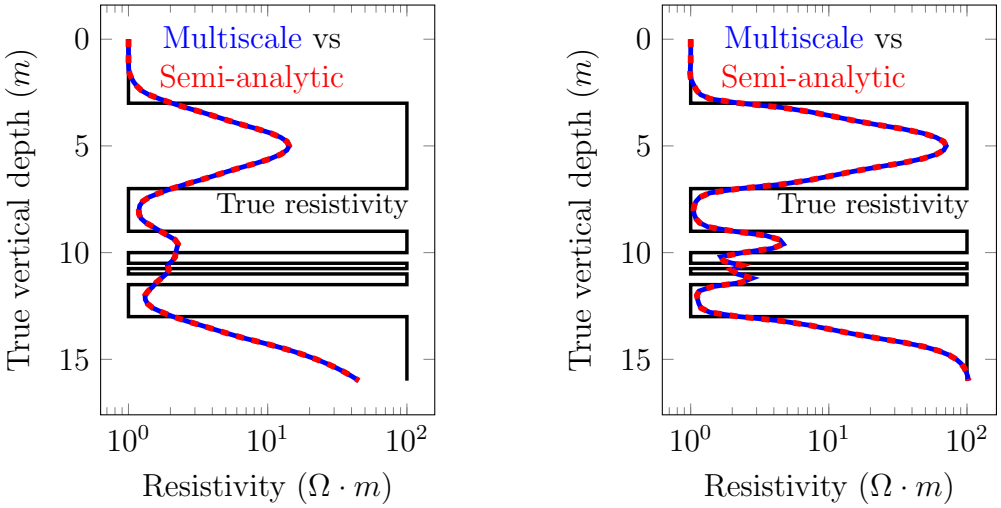

(a) Apparent resistivity based on attenuation

(b) Apparent resistivity based on phase difference

Figure 4.7.: Model problem B. Apparent resistivities for the zz coupling for a vertical well (dip angle = 0°).

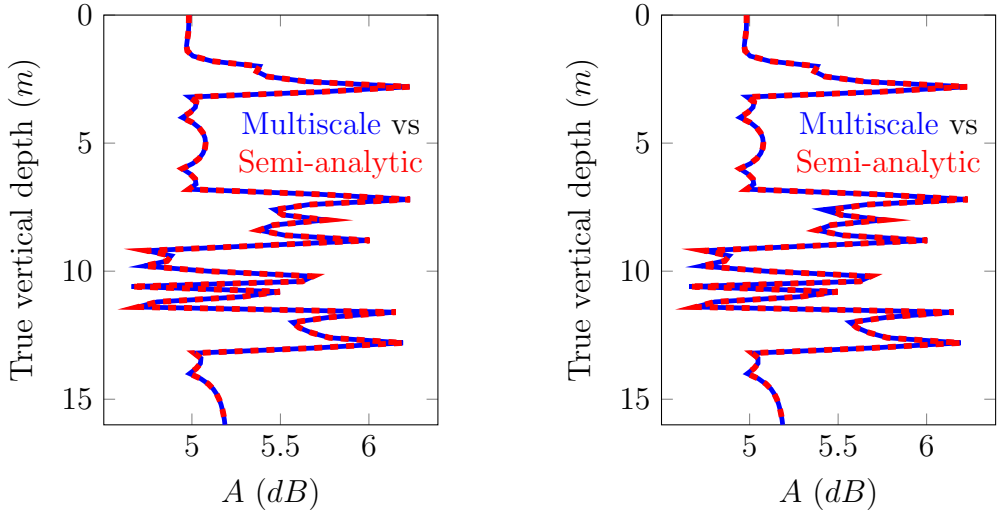

(a) xx coupling

(b) yy coupling

Figure 4.8.: Model problem B. Attenuations for the non-zero couplings (xx and yy couplings) of the magnetic field for a vertical well (dip angle = 0°).

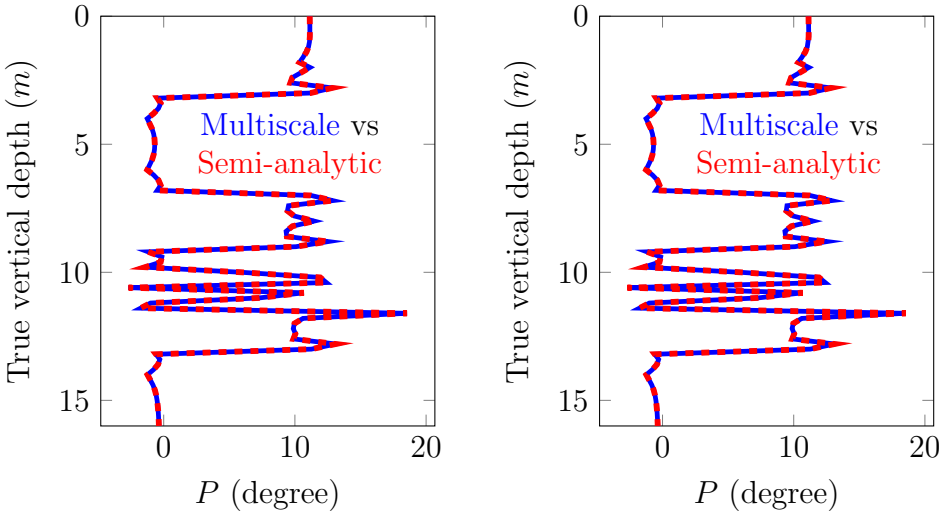

(a) xx coupling (b) yy coupling

Figure 4.9.: Model problem B. Phase differences for the non-zero couplings (xx and yy couplings) of the magnetic field for a vertical well (dip angle = 0°).

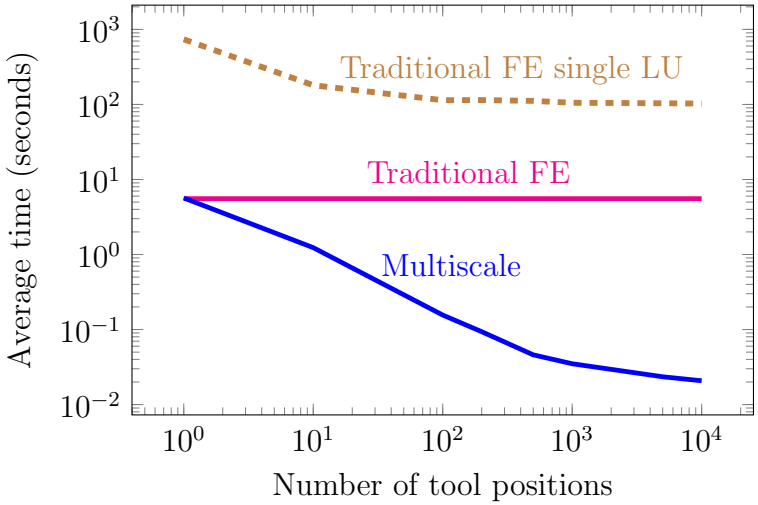

Figure 4.10.: Model problem B. Average time (in seconds) to solve for a single tool position as the number of logging positions varies using (a) a traditional FE approach, (b) a FE approach where we reuse the LU factorization, and (c) our proposed multiscale method $(\frac{\text{time(seconds)}}{\text{number of tool positions}})$.

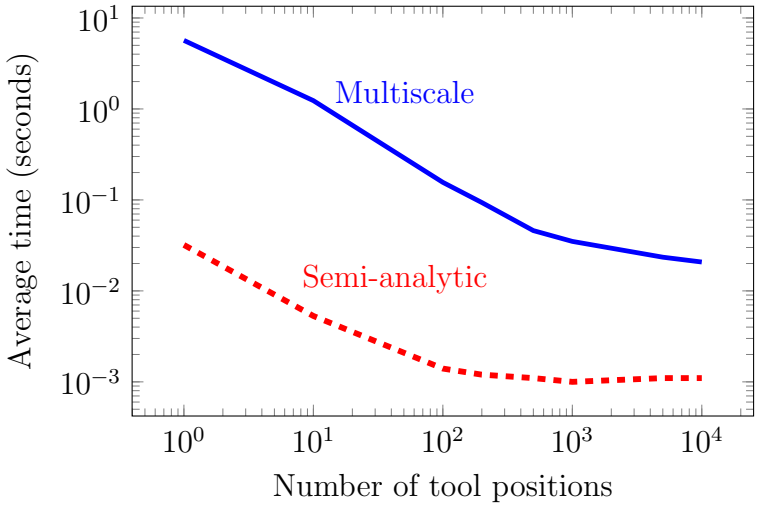

Figure 4.11.: Model problem B. Average time (in seconds) to solve for a single tool position as the number of tool positions varies $(\frac{\text{time(seconds)}}{\text{number of tool positions}})$.

Positions	**Semi-analytic**	**Numerical**	**Ratio**
1	3.2×10^{-2}	5.67	177.19
10	5.3×10^{-2}	12.34	232.83
100	1.4×10^{-1}	15.60	111.43
200	2.4×10^{-1}	18.73	76.54
500	4.1×10^{-1}	23.10	56.34
1000	1.01	35.52	35.16
5000	5.68	115.47	20.65
10000	11.57	207.61	17.94

Table 4.1.: Model problem B. A time comparison (in seconds) for a vertical well using a semi-analytic method and the proposed multiscale FEM as a function of the number of tool positions.

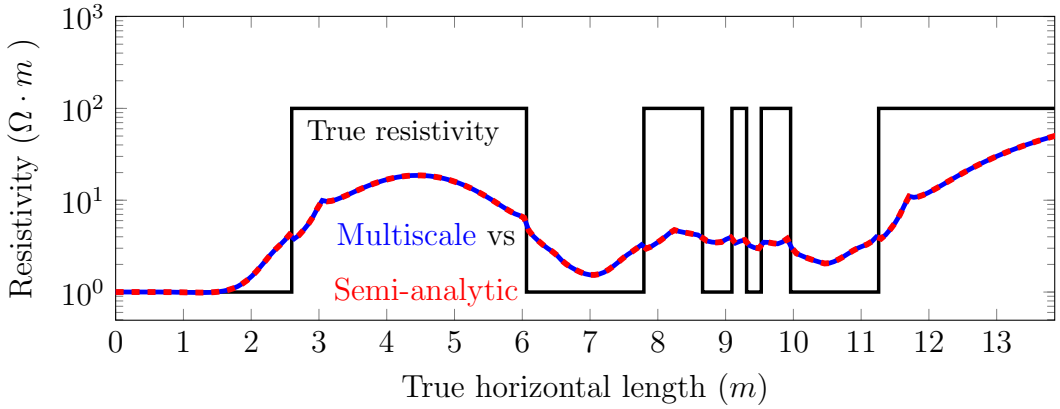

(a) Apparent resistivity based on attenuation

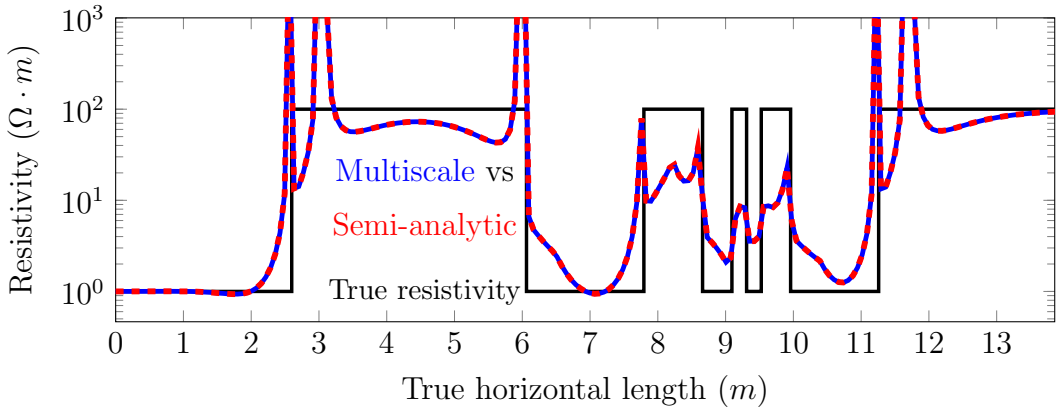

(b) Apparent resistivity based on phase difference

Figure 4.12.: Model problem B. Apparent resistivity for the zz coupling for a 60° deviated well.

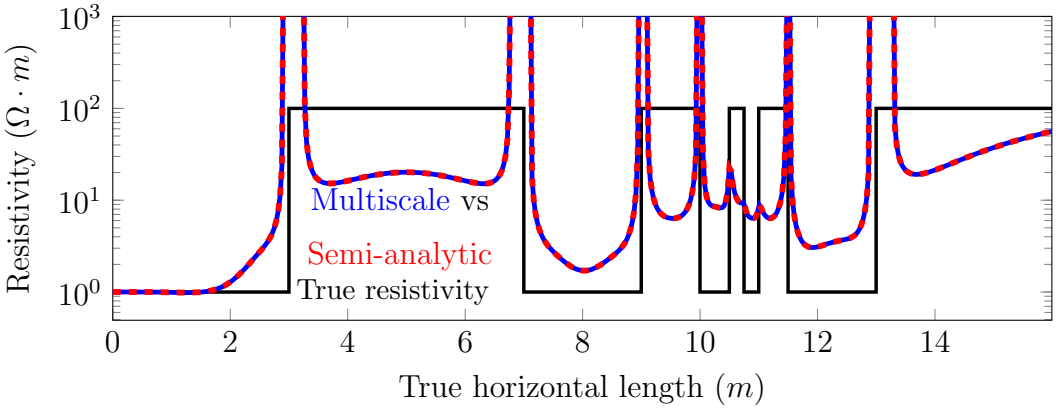

(a) Apparent resistivity based on attenuation

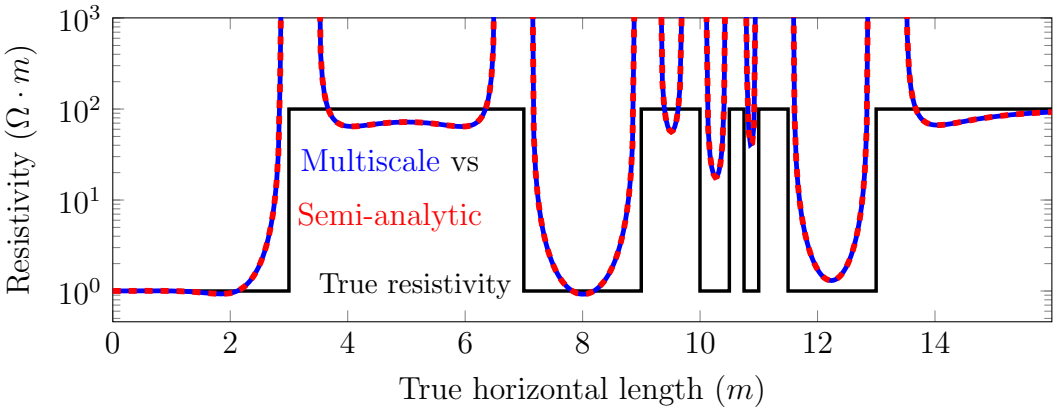

(b) Apparent resistivity based on phase difference

Figure 4.13.: Model problem B. Apparent resistivity for the zz coupling for a 89° deviated well.

4.2.2. Derivatives

4.2.2.1. Model problem C: 2D potential equation

In this subsection, we verify our proposed adjoint-based method to compute derivatives with respect to bed boundary positions, and we analyze their convergence speed with respect to the finite element mesh size. To do so, we first consider a simple scenario in which $\omega = 0$. We further assume a 2D problem in the transverse magnetic polarization, so that H is a scalar and $\mathbf{E}$ is a vector with two components. Then, (2.2) shows that $\nabla \times \mathbf{E} = 0$, so that $\mathbf{E} = \nabla\phi$ for some scalar potential ϕ. Such scalar potential satisfies the continuity equation $\nabla \cdot (\boldsymbol{\sigma} \nabla\phi) = \nabla \cdot \mathbf{J}$, which governs the electrostatic phenomena in a lossy media

(see, e.g., [66]). Furthermore, we can use (3.15) with $\nabla \times H = \boldsymbol{\sigma}\nabla\phi + \mathbf{J}$.

To better analyze the numerical results, we consider a simple problem for which we know the exact solution. Thus, we select $\mathbf{M} = \mathbf{0}$ and $\mathbf{J} = (0, 2\mathbf{x}_2)$, so that $\nabla \cdot \mathbf{J} = 2$. The domain is the unit square $\Omega = (0,1)^2$. Thus, ϕ_{z_i} is solution to

$$-\nabla \cdot (\boldsymbol{\sigma}_{z_i} \nabla \phi_{z_i}) = -2, \tag{4.9}$$

where $\boldsymbol{\sigma}_{z_i} = \sigma_{z_i}\mathbf{I}_2$, with

$$\sigma_{z_i}(\mathbf{x}) = \begin{cases} \sigma_- & \text{if } z < z_i \\ \sigma_+ & \text{if } z > z_i \end{cases} \tag{4.10}$$

is the conductivity of a 1D layered media that consists of two different layers, and $\sigma_\pm$ are two positive values. In this example, we consider $\sigma_- = 1Sm^{-1}$ and $\sigma_+ = 10Sm^{-1}$, and $f = -2$. The boundary conditions are:

$$\phi_{z_i}(x,0) = \frac{\partial \phi_{z_i}}{\partial z}(x,1) = 0, \quad \frac{\partial \phi_{z_i}}{\partial x}(0,z) = \frac{\partial \phi_{z_i}}{\partial x}(1,z) = 0. \tag{4.11}$$

The analytical solution for this problem is:

$$\phi_{z_i}(\mathbf{x}) = \begin{cases} \rho_- z(z-2) & \text{if } z < z_i \\ \rho_+ z(z-2) - [\rho] z_i (z_i - 2) & \text{if } z > z_i. \end{cases} \tag{4.12}$$

For the measurements, we consider $\mathbf{K} = \mathbf{M} = \mathbf{0}$ and $\mathbf{G} = \mathbf{J} = (0, 2\mathbf{x}_2)$ so that the direct and adjoint solutions are the same. Measurements are then given by:

$$\begin{aligned} m(z_i) &= \int_\Omega \nabla \times (\widetilde{\rho}\mathbf{J}) H_{z_i} d\Omega = \int_\Omega \mathbf{J}\widetilde{\rho} \nabla \times (H_{z_i}) d\Omega = \int_\Omega \mathbf{J}\nabla\phi_{z_i} + \int_\Omega |\mathbf{J}|^2 d\Omega \\ &= -\int_\Omega \nabla \cdot \mathbf{J}\phi_{z_i} d\Omega + \int_\Omega |\mathbf{J}|^2 d\Omega = -2\int_\Omega \phi_{z_i} d\Omega + \frac{4}{3} \\ &= -2[\rho]\left(\frac{2}{3}z_i^3 - 2z_i^2 + 2z_i\right) + \frac{4}{3}\rho_+ + \frac{4}{3}. \end{aligned}$$

Thus:

$$\frac{dm}{dz_i}(z_i) = -4[\rho]\left(z_i - 1\right)^2. \tag{4.13}$$

Figure 4.14 compares the derivative of m computed using adjoint state expression (3.15) vs. analytical expression (4.13). As shown there, the numerical result is highly accurate. Figure 4.15 analyses the convergence of the adjoint-based gradient with respect to the finite element mesh size for the case $z_i = 0.5$, and we observe a linear convergence rate.

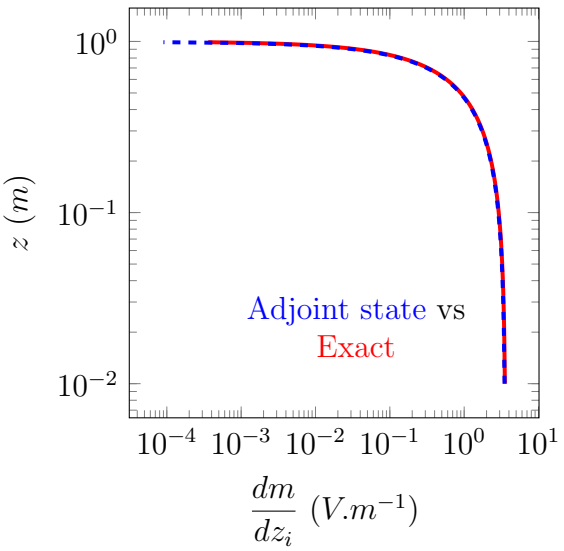

Figure 4.14.: Model problem C. Analytical and numerical gradient.

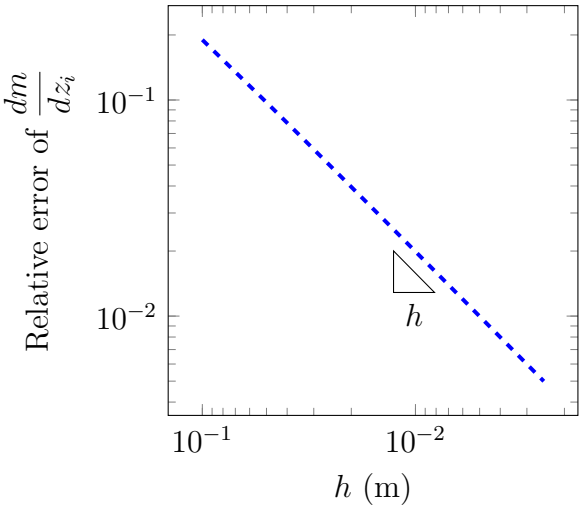

Figure 4.15.: Model problem C. Convergence of the numerical gradient at point $z_i = 0.5$.

4.2.2.2. Model problem D: Two-layered media

Figure 4.16 describes the logging instrument used in this model problem. The conductivity of the two-layer media is given by $\boldsymbol{\sigma}_{z_i} = \sigma_{z_i}\mathbf{I}_3$, where:

$$\sigma_{z_i}(\mathbf{x}) = \begin{cases} 1 & Sm^{-1} \quad \text{if } 0 < z < z_i \\ 10^{-2} & Sm^{-1} \quad \text{if } z_i \leqslant z < 6, \end{cases} \tag{4.14}$$

and $z_i = 3.15\ m$.

In this example, the measurement is the value of the zz coupling of the magnetic field at the receiver. To simplify notation, we denote $H = H_{z_i,z}(Rx)$ to the recorded value, and we have $m(z_i) = H$. Figure 4.17 shows the real and imaginary parts and the absolute value of H for different tool positions. Figure 4.18 compares the derivative with respect to the bed boundary position using the 1.5D adjoint formulation (3.16) vs. that obtained with a finite difference approximation. The finite difference approximation experiences some oscillations due to numerical errors. The solution using the adjoint state method shows superior accuracy and avoids any spurious oscillation. Figures 4.19 and 4.20 display the derivatives of the zz coupling of the magnetic field with respect to resistivity values using the adjoint state method and a finite difference method of the first and second layer, respectively. The aforementioned results verify the accuracy of the adjoint-state method.

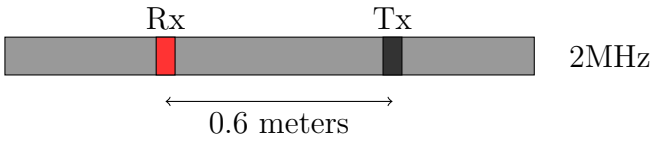

Figure 4.16.: Model problem D. Logging instrument. Tx and Rx denote the transmitter and the receiver, respectively.

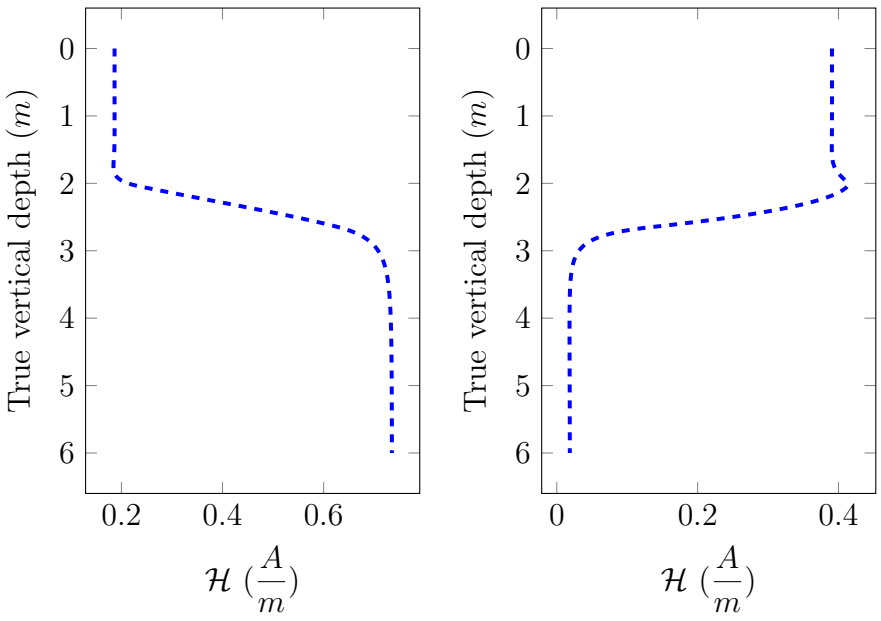

(a) Real part

(b) Imaginary part

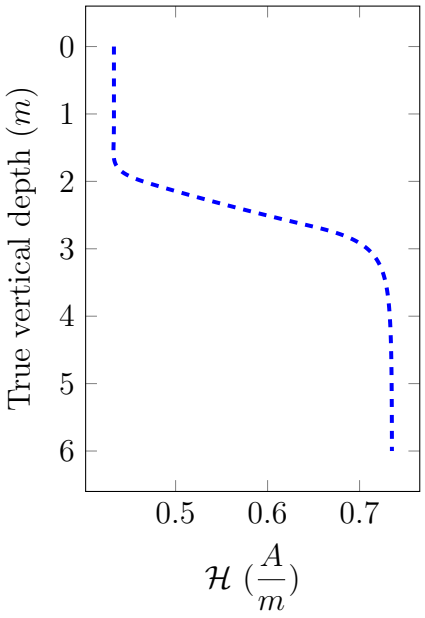

(c) Absolute value

Figure 4.17.: Model problem D. zz coupling of the magnetic field for a vertical well.

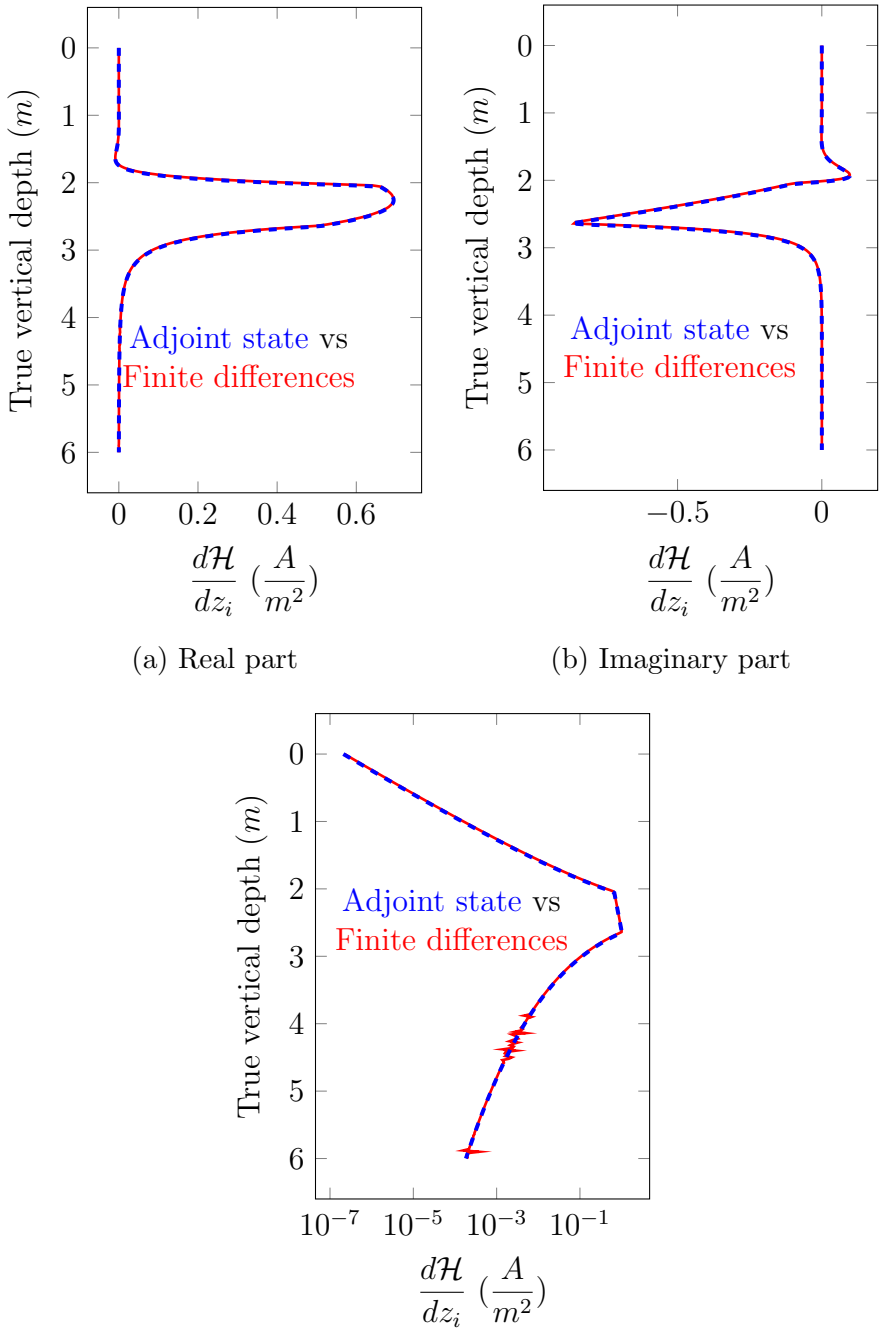

(a) Real part

(b) Imaginary part

(c) Absolute value

Figure 4.18.: Model problem D. Derivative of the zz coupling of the magnetic field with respect to the bed boundary position for a vertical well.

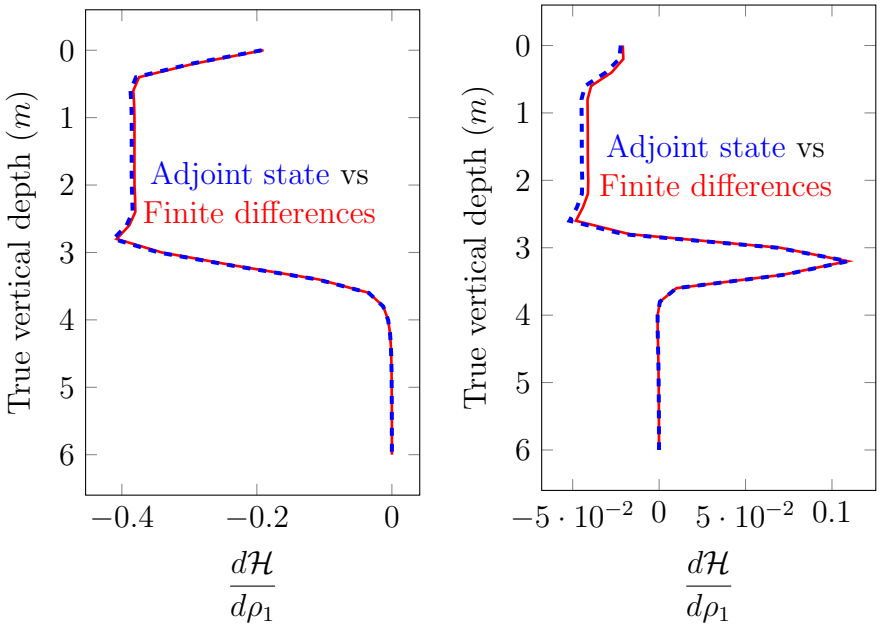

(a) Real part

(b) Imaginary part

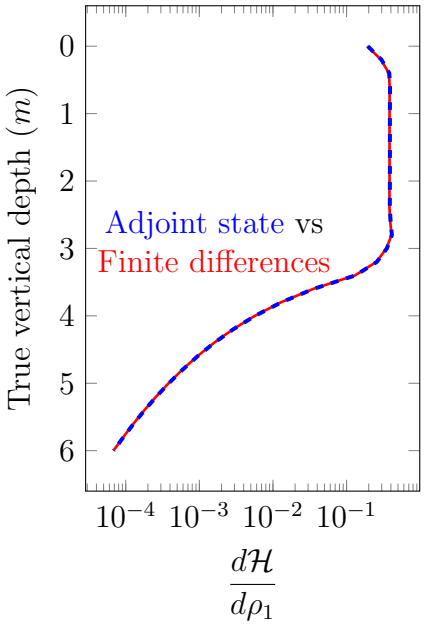

(c) Absolute value

Figure 4.19.: Model problem D. Derivative of the zz coupling of the magnetic field with respect to the resistivity value of the first layer for a vertical well.

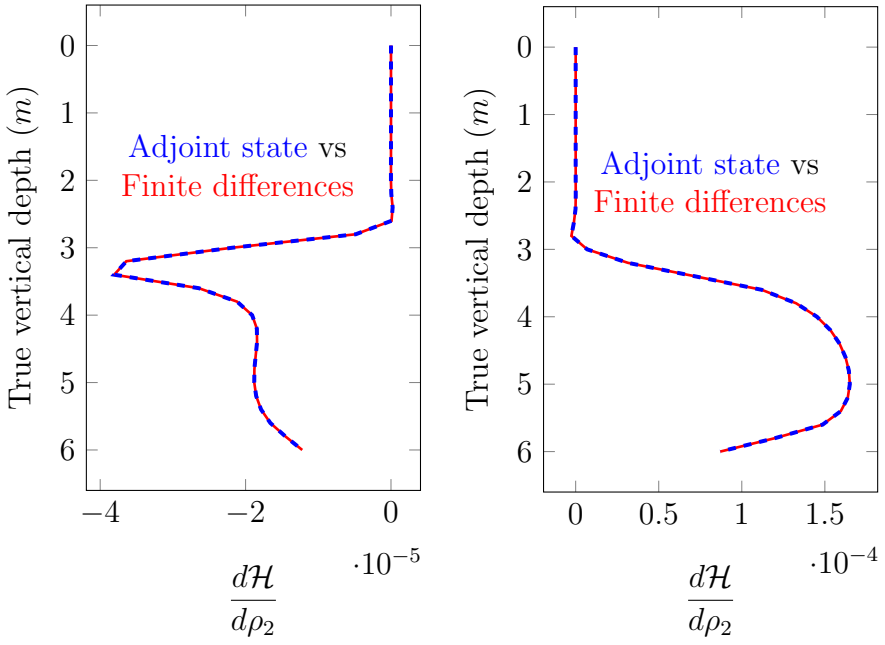

(a) Real part

(b) Imaginary part

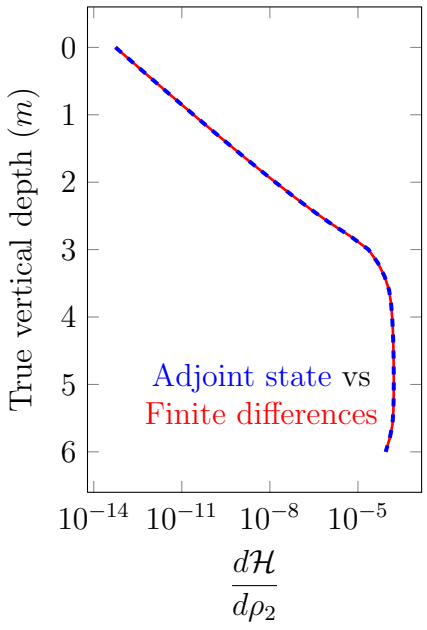

(c) Absolute value

Figure 4.20.: Model problem D. Derivative of the zz coupling of the magnetic field with respect to resistivity value of the second layer for a vertical well.

4.2.2.3. Model problem E: Multi-layered media

Figure 4.21 describes the logging instrument used for this model problem. In this example, the conductivity model features four layers. $\mathbf{z}_i = (z_{i,1}, z_{i,2}, z_{i,3})$ represents the location of the three interfaces. The conductivity of the media is $\boldsymbol{\sigma}_{\mathbf{z}_i} = \sigma_{\mathbf{z}_i}\mathbf{I}_3$, where:

$$\sigma_{\mathbf{z}_i}(\mathbf{x}) = \begin{cases} 1 & Sm^{-1} & \text{if } 0 < z < z_{i,1} \\ 10^{-2} & Sm^{-1} & \text{if } z_{i,1} \leqslant z < z_{i,2}, \\ 1 & Sm^{-1} & \text{if } z_{i,2} \leqslant z < z_{i,3} \\ 10^{-2} & Sm^{-1} & \text{if } z_{i,3} \leqslant z < 10, \end{cases} \tag{4.15}$$

with $\mathbf{z}_i = (3, 5, 7)$.

For this problem, we consider the attenuation and the phase difference of the magnetic field between the two receivers. These are the quantities often recorded in borehole geophysical measurements.

Figure 4.22 describes the attenuation and the phase difference for the zz coupling of the magnetic field. Figures 4.23 and 4.24 show the derivatives of the attenuation and the phase difference with respect to all bed boundary positions of the media using the adjoint state formulation vs. those obtained with a finite difference method. As shown in the figures, the derivatives using the adjoint state method coincide with the finite differences ones for all cases. Indeed, the adjoint-based derivatives produce enhanced accuracy (see Figure 4.25 displaying a zoom of the derivative). Additionally, the adjoint-based method only requires the solution of one finite element problem with two right hand sides, while the finite differences approach involves the solution of one additional problem per interface (i.e., a total of $N_{int} + 1$ problems, where N_{int} is the number of interfaces whose derivative is estimated). Similarly, Figures 4.26 and 4.27 describe the accuracy of the adjoint-state method to compute the derivatives of the attenuations and phase differences with respect to the resistivity values of all layers.

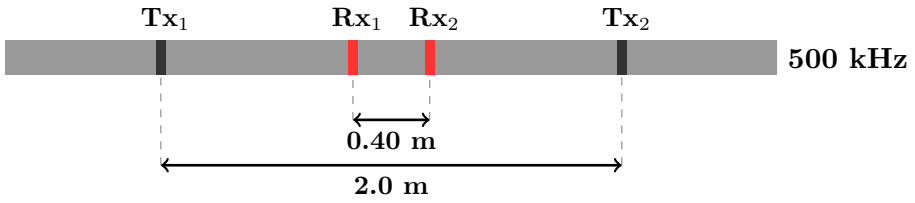

Figure 4.21.: Model problem E. Logging instrument. Rx_1 and Rx_2 are the first and the second receivers, respectively. Tx_1 and Tx_2 are the first and the second transmitters, respectively.

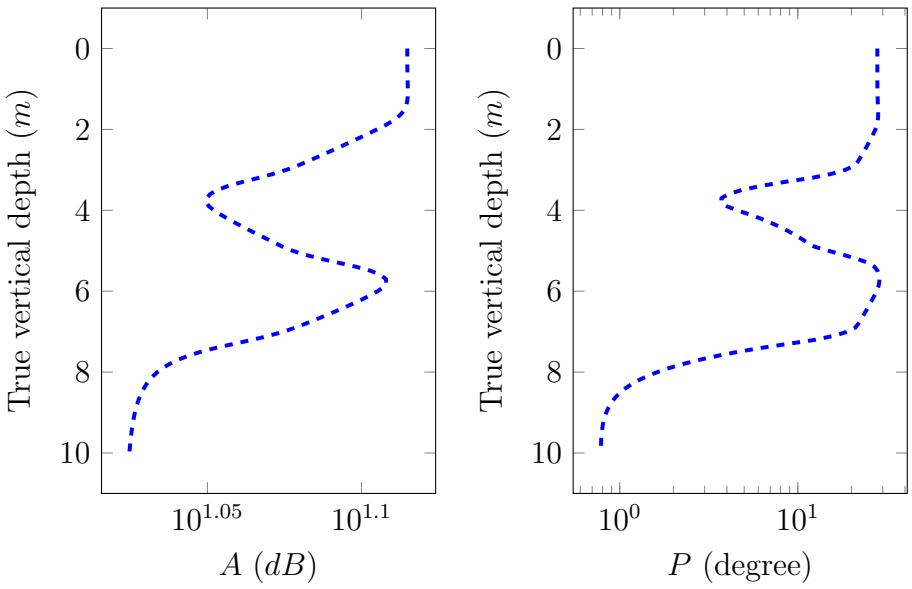

(a) Attenuation (b) Phase difference

Figure 4.22.: Model problem E. Attenuation and phase difference for the zz coupling of the magnetic field.

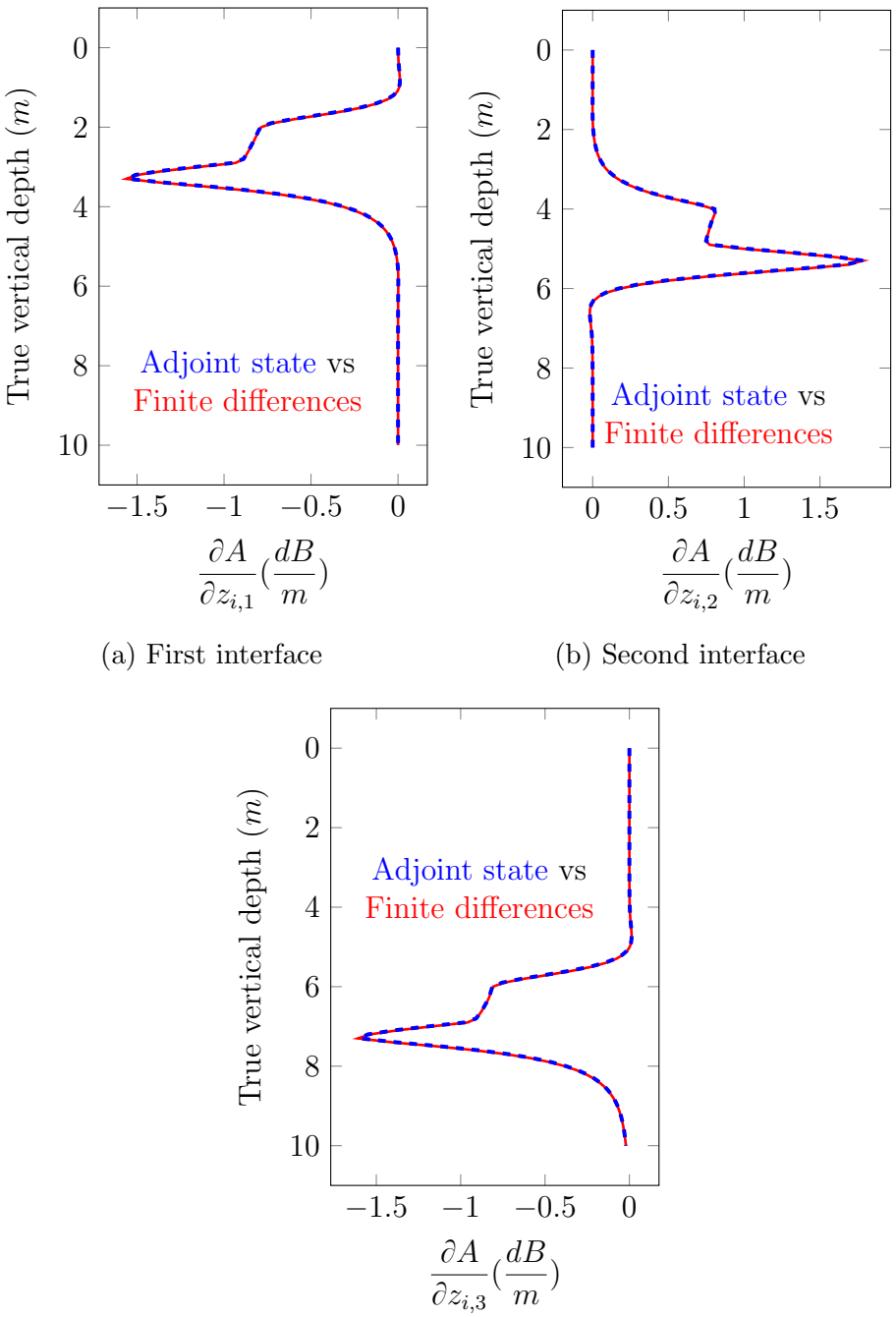

(a) First interface

(b) Second interface

(c) Third interface

Figure 4.23.: Model problem E. Derivatives of the attenuation with respect to the bed boundary positions.

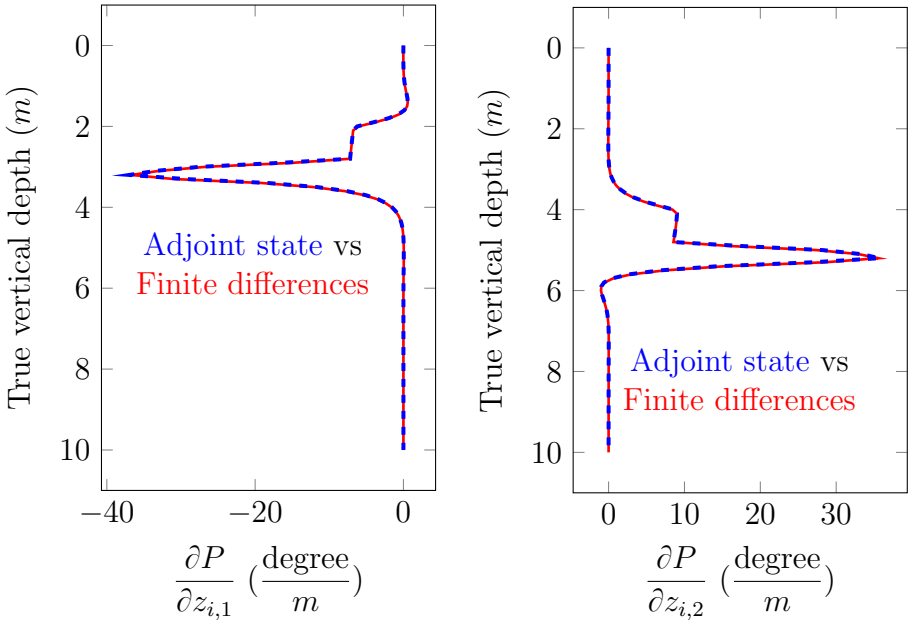

(a) First interface

(b) Second interface

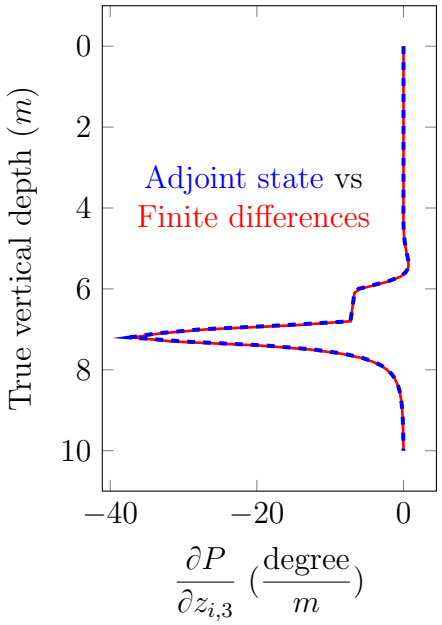

(c) Third interface

Figure 4.24.: Model problem E. Derivatives of the phase difference with respect to the bed boundary positions.

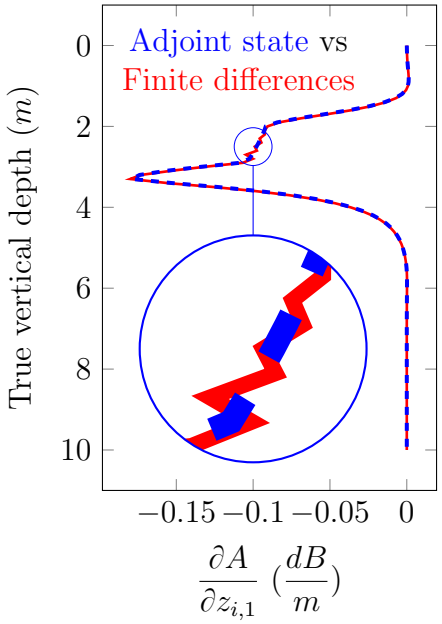

Figure 4.25.: Model problem E. Derivative of the attenuation with respect to the first bed boundary position.

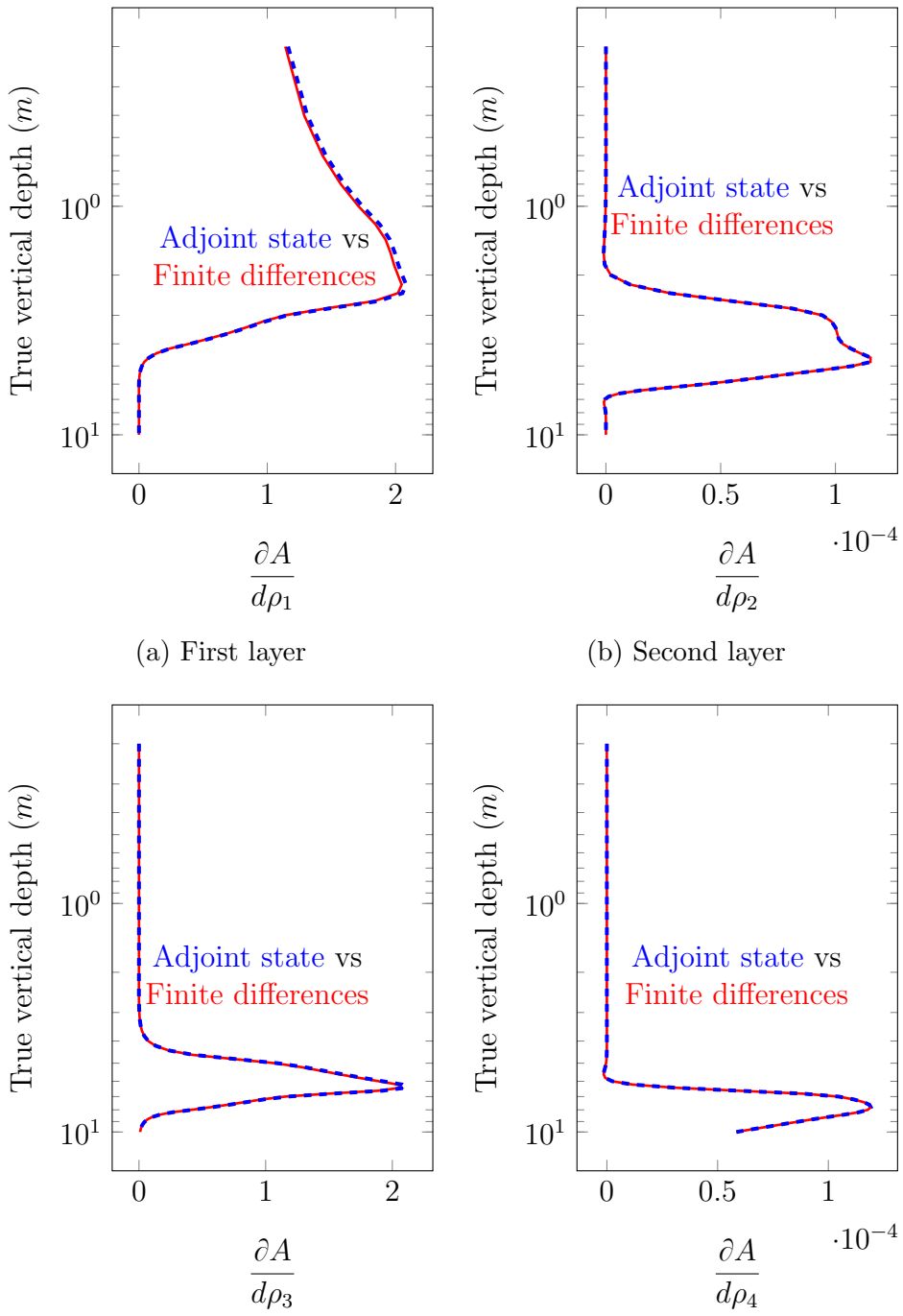

(a) First layer

(b) Second layer

(c) Third layer

(d) Fourth layer

Figure 4.26.: Model problem E. Derivative of the attenuations with respect to the resistivity value of all layers in a vertical well.

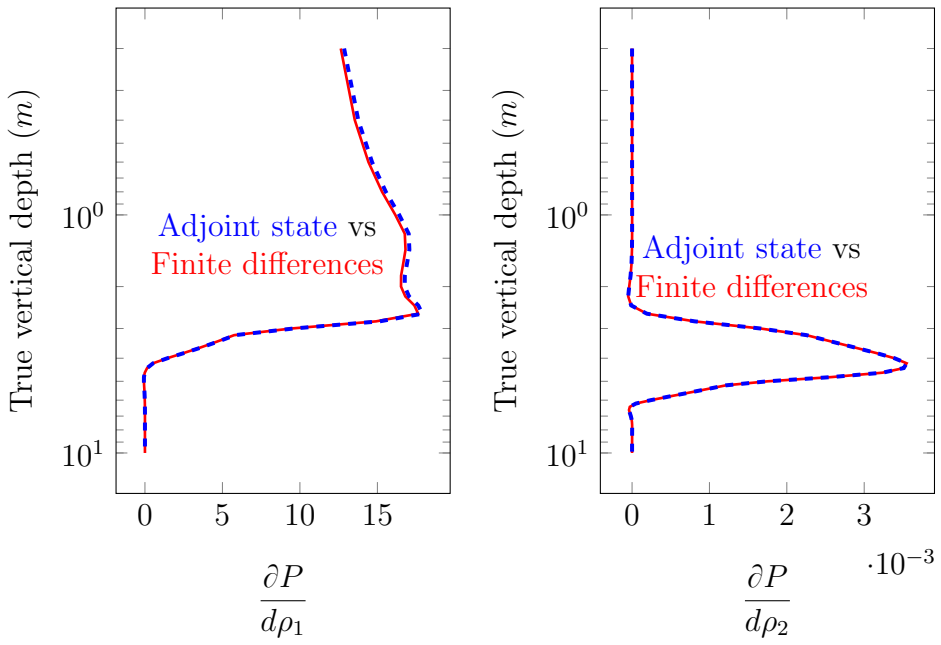

(a) First layer

(b) Second layer

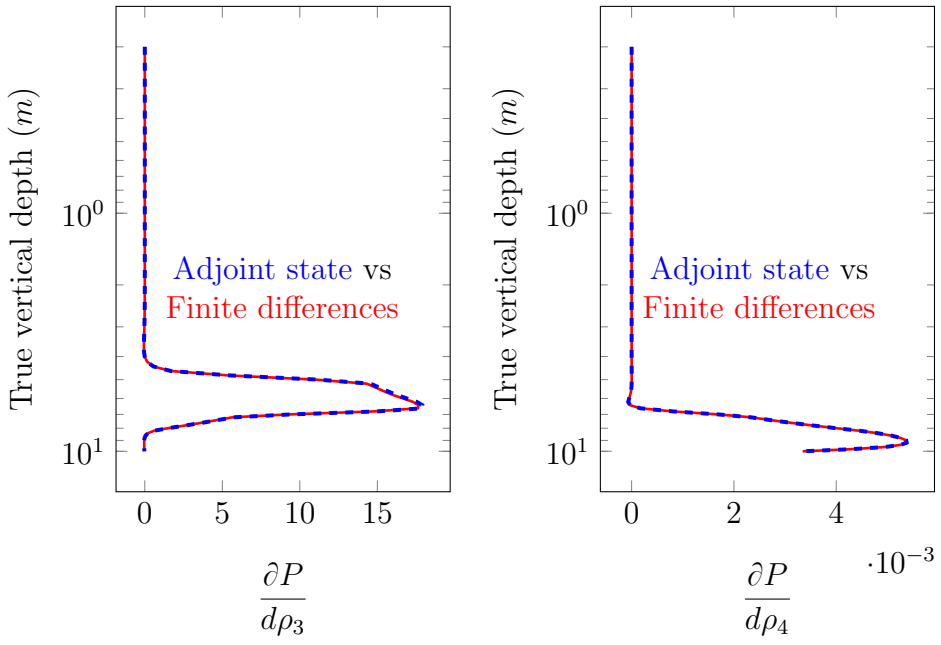

(c) Third layer

(d) Fourth layer

Figure 4.27.: Model problem E. Derivative of the phase differences with respect to the resistivity value of all layers in a vertical well.

4.2.3. Arbitrary resistivity profile

We consider the logging instrument described in Figure 4.2 and a model problem that exhibits a subdomain with a linearly varying resistivity, which is the case of an Oil-Water Transition (OWT) zone corresponding to a two phase-flow of immiscible fluids. We compare our numerical solution to the semi-analytic one. In the later case, we approximate our linearly varying resistivity distribution using multiple piecewise constant resistivity distributions. Figure 4.28 compares the attenuation and phase difference of the semi-analytic solution and the multiscale one for the zz coupling. Figure 4.29 shows that the apparent resistivity of the semi-analytic solution is converging to the multiscale solution as the number of layers with piecewise constant resistivity distribution increases. With our numerical method, we can model those arbitrarily varying conductivities without the need of approximating them. Figures 4.30 and 4.31 compare the derivatives of the attenuation and phase differences with respect to the resistivity values of all layers using the adjoint-state method and a finite difference method. The aforementioned results verify the accuracy of our formulation for computing the derivatives with respect to the resistivity values for a media with an arbitrary resistivity distribution.

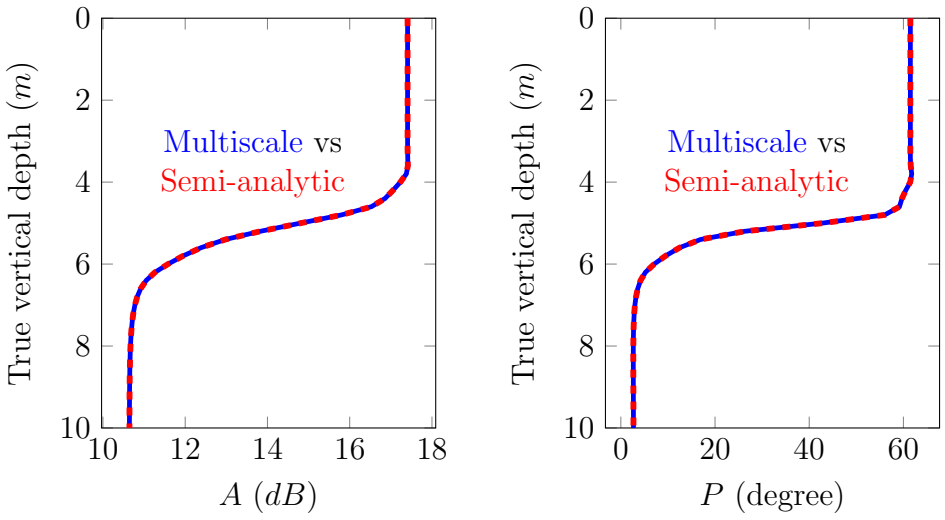

(a) Attenuation (b) Phase difference

Figure 4.28.: Arbitrary resistivity profile. Attenuation and phase difference of zz coupling of the magnetic field in a vertical well (dip angle = 0°).

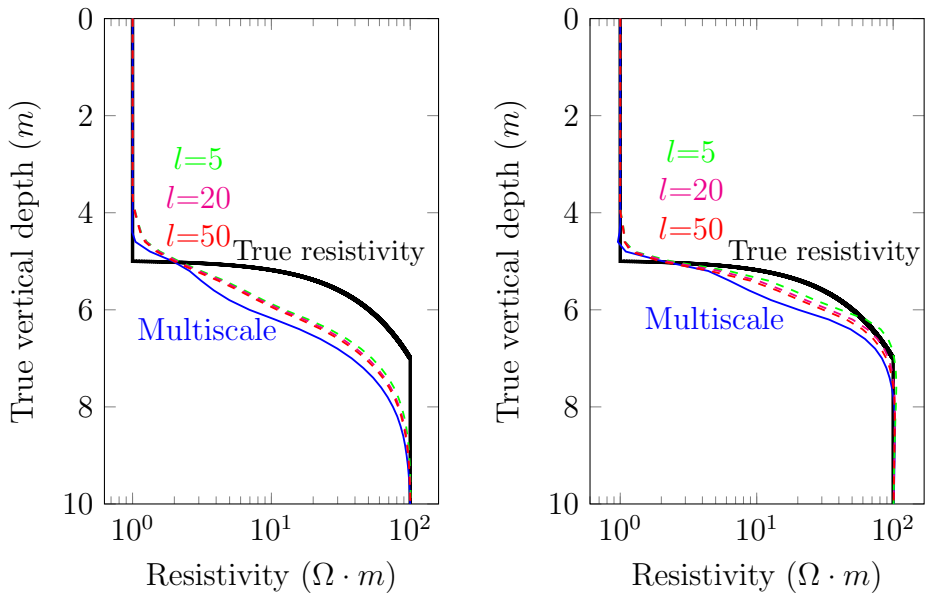

(a) Apparent resistivity based on attenuation

(b) Apparent resistivity based on phase difference

Figure 4.29.: Arbitrary resistivity profile. Convergence of the zz coupling apparent resistivity of the semi-analytic solution to the multiscale one in a vertical well (dip angle $= 0^\circ$). l is the number of piecewise constant resistivity distributions that we select to approximate the linearly varying resistivity.

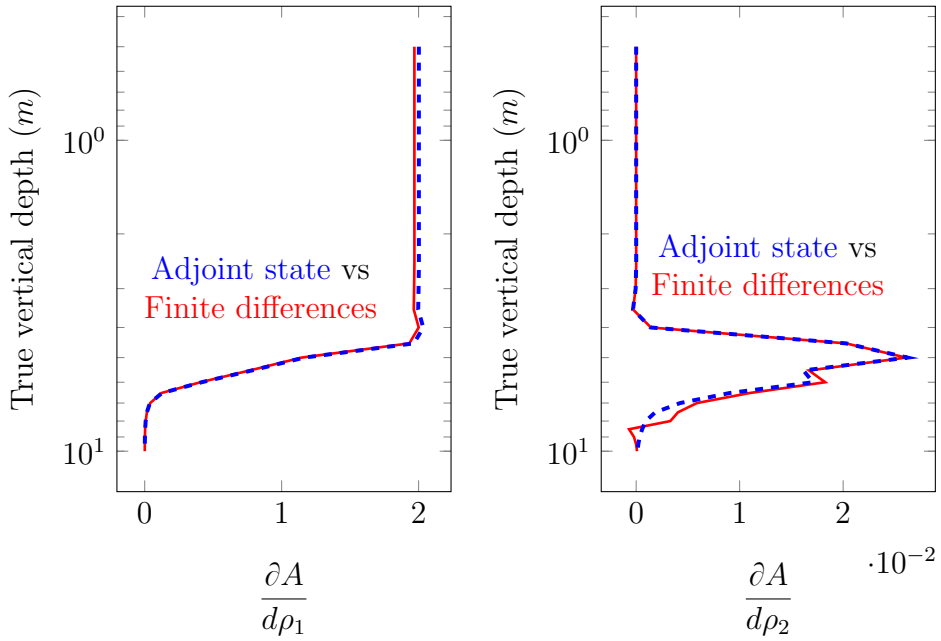

(a) First layer

(b) Second layer

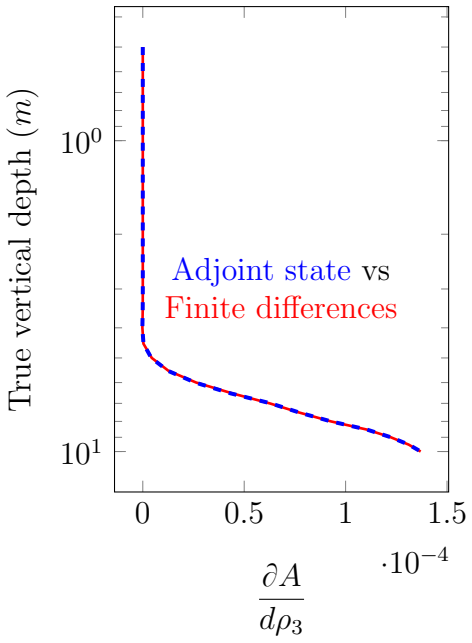

(c) Third layer

Figure 4.30.: Arbitrary resistivity profile. Derivative of the attenuations with respect to the resistivity value of each layer.

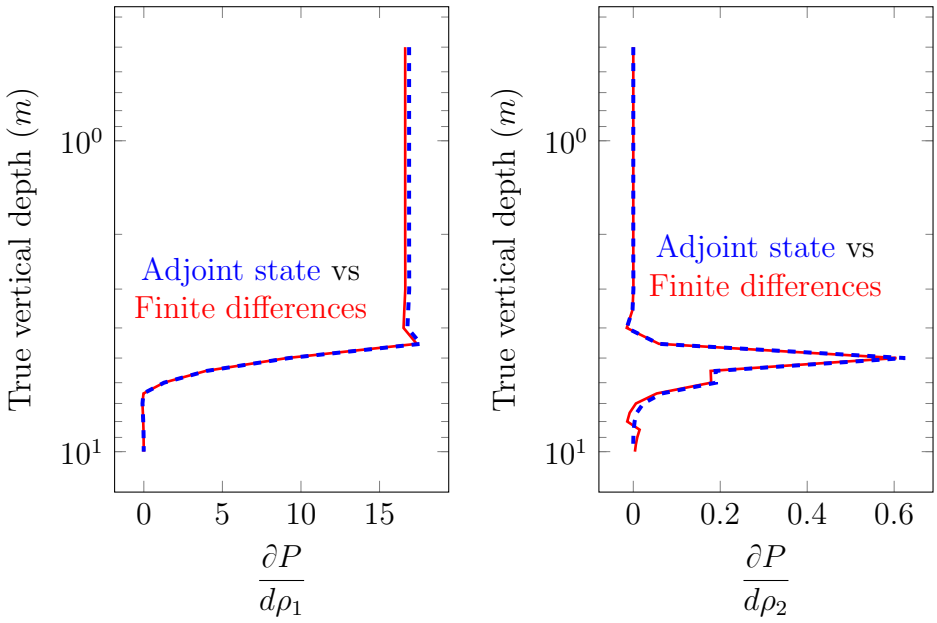

(a) First layer

(b) Second layer

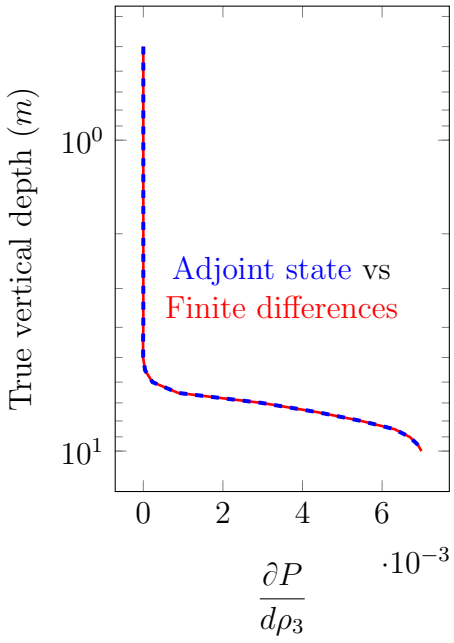

(c) Third layer

Figure 4.31.: Arbitrary resistivity profile. Derivative of the phase differences with respect to the resistivity value of each layer.

5. Applications

In this Chapter, we describe some geosteering applications of the 1.5D method. In addition to the traditional Logging-While-Drilling (LWD) instruments, we consider the newly introduced deep and extra-deep azimuthal logging devices [10, 13]. In addition, to map the subsurface, they help us to select the well trajectory properly in the hydrocarbon reservoir in order to increase the productivity of the well [16, 10, 20, 21]. There exist several differences between conventional LWD devices and deep azimuthal devices, e.g., the number of transmitters and receivers, and the spacings between them, which are significantly larger in deep azimuthal configurations. Figure 5.1 displays a typical deep azimuthal device incorporating tilted coils and operating at several frequencies. The main advantage of deep and extra-deep resistivity instruments in comparison to conventional LWD devices is their significantly longer depth of investigation, which enables to perform geosteering without crossing a water-saturated rock [13, 10].

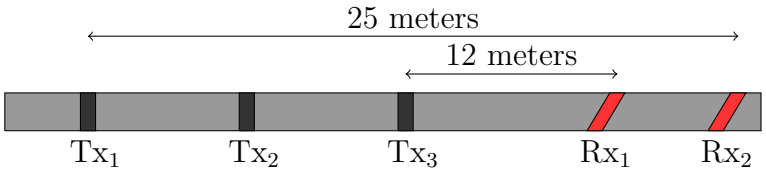

Figure 5.1.: A LWD deep azimuthal tool. Tx_1, Tx_2, Tx_3 are the transmitters, and Rx_1 and Rx_2 are two tilted receivers.

Herein, we investigate the affect of considering Oil-Water Contact (OWC) and Oil-Water Transition (OWT) zones in our simulations via two synthetic examples in which the saturation profiles are obtained from the experiment described in [12], and the corresponding resistivity profiles are estimated using Archie's (experimental) law [30]. Moreover, We describe a novel inversion method based on deep learning to be used for the inversion of the resistivity measurements.

5.1. Analyzing OWT zones

We consider a tank in which we pour oil and water. Since oil and water are immiscible fluids, the contact between these two fluids appears as a sharp interface which is called OWC (see Figure 5.3a). In the aforementioned scenario, the light material (oil) locates on top due to the gravity effect. However, if we insert a capillary tube into the tank containing oil and water, the OWC inside the tube appears in a different level compared to the OWC outside the tube (see Figure 5.2). The aforementioned phenomena is called capillary effect. By increasing the radius of the tube, the height of the OWC decreases inside the tube [59]. In a porous media, the pores act in a similar fashion as the capillary tube[50].

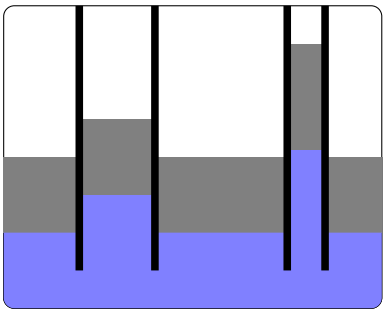

Figure 5.2.: Capillary effect for a tank containing two immiscible fluids in the presence of two capillary tubes.

In general, a porous media is first filled with water, and later the oil replaces the water in the pores. Due to the high capillary pressure in the small pores, the oil usually enters to the bigger ones. The OWT zone is the area of the formation that separates the oil-saturated reservoir from the water-saturated rock (see Figure 5.3b). OWT zones where the water saturation (S_w) is below one appear because of capillary effect and a loss of buoyancy pressure in the hydrocarbon phase [84, 27].

We can categorize OWT zones into two different kinds, namely: (a) homogeneous, which are described by a single capillary pressure while the water saturation increases uniformly, and (b) heterogeneous, in which the capillary pressure and water saturation vary level by level. In this work, we consider homogeneous OWT zones.

The length of an OWT zone can differ from a few meters to more than hundred meters [57]. The thin OWT zones appear mostly in a homogeneous reservoir. The thick OWT zones may appear in many fields. They appear

due to multiple reasons, e.g., reservoir heterogeneity, complex pore networks. Hence, the OWT zone can be a considerable part of an oil reservoir [2, 18, 69]. However, exploiting the OWT zone is considered not economical. Still, accurately simulating an OWT zone may increase the productivity of the reservoir, and helps us to avoid invading the water-saturated rock.

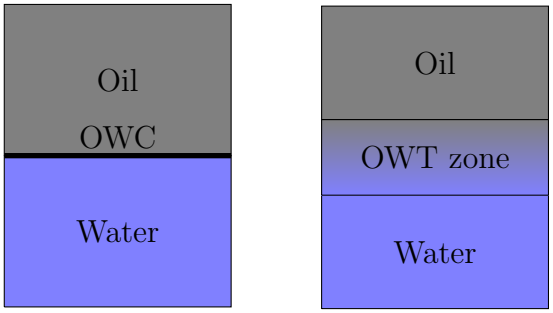

(a) OWC surface (b) OWT zone

Figure 5.3.: Oil-water contact surface and transition zone.

5.1.1. Resistivity profiles and synthetic subsurface models and logging trajectories

We calculate the resistivity profile of the transition zone from the water saturation profile. Determining the water saturation profile in the transition zone in a porous media to predict the recoverable oil saturated in the rock is a demanding task in petrophysics (see, e.g., [49, 29, 55]). However, sometimes, a saturation profile may be available from previously recorded data. For example, in [12], the authors utilized electrical wireline logs and capillary pressure relations to obtain the water saturation in the Wellington West field. In here, we use the data provided by [12] to produce two realistic examples of OWT zones (see Table 5.1). In order to compute the resistivity of a fluid saturated rock, we employ Archie's law, given by:

$$\rho_o = a\phi^{-m} S_w^{-n} \rho_w, \tag{5.1}$$

where ρ_o is the resistivity of the oil-saturated rock, ρ_w is the brine resistivity (in our case, we select $\rho_w = 0.13\ \Omega \cdot m$), a is the tortuosity factor, ϕ denotes the porosity, and m and n are the cementation and saturation exponents of the rock, respectively. In this work, we consider $m = n = 2$ and $a = 1$.

S_w (fraction)	Model 1 (meters)	Model 2 (meters)
0.05	0.0	—
0.1	14.02	—
0.15	18.59	—
0.18	—	0
0.2	21.33	4.57
0.25	23.16	9.14
0.3	24.38	12.19
0.35	24.84	14.63
0.4	25.29	16.15
0.45	25.75	17.83
0.5	26.21	19.05
0.55	26.67	20.26
0.6	27.12	21.33
0.65	27.27	21.94
0.7	27.43	22.55
0.75	27.55	23.16
0.8	27.67	23.46
0.85	27.79	23.77
0.9	27.91	23.92
0.95	28.04	24.07
1	28.16	24.23

Table 5.1.: Water saturation in two transition zones.

Moreover, we assume a homogeneous rock porosity equal to 20% and 25% for our first and second models, respectively. Using (5.1) and the resistivity values of Table 5.1, we obtain a set of resistivity values which are extended to the entire transition zone by using a cubic piecewise spline interpolation composed of three subintervals (see Figure 5.4).

In this work, we approximate our formation as a sequence of three 1D models, which are described in Figures 5.5 and 5.6. Synthetic example 1 (Figure 5.5) considers the OWT zone described in Model 1 (Figure 5.4a), while synthetic example 2 (Figure 5.6) employs the OWT zone described in Model 2 (Figure 5.4b).

5.1.2. Logging device and measurements

We consider an extra-deep LWD instrument with short and long spacings, as described in Figure 5.7. The logging instrument operates at two frequencies,

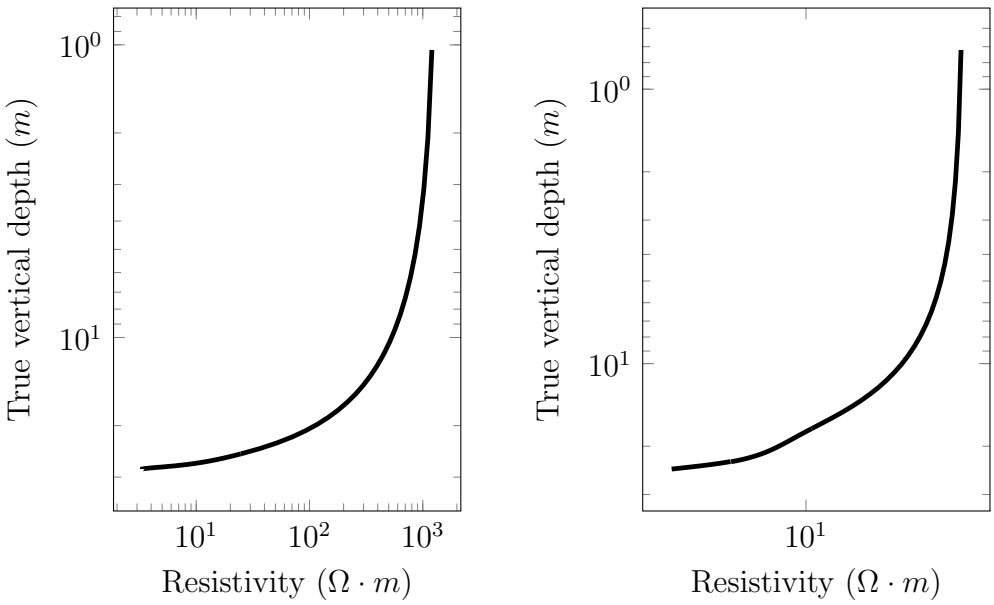

(a) Model 1 ($\rho_{sp,1}$) (b) Model 2 ($\rho_{sp,2}$)

Figure 5.4.: Resistivity profile for two OWT zones.

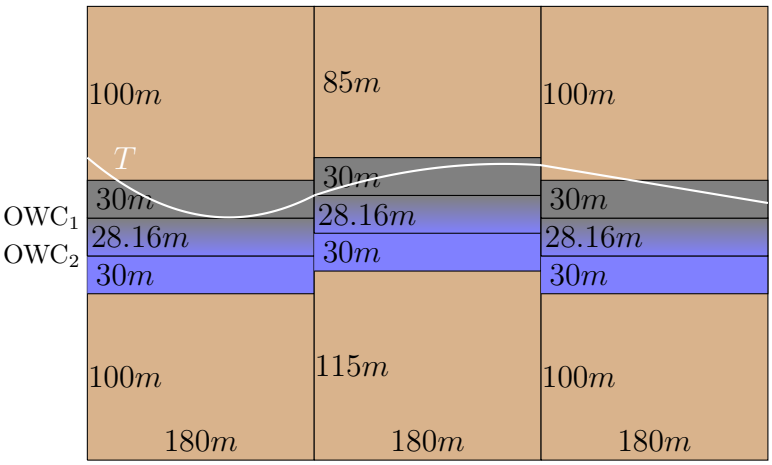

Figure 5.5.: Example 1. T describes the logging trajectory.

Example			OWT zone	
Example 1 $(\Omega \cdot m)$	10.00	1300	$\rho_{sp,1}$	3.25
Example 2 $(\Omega \cdot m)$	10.00	64.19	$\rho_{sp,2}$	2.08

Table 5.2.: Resistivity of different layers for our two synthetic examples.

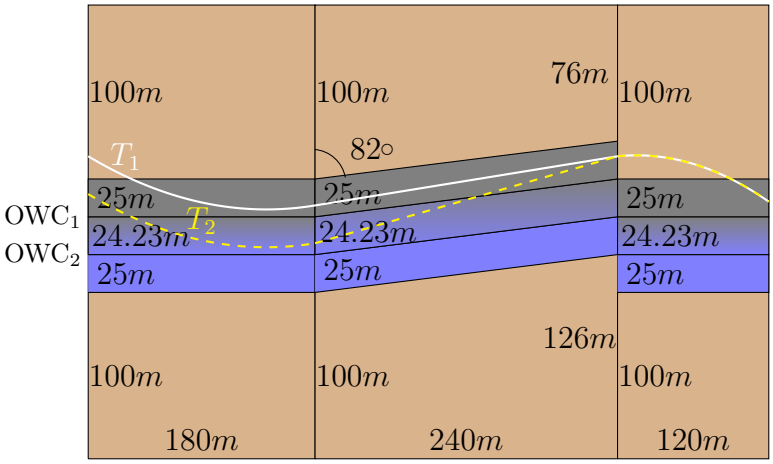

Figure 5.6.: Example 2. T_1 and T_2 describe two logging trajectories.

namely, 10 kHz (short spacing) and 2 kHz (long spacing).

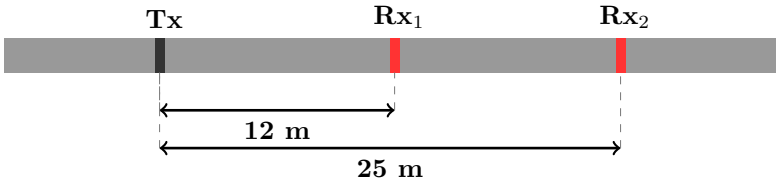

Figure 5.7.: Logging instrument. Tx is the induction transmitter, and Rx_1 and Rx_2 are the receivers. The instrument operates at two frequencies: 2 kHz for the long spacing, and 10 kHz for the short one.

We denote the nine couplings of the magnetic field as follows:

$$\boldsymbol{\mathcal{H}} = \begin{bmatrix} H_{xx} & H_{xy} & H_{xz} \\ H_{yx} & H_{yy} & H_{yz} \\ H_{zx} & H_{zy} & H_{zz} \end{bmatrix}, \tag{5.2}$$

where the first and the second subscripts refer to the direction of the transmitter and the receiver magnetic dipole, respectively.

In LWD resistivity measurements, it is common to consider attenuations and phase differences of the zz coupling [31, 26]. In our case, we consider an extra-deep azimuthal instrument equipped with one receiver. We define our

measurement of interest as:

$$\ln(H_{zz}) = \underbrace{\ln(\mid H_{zz} \mid)}_{\times 20\log(e)=A(dB)} + i \underbrace{ph(H_{zz})}_{\times \frac{180}{\pi}=P(\text{degree})}. \tag{5.3}$$

Additionally, we consider directional measurements based on the apparent conductivity [88]. Following (5.2), we compute apparent conductivity $\boldsymbol{\sigma}_p$ as:

$$\boldsymbol{\sigma}'_p = \begin{bmatrix} \sigma_{p,xx} & \sigma_{p,xy} & \sigma_{p,xz} \\ \sigma_{p,yx} & \sigma_{p,yy} & \sigma_{p,yz} \\ \sigma_{p,zx} & \sigma_{p,zy} & \sigma_{p,zz} \end{bmatrix}' = \mathbf{K} \cdot \boldsymbol{\mathcal{H}}', \tag{5.4}$$

where the prime symbol denotes the adjoint of the matrix, and we have:

$$\mathbf{K} = \begin{bmatrix} i\frac{8\pi}{\omega\mu_0} & i\frac{8\pi}{\omega\mu_0} & i\frac{16\pi}{\omega\mu_0} \\ i\frac{8\pi}{\omega\mu_0} & i\frac{8\pi}{\omega\mu_0} & i\frac{16\pi}{\omega\mu_0} \\ i\frac{16\pi}{\omega\mu_0} & i\frac{16\pi}{\omega\mu_0} & i\frac{4\pi}{\omega\mu_0} \end{bmatrix}. \tag{5.5}$$

Using apparent conductivity (5.4), we define the symmetrized directional measurement as:

$$\sigma_d = \frac{\sigma_{p,xz} - \sigma_{p,zx}}{2}. \tag{5.6}$$

The aforementioned directional measurement has high sensitivity to the bed boundaries [63, 20, 88]. Another directional measurement which is highly sensitive to bed boundaries is the geosignal [73], which is defined as:

$$g = \ln\left(\frac{H_{zz}+H_{zx}}{H_{zz}-H_{zx}}\right) = \underbrace{\ln\left(\frac{\mid H_{zz}+H_{zx} \mid}{\mid H_{zz}-H_{zx} \mid}\right)}_{\times 20\log(e)=A(dB)} + i \underbrace{\left(ph(H_{zz}+H_{zx}) - ph(H_{zz}-H_{zx})\right)}_{\times \frac{180}{\pi}=P(\text{degree})}. \tag{5.7}$$

To illustrate that OWC models can lead to unrealistic simulations, we compare the simulated results corresponding to two OWC models (OWC_1 and OWC_2, see Figures 5.5 and 5.6) with the true OWT zone model.

5.1.3. Numerical results

Figure 5.8 shows the attenuation of the zz coupling of the magnetic field for the first example using extra-deep short and long spacings. This figure shows significant differences between the OWT zone and OWC_1 model results. The OWC_1 model leads to a large error in our simulated measurements, which will severely affect the inversion process. However, the aforementioned figures show a small difference between the OWT zone and OWC_2 model solutions.

Figures 5.9 and 5.10 illustrate the apparent conductivity and geosignal, respectively, using extra-deep short and long spacings for the first example. As observed in the figures, the aforementioned directional measurements are highly sensitive to the position of a bed boundary. Each peak indicates the position of a bed boundary. The peak direction identifies the tool motion from a more resistive layer to a less resistive one (convex) or vice versa (concave). This information can be used for geosteering purposes to navigate the instrument inside the reservoir. Similarly as with zz coupling, there is a large difference between the OWT zone and OWC_1 model solutions, which can lead to a considerable inversion error. Again, OWC_2 model solution seems to provide similar logs to those obtained on the OWT zone scenario. However, these results may lead us to enter into a rock with significant water saturation, thus, lowering the well productivity. In summary, considering OWC_2 instead of OWT zone puts us in the danger of entering a partially water saturated rock.

For the second example shown in Figure 5.6, we consider two different trajectories. The first trajectory T_1 is entirely above the OWT zone. The results for T_1 verify, once again, the conclusions we obtained for the first example (see Figure 5.11). Moreover, to investigate the difference between OWT zone and OWC_2 models, we consider a second trajectory T_2 which enters the OWT zone (see Figure 5.6). Figure 5.12 shows the attenuations and phase differences of the zz coupling using the short spacing. This figures shows that a noticeable difference exists between the OWT and OWC_2 models in the part of the trajectory that is inside the OWT zone. These differences may lead to important errors in our inverted values. Figures 5.13 and 5.14 show the directional measurements using short and long spacings. They describe a considerable difference on the response between the OWT zone and OWC_2 model solutions when the trajectory enters the OWT zone. Again, this difference may lead to a significant inversion error. Moreover, by considering OWC_2, we are unable of accurately estimate the exact bed boundary positions. The aforementioned feebleness puts us in danger of entering the water saturated rock and creating attics in the reservoir. Consequently, the production of the reservoir may decrease if OWC models are considered.

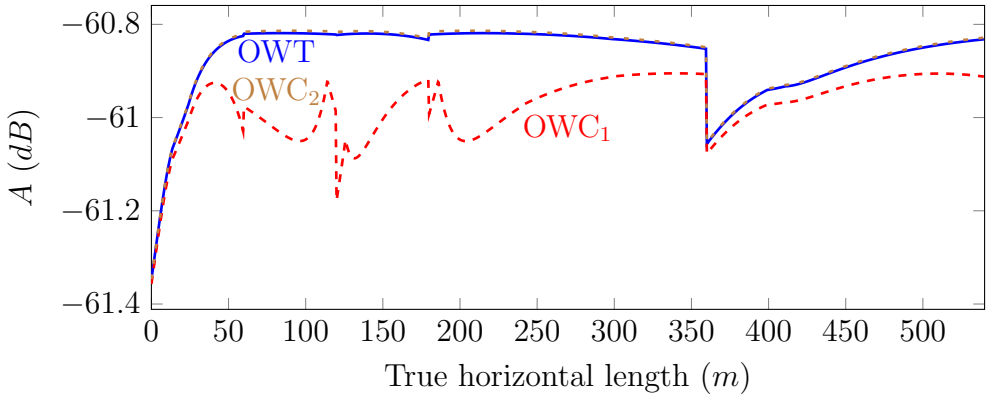

(a) Short spacing

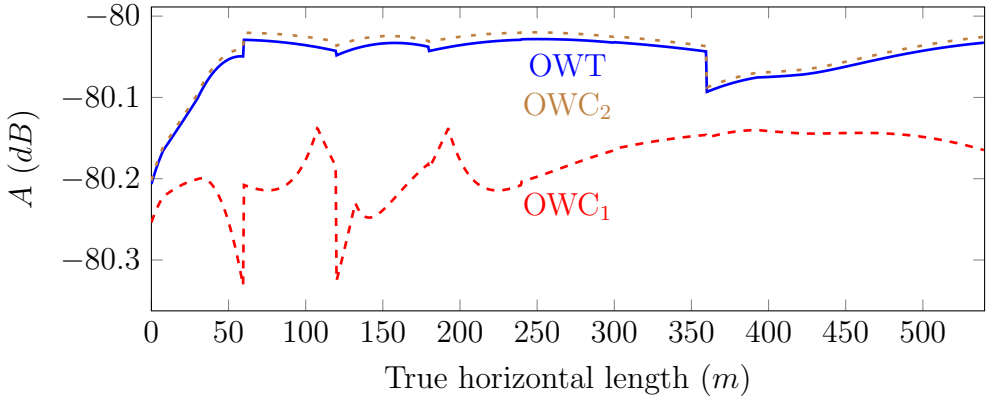

(b) Long spacing

Figure 5.8.: Example 1. Attenuation of zz coupling using short and long spacings.

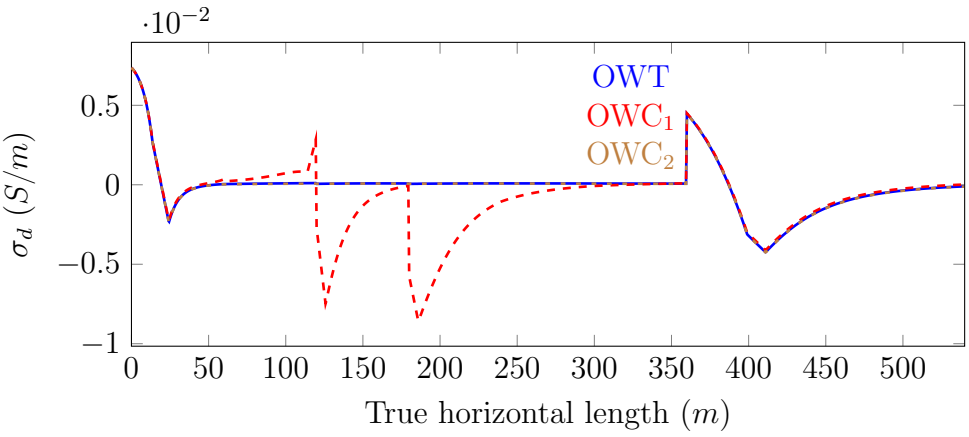

(a) Short spacing

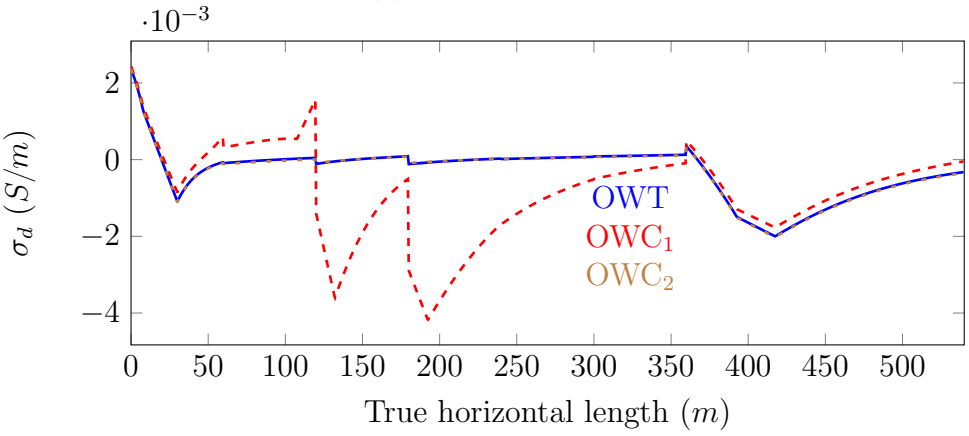

(b) Long spacing

Figure 5.9.: Example 1. Real part of the symmetrized apparent conductivity using short and long spacings.

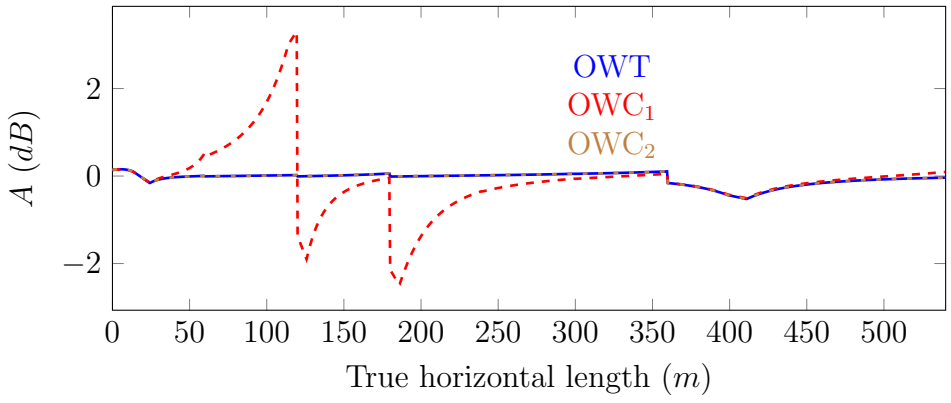

(a) Short spacing

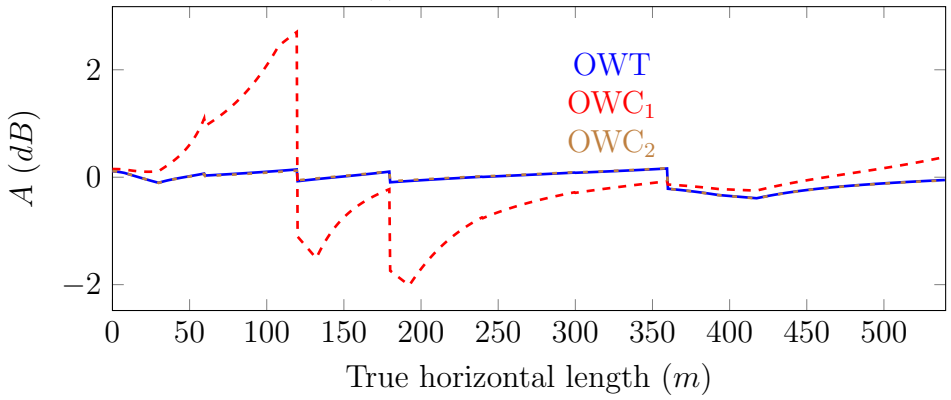

(b) Long spacing

Figure 5.10.: Example 1. Attenuation of geosignal using short and long spacings.

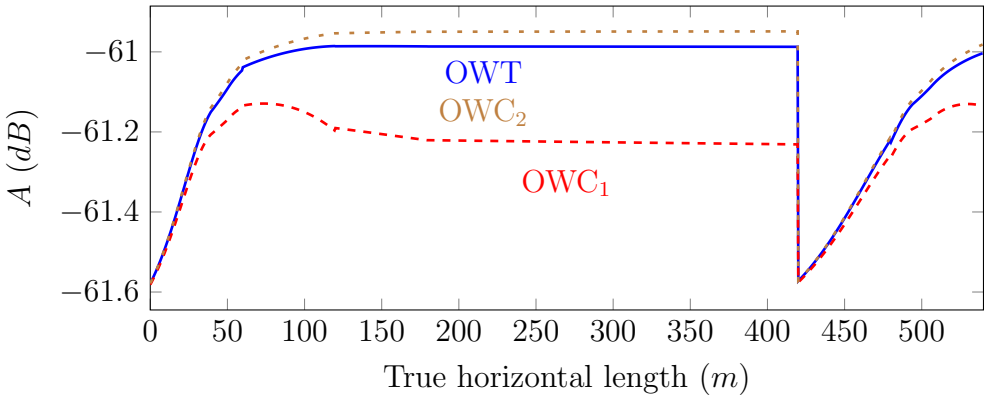

(a) Short spacing

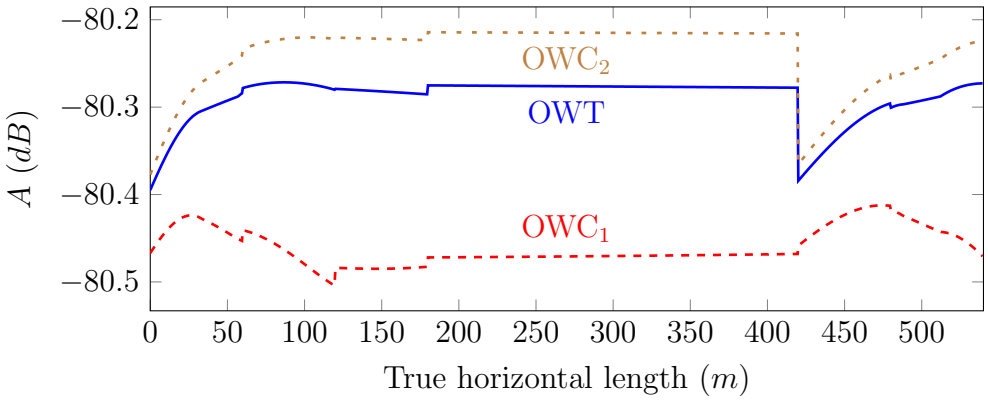

(b) Long spacing

Figure 5.11.: Example 2. Attenuation of zz coupling using short and long spacings for trajectory T_1.

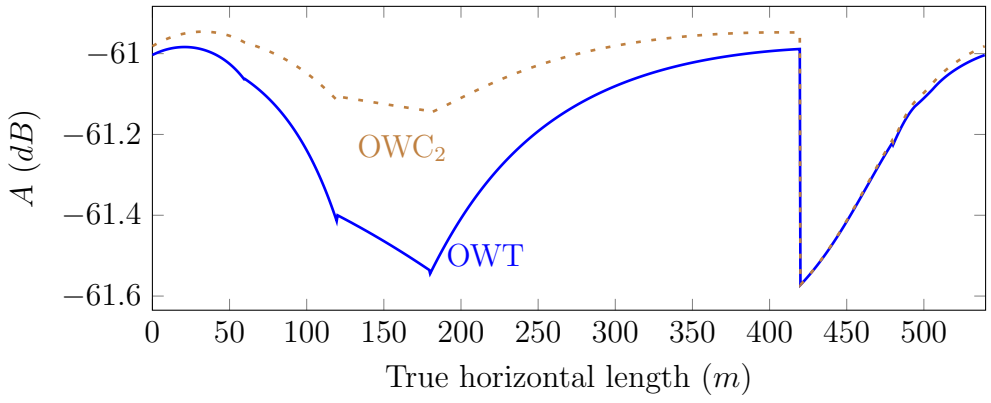

(a) Attenuation

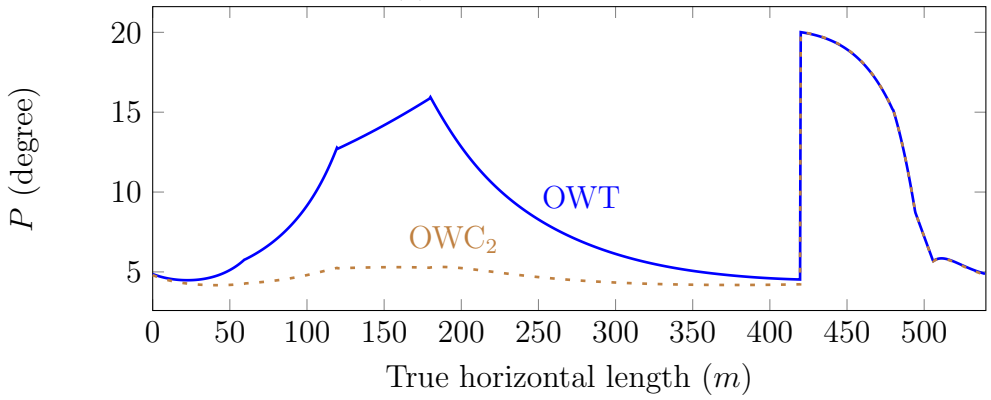

(b) Phase difference

Figure 5.12.: Example 2. Attenuation and phase difference for zz coupling using short spacing for trajectory T_2.

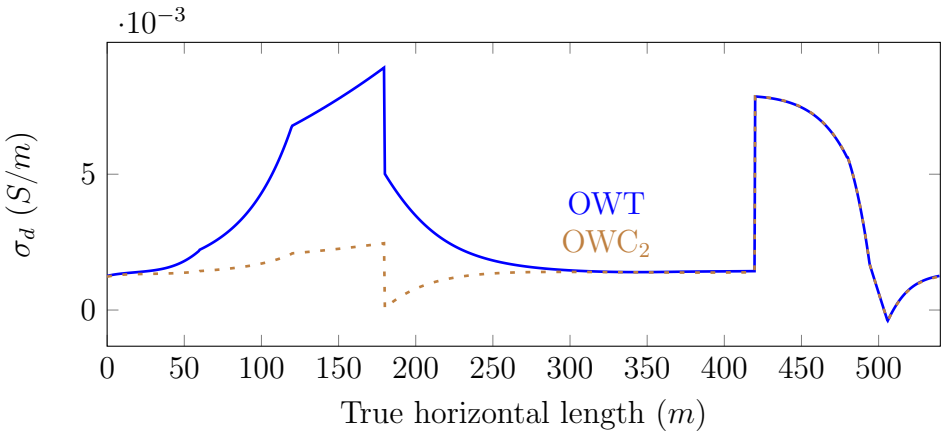

(a) Short spacing

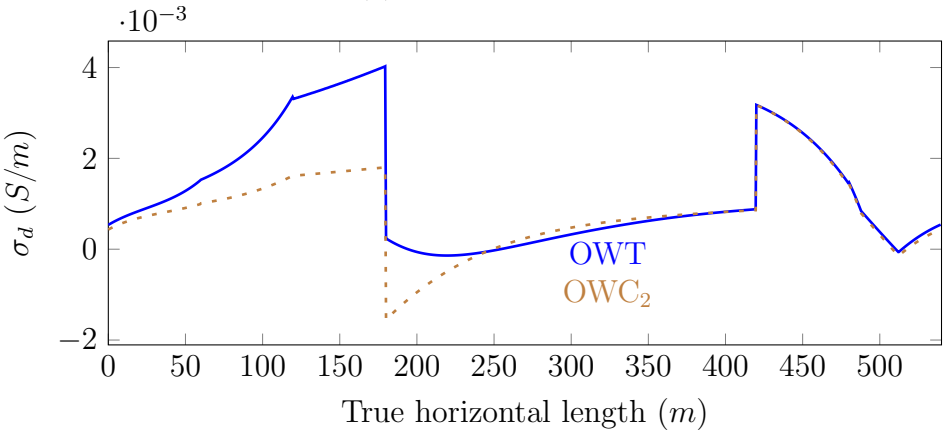

(b) Long spacing

Figure 5.13.: Example 2. Real part of symmetrized apparent conductivity using short and long spacings spacing for trajectory T_2.

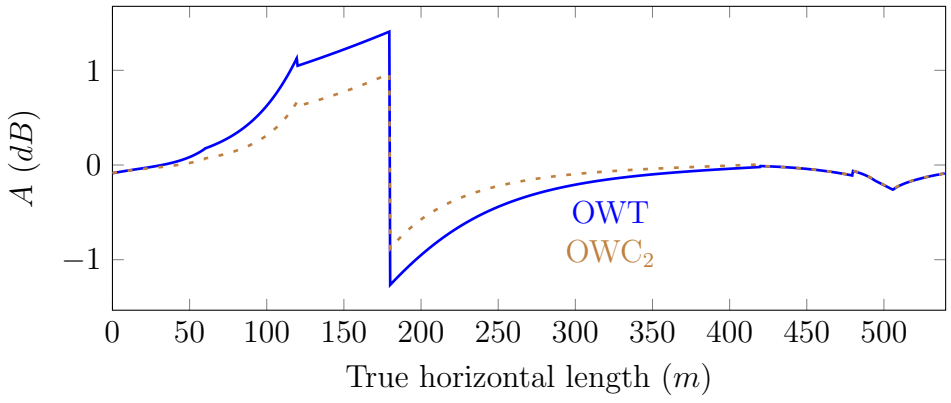

(a) Short spacing

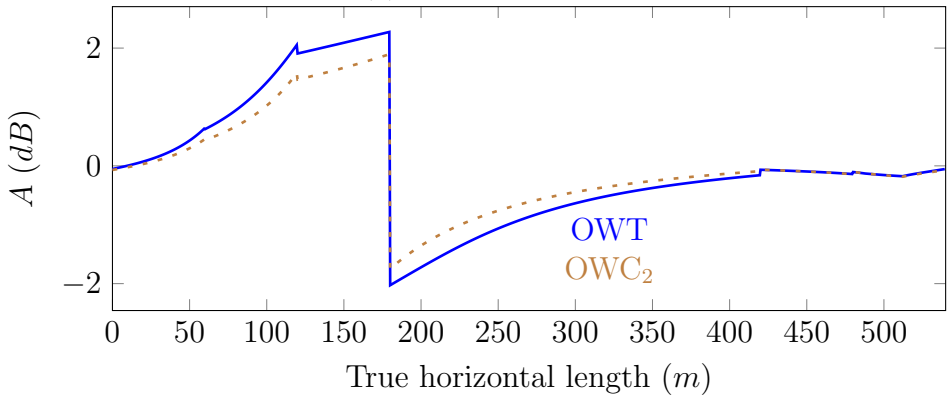

(b) Long spacing

Figure 5.14.: Example 2. Attenuation of the geosignal using short and long spacings for trajectory T_2.

5.2. Deep learning

In this section, we consider a discrete representation of the inverse function $\mathbf{I}_h : \boldsymbol{\mathcal{M}} \times \mathbf{T} \to \mathbf{P}$ that associates each pair of measurements and trajectories $(m, t) \in \boldsymbol{\mathcal{M}} \times \mathbf{T}$ with a corresponding distribution of subsurface properties $P \in \mathbf{P}$ (see Chapter 1). In order to approximate this function, we employ Neural Network (NN) [37]. We provide below a concise overview on how to construct this kind of operators. The existing literature about NN is large, but in here we only intend to briefly introduce geophysicists on some NN and related algorithms that seem to be relevant for the inversion of borehole resistivity measurements.

5.2.1. Neural network

Fully-connected neural network definition: Early formulations of NN, known as Fully-Connected Neural Network (FC-NN), were defined by repeated compositions of simple transformations. Denoting $x = (m, t)$, a FC-NN composed of L *layers* is given by:

$$\mathbf{I}_\theta(x) = (\mathcal{N}^{(L)} \circ \ldots \circ \mathcal{N}^{(l)} \circ \ldots \mathcal{N}^{(2)} \circ \mathcal{N}^{(1)})(x), \tag{5.8}$$

where $\mathcal{N}^{(l)}(x) = \mathbf{s}(W^{(l)} \cdot x + b^{(l)})$, $W^{(l)}$ is a matrix, and $b^{(l)}$ a vector. Thus, $W^{(l)} \cdot x + b^{(l)}$ is an affine transformation. $\mathbf{s}$ is a simple non-linear point-wise mapping, typically the so-called *half-sided rectifier* given by:

$$\mathbf{s}(v_1, ..., v_r) = (\max(0, v_1), ..., \max(0, v_r)). \tag{5.9}$$

We define $\theta^{(l)}$ as a vector composed of all entries of matrices $W^{(l)}$ and vectors $b^{(l)}$ for each layer $l = 1, ..., L$. Thus, $\theta = \{\theta^{(l)} \ : \ 1 \leqslant l \leqslant L\}$ is a large vector of parameters fully determining $\mathbf{I}_\theta$. Due to the varying dimensions of the different matrices $W^{(l)}$ and vectors $b^{(l)}$ at each layer in Equation (5.8), the dimensionality of the input x can change, so it eventually reaches that of the target variable $P \in \mathbf{P}$.

Training a neural network. Data preparation: We consider a finite set S containing m data samples:

$$S = (M, T, P) = \{(m^{[i]}, t^{[i]}, \rho^{[i]}) \ : \ m^{[i]} \in \boldsymbol{\mathcal{M}}, t^{[i]} \in \mathbf{T}, P^{[i]} \in \mathbf{P}, \ 1 \leqslant i \leqslant m\}. \tag{5.10}$$

This set is randomly split into three disjoint subsets, referred to as *training*, *validation*, and *test* sets, respectively:

$$S_{train} = (M_{\text{train}}, T_{\text{train}}, P_{\text{train}}) = \{(m^{[i]}, t^{[i]}, P^{[i]}) \ : \ 1 \leqslant i \leqslant m_1\}, \tag{5.11}$$

$$S_{val} = (M_{\text{val}}, T_{\text{val}}, P_{\text{val}}) = \{(m^{[i]}, t^{[i]}, P^{[i]}) \ : \ m_1 + 1 \leqslant i \leqslant m_2\}, \tag{5.12}$$

$$S_{test} = (M_{\text{test}}, T_{\text{test}}, P_{\text{test}}) = \{(m^{[i]}, t^{[i]}, P^{[i]}) \ : \ m_2 + 1 \leqslant i \leqslant m\}. \tag{5.13}$$

A network $\mathbf{I}_\theta$ can be applied to input data sampled from set S in order to produce a prediction $\mathbf{I}_\theta(m^{[i]}, t^{[i]})$ of its resistivities. The accuracy of such prediction can then be computed via an error function $\mathcal{L}$, *e.g.* the l_2 norm of the difference between both vectors:

$$\mathcal{L}(\mathbf{I}_\theta(m^{[i]}, t^{[i]}), P^{[i]}) = \|\mathbf{I}_\theta(m^{[i]}, t^{[i]}) - P^{[i]}\|_2 \tag{5.14}$$

The numerical process by which the error given by Equation (5.14) is iteratively minimized via a gradient-based algorithm across the entire training set is referred to as *training*, and will be detailed in the next subsection. The validation set S_{val} is employed to perform some high-level NN design decisions, e.g., to modify the network architecture (the dimensions of the different layers) or different parameters controlling the numerical optimization algorithm. After training, predictions are computed for data samples in S_{test} . Then, the network $\mathbf{I}_\theta$ is said to generalize properly if the errors in S_{train} and S_{test} are similar. If in addition such errors are relatively low, we can assume that $\mathbf{I}_\theta$ correctly approximates operator $\mathbf{I}_h$.

Training a neural network. Numerical optimization: A critical feature of NNs is that they are designed as a hierarchical composition of multiple functions which are easy to differentiate. Hence, the chain rule becomes essential to find derivatives of these operators. This is the core idea of the most popular algorithm for implementing gradient descent strategies on NNs, called *back-propagation* in the neural networks literature [71].

Within each gradient descent iteration, we first carry out a forward pass for a given data sample (m_i, t_i) in order to compute a prediction $\mathbf{I}_\theta(m_i, t_i)$ and the corresponding error $\mathcal{L}(\mathbf{I}_\theta(m_i, t_i), P_i)$. Afterwards, this error is backpropagated by applying the chain rule to the composition of functions defining the different layers of the network. Hence, proceeding from the last layer of the model backwards, gradient estimates of the loss function with respect to parameters θ defining $\mathbf{I}_\theta$ can be computed in reverse order as:

$$\frac{\partial \mathcal{L}(\theta)}{\partial \theta^{(L)}}, \ldots, \frac{\partial \mathcal{L}(\theta)}{\partial \theta^{(l+1)}}, \frac{\partial \mathcal{L}(\theta)}{\partial \theta^{(l)}}, \ldots, \frac{\partial \mathcal{L}(\theta)}{\partial \theta^{(1)}} \tag{5.15}$$

The gradient at each layer is derived based on previous gradient computations, parameters θ are updated with some form of gradient descent strategy (e.g., stochastic gradient descent), and the process is iterated over all elements of the training set so as to minimize its error.

The number of iterations during which the model is trained is typically decided by monitoring the value of the loss function $\mathcal{L}$ on elements of the validation set S_{val} that are never used to adjust the network parameters. During training, that value is compared with the loss value attained in S_{train}, in order to stop the optimization process as soon as both quantities start to diverge, which would imply that the network is becoming *too* much adjusted to the training data and failing to generalize, a phenomenon known as *overfitting*.

Convolutional neural networks: As observed from Equation (5.8), NNs are defined as a composition of functions. Thus, they naturally posses a layer-wise hierarchical nature. Therefore, they are ideal candidates to design operators that progressively retain the most salient aspects of the initial input. However, $W^{(l)}$ are dense matrices, connecting every component of the input of a given layer to its output. This results in an excessively large number of parameters that need to be optimized. In order to reduce this number, a popular solution consists of replacing fully-connected affine layers $\mathcal{N}$ by convolutional operators $\mathcal{C}$ defined by convolution kernels f. This localizes computations, effectively reducing the number of parameters in $\mathbf{I}_\theta$. The resulting network is known as a Convolutional Neural Network (CNN) [47]. We provide a rigorous definition of a CNN in Appendix B.1.

Recurrent neural networks: A particular kind of network architectures that are useful for sequence processing (*e.g.* speech, text, or time-related data) are Recurrent Neural Networks (RNNs), introduced in [36]. In here, since successively recorded logging data exhibit a temporal pattern (there is a strong relationship between measurements recorded at a given logging position and at the next one), we also adopt RNNs. For a technical description of this type of networks, see Appendix B.2.

A neural network architecture for inverting borehole resistivity measurements: The NN architecture employed in this work combines both CNNs and RNNs by first reducing the dimensionality of the input measurements by means of a Long Short-Term Memory Network, a specific class of RNNs described in Appendix B.2. Next, the result of this operation serves as input to a series of one-dimensional CNNs, with interleaved *pooling* operators similar to the ones described in Appendix B.1. The output of this second set of

operations becomes the input to a fully-connected layer that maps it into the space $\mathbf{P}$ of subsurface resistivity properties. The network is trained end-to-end by backpropagation until the validation error is no longer decreasing. A pseudo-code of this Deep Neural Network (DNN) is provided in Appendix B.3.

5.2.2. Measurement acquisition system

In this work, we consider the co-axial LWD instrument shown in Figure 5.15. For the aforementioned instrument, we measure attenuation and phase difference of the zz coupling ($\boldsymbol{\mathcal{M}}_1$).

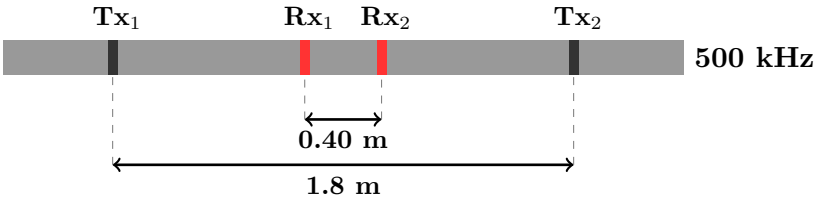

Figure 5.15.: Conventional LWD logging instrument. Tx_i and Rx_i are the transmitters and the receivers, respectively.

In addition, we consider a short-spacing deep azimuthal instrument shown in Figure 5.7. For this instrument, we record attenuation and phase difference as another set of measurements ($\boldsymbol{\mathcal{M}}_2$). Moreover, we consider geosignal defined in Equation (5.7) as our third set of measurements ($\boldsymbol{\mathcal{M}}_3$).

5.2.3. Trajectory parameterization

We select a fixed number of logging positions (n_p) based on the depth of investigation of the logging instruments. For our instruments, the largest depth of investigation is close to 20 m. By considering the logging step size equal to one foot, we select $n_p = 65$.

We consider an arbitrary (but close to horizontal) trajectory, as it is customary in geosteering applications. Since we assume a 1D layered media along a particular direction of the well trajectory, we select the azimuthal degree of the trajectory to be always equal to zero.

With the above assumptions, we discretize (parameterize) the well trajectory as follows. We consider t_{ini} to be the initial trajectory dip angle. We assume that the trajectory dip angle can vary while drilling by t_v in each step. Hence,

at each logging position (i), the trajectory dip angle is:

$$t_i = t_{ini} + (i-1)t_v, \ i = 1, \cdots, n_p, \tag{5.16}$$

where t_i is the trajectory dip angle at the i-th position.

5.2.4. Material properties parameterization

In 1D inversion of borehole resistivity measurements, it is often sufficient to recover a media containing three layers at each logging position, which are discretized with seven variables: (1) the horizontal and vertical resistivity of the layer where the tool is currently located (ρ_h and ρ_v, respectively); (2) the resistivity of the upper and lower layers of the current position (ρ_u and ρ_l, respectively); (3) the vertical distance from the current position of the tool to the upper and lower bed boundary positions (d_u and d_l, respectively); and (4) the dip angle of the layers (β) (see Figure 5.16). Our Deep Learning algorithm will provide an estimate of these seven numbers at each logging position.

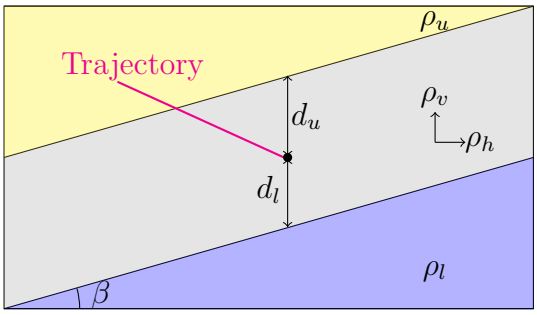

Figure 5.16.: Inversion variables in a 1D media. The black circle indicates the last logging position.

5.2.5. Traning the DNN

To produce reliable training and validation sets, and to avoid full randomness which leads to a huge and non-physical set of data (see Figure 5.17), we need to consider the physical and geological properties of the subsurface.

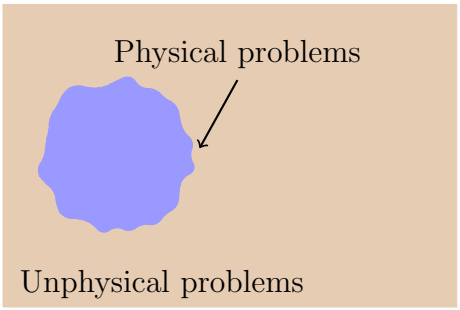

Figure 5.17.: The entire set of random synthetic model problems and the physically meaningful scenarios.

5.2.5.1. Material properties

In order to produce our training and validation sets, we consider $\rho_u, \rho_l \in [1, 10^3]$. Moreover, because our measurements of interest are highly sensitive to the resistivity values, and we need these values to be comparable, we consider them in logarithmic scale. Thus, our random variables become: $\log(\rho_l), \log(\rho_u) \in [0, 3]$. Additionally, in the case of ρ_v and ρ_h, we need to consider that in geological structures, we have the following observed physical restrictions:

$$\rho_h \leqslant \rho_v \leqslant 10\rho_h. \tag{5.17}$$

Therefore, we obtain:

$$1 \leqslant \underbrace{\frac{\rho_v}{\rho_h}}_{a} \leqslant 10, \tag{5.18}$$

where a is the anisotropy factor. In order to consider (5.17) in our calculations, we select random values of $\log(a)$ in between:

$$0 \leqslant \log(a) \leqslant 1. \tag{5.19}$$

Moreover, since we want to have $\log(\rho_v) \in [0, 3]$, we select $\log(\rho_h) \in [0, 3 - \log(a)]$. We consider $d_l, d_u \in [0.01, 10]$ meters. Analogous to the resistivity values, we consider them in logarithmic scale, i.e., our variables become $\log(d_l), \log(d_u) \in [-2, 1]$. In geological layers, we assume that the deep angle is $\beta \in [-10°, 10°]$.

Hence, we select $\log(\rho_u)$, $\log(\rho_l)$, $\log(\rho_h)$, a, $\log(d_u)$, $\log(d_l)$, and β randomly within their aforementioned ranges of variation to build the materials for our synthetic forward models.

5.2.5.2. Trajectory

Since we consider an almost horizontal trajectory, as it occurs in most geosteering applications, we have $t_{ini} \in [83^\circ, 97^\circ]$. Moreover, we further assume that the tool rotates a maximum of 3° in a 20 meters section. In addition, since the direction of the trajectory dip angle is often changing gradually and almost constantly at each logging position, for $n_p = 65$ we have $t_v \in [-0.045^\circ, 0.045^\circ]$.

By selecting randomly t_{ini} and t_v in their aforementioned ranges of variation, we build the trajectory for our forward problem.

5.2.6. Results

For this problem, we consider one million randomly selected model problems (80% training, 10% validation, and 10% test). Figure 5.18 shows the accuracy of the trained DNN when we only consider the set of measurements $\boldsymbol{\mathcal{M}}_2$, i.e., $\boldsymbol{\mathcal{M}} = \boldsymbol{\mathcal{M}}_2$. The red line indicates the perfect approximation where the predicted value and the ground truth are equal. Besides, the upper and lower blue lines show percentiles 10 and 90, respectively. The aforementioned percentiles provide a reliable uncertainty quantification. In a perfect approximation, the blue lines should coincide with the red one. Therefore, a lower distance between the blue lines and the red one indicates a better approximation. As evident in the figures, the cloud of points is much denser close to the red line, which promises an acceptable approximation. However, for the anisotropy factor a, the DNN is almost unable to predict the correct value, and consequently, it can not predict ρ_v as precisely as the other variables.

Analogously, Figure 5.19 illustrates the results when we have $\boldsymbol{\mathcal{M}} = \boldsymbol{\mathcal{M}}_2 \cup \boldsymbol{\mathcal{M}}_3$. One can see that the blue lines are closer compared to Figure 5.18. Moreover, the distribution area of the points is smaller, and the cloud of points is denser close to the red line. However, the approximation of the anisotropy factor a is still unacceptable, although better than in the previous case.

Figure 5.20 illustrates the results when we have $\boldsymbol{\mathcal{M}} = \boldsymbol{\mathcal{M}}_1 \cup \boldsymbol{\mathcal{M}}_2 \cup \boldsymbol{\mathcal{M}}_3$. In the aforementioned results, the concentration of points is closer to the red line compared to the previous results. Moreover, the blue lines are closer to each other. More importantly, for the first time, we have an acceptable approximation of anisotropy factor a. Since the aforementioned DNN shows the best performance, we use it to invert the examples presented in this work.

Figure 5.21 illustrates the inversion of a three-layer media in which the middle layer is more conductive than the other two ones, and it is anisotropic. The aforementioned results are not as precise as the one of a gradient-based method. However, as primary results, they are encouraging. The results show that for the isotropic layer, the prediction of the resistivity is better than the

one for the anisotropic layer. This probably occurs because of lack of required accuracy for anisotropy factor a. The prediction of d_u and d_l provides an acceptable view of the material surrounding the instrument. Figures 5.22 and 5.23 show a comparison between the attenuations and the phase differences of measurements corresponding to the exact and predicted (inverted) models. These results show a better approximation of $\boldsymbol{\mathcal{M}}_1$.

Figure 5.24 displays an inversion performed on a three-layer media in which the middle layer is more resistive and isotropic. We consider the other two layers to be anisotropic. As in the previous model problem, results show discrepancies in the anisotropic layers probably because of the lack of a good approximation of anisotropy factor a. Figures 5.25 and 5.26 compare the measurements corresponding to the exact and predicted (inverted) models.

Figure 5.27 describes the inversion performed on a synthetic example containing a sequence of 1D layer media. Each 1D model consists of four layers. The results are not perfect, and the lack of accuracy for anisotropy factor a causes a poor approximation of the resistivity in the anisotropic layer. Approximation of d_u and d_l can predict a first approximation of the surrounding area of the tool, although, a better approximation of d_u and d_l is necessary for a more accurate estimation of bed boundary positions. Figures 5.28 and 5.29 compare the measurements corresponding to the exact and predicted (inverted) models. As in previous cases, the best approximation belongs to $\boldsymbol{\mathcal{M}}_1$.

Figures 5.30, 5.31, and 5.32 present the results of the inversion for a synthetic example in which a negative dipping of the layers appears in our synthetic formation. Figures 5.33, 5.34, and 5.35 show the results of the inversion of another synthetic example in which the formation is similar to the one of Figure 5.30, but considering a different trajectory. Again, the results lack accuracy. However, they provide an adequate initial approximation, and we are able to perform the above inversion in a few seconds for over a thousand logging positions. Considering the aforementioned results indicates that the use of DNN for inversion of the resistivity measurements may be a viable option. However, an intensive amount of research work is needed to achieve the required accuracy by the oil & gas industry.

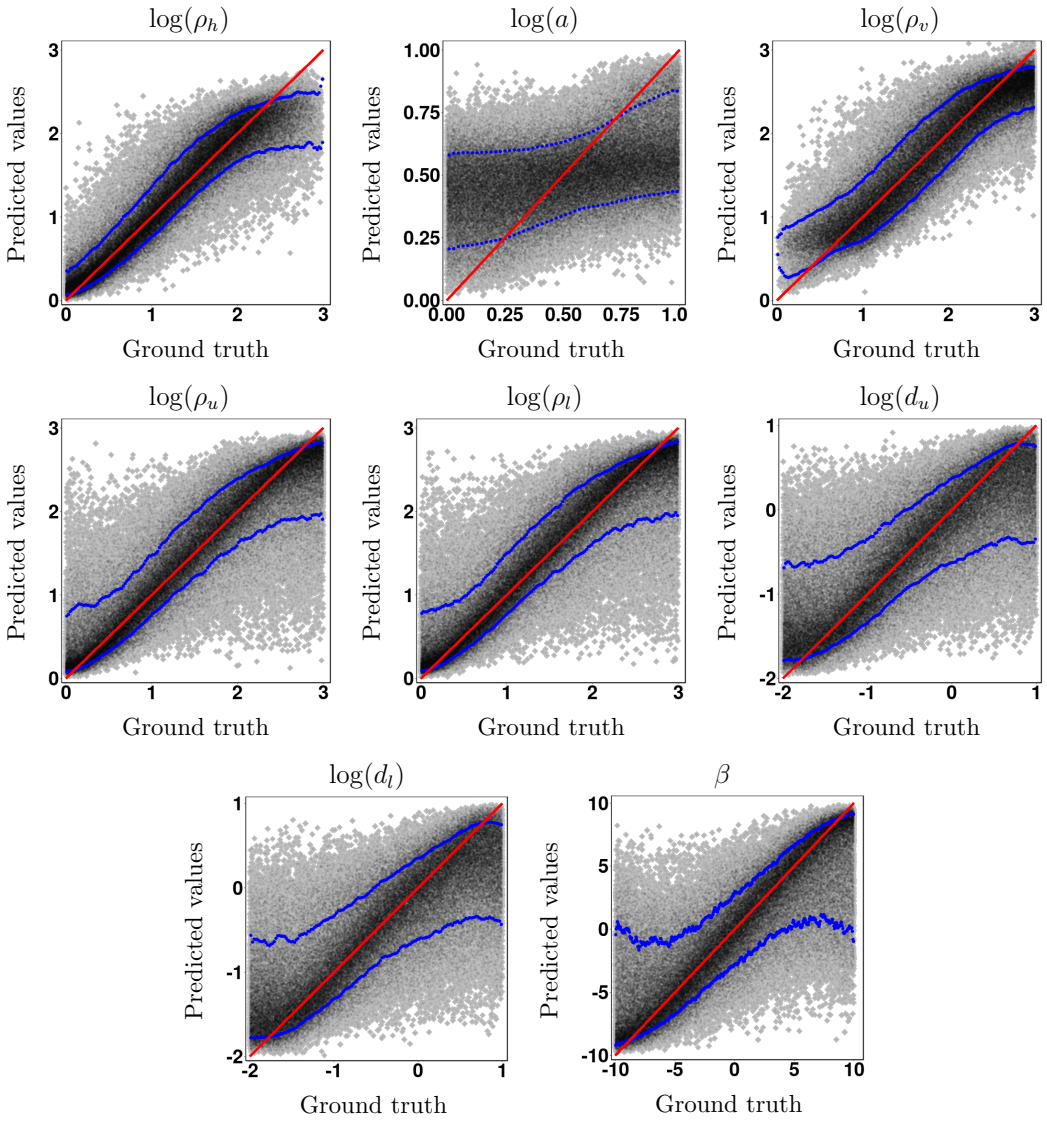

Figure 5.18.: Model problem 2. Comparison between the ground truth and predicted values using a trained DNN for $\boldsymbol{\mathcal{M}} = \boldsymbol{\mathcal{M}}_2$. Red line indicates the equality of the predicted values and the ground truth. The blue lines correspond to the 10 and 90 percentiles, respectively.

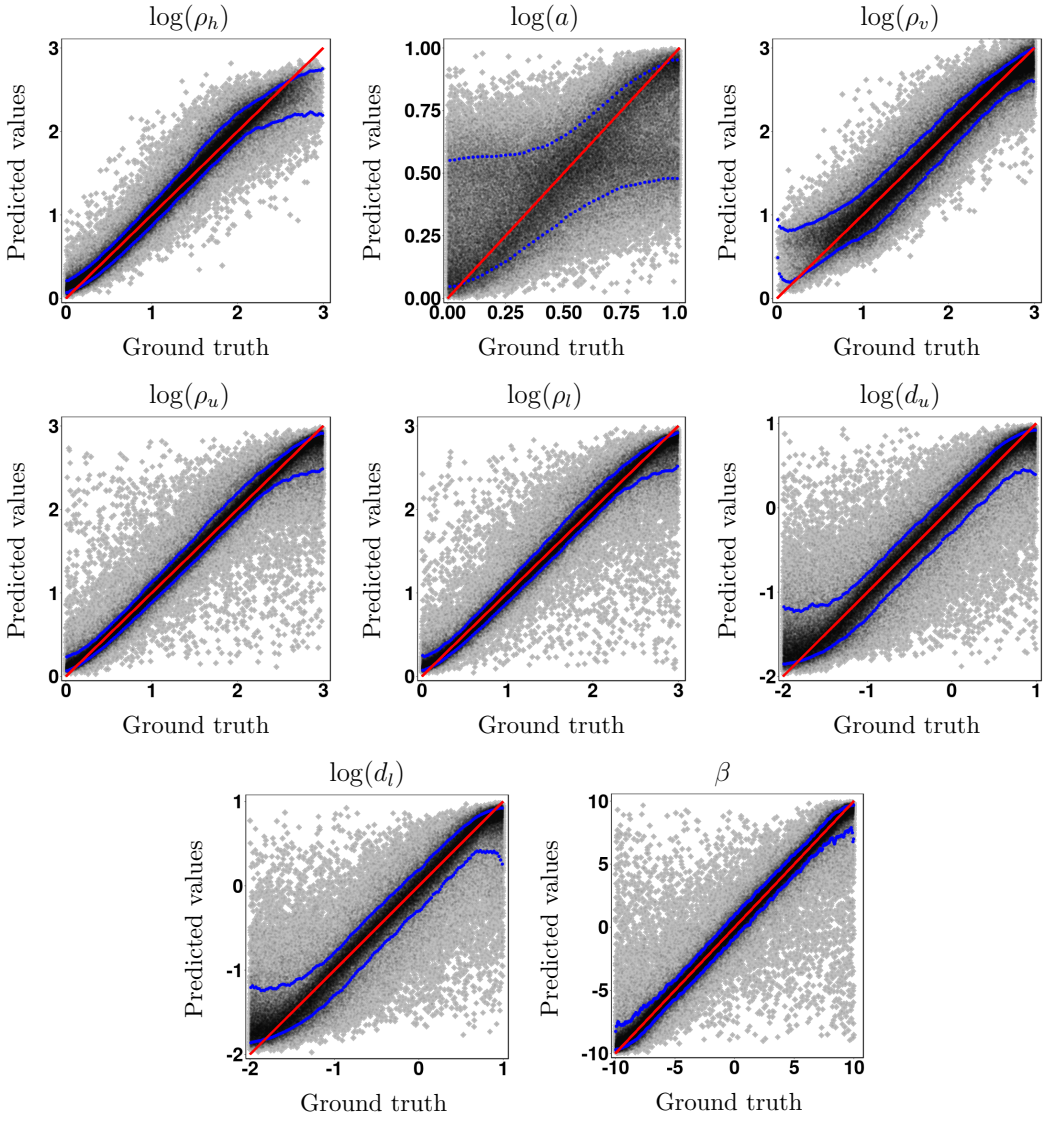

Figure 5.19.: Model problem 2. Comparison between the ground truth and predicted values using a trained DNN using $\boldsymbol{\mathcal{M}} = \boldsymbol{\mathcal{M}}_2 \cup \boldsymbol{\mathcal{M}}_3$. Red line indicates the equality of the predicted values and the ground truth. The blue lines correspond to the 10 and 90 percentiles, respectively.

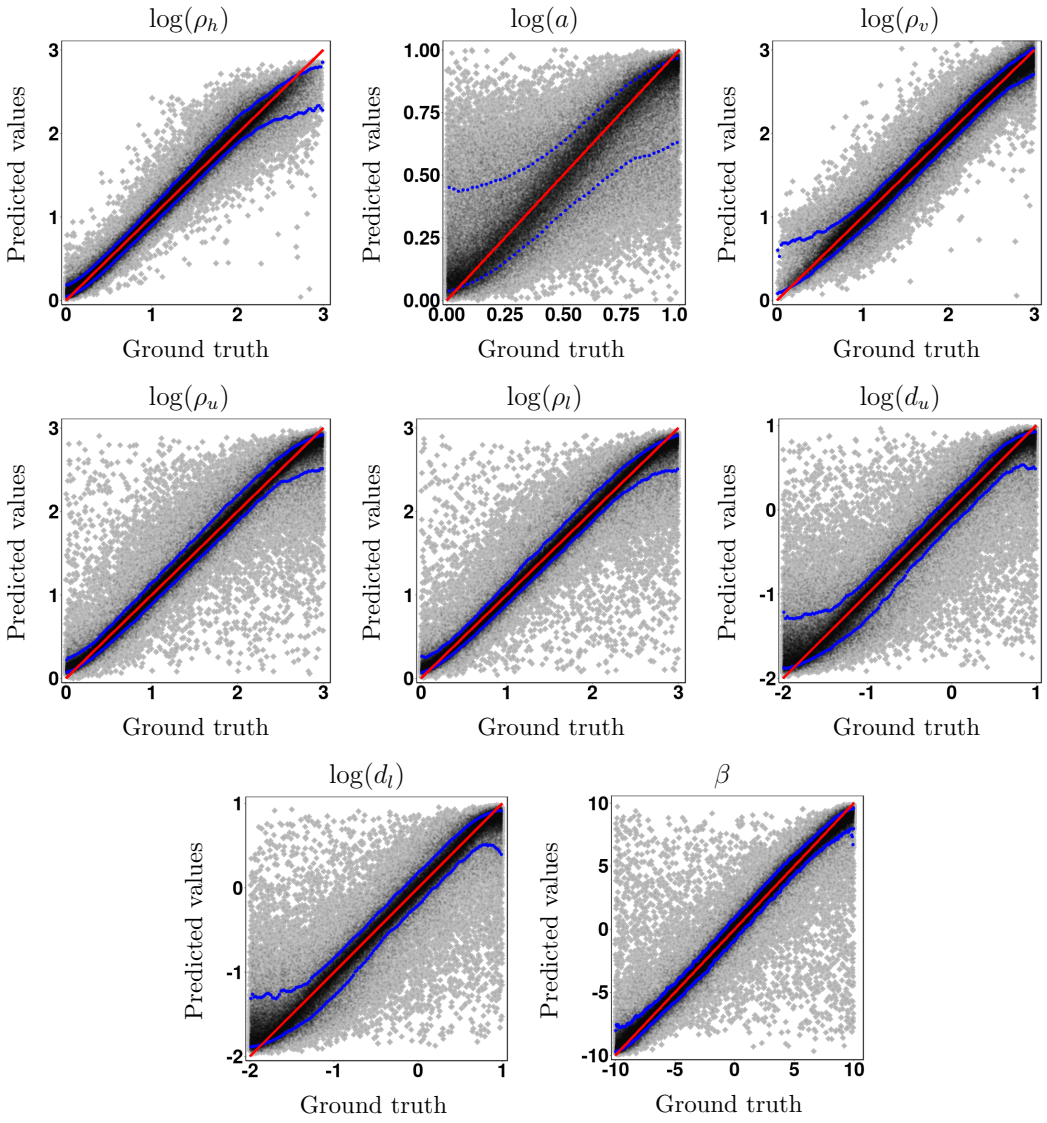

Figure 5.20.: Model problem 2. Comparison between the ground truth and predicted values using a trained DNN using $\boldsymbol{\mathcal{M}} = \boldsymbol{\mathcal{M}}_1 \cup \boldsymbol{\mathcal{M}}_2 \cup \boldsymbol{\mathcal{M}}_3$. Red line indicates the equality of the predicted values and the ground truth. The blue lines correspond to the 10 and 90 percentiles, respectively.

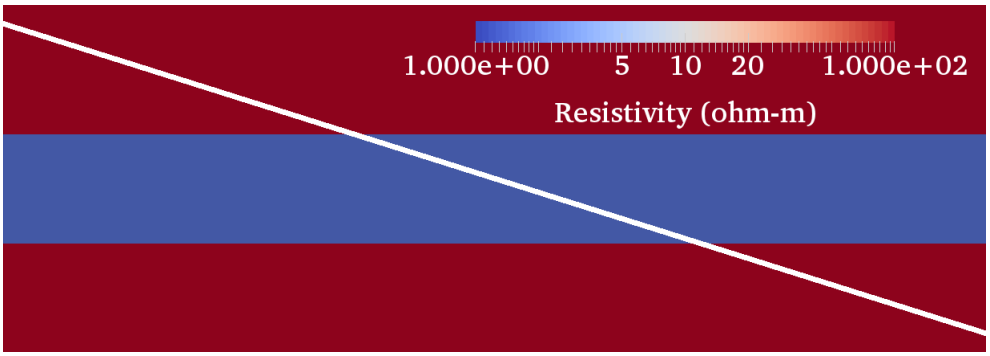

(a) Actual formation

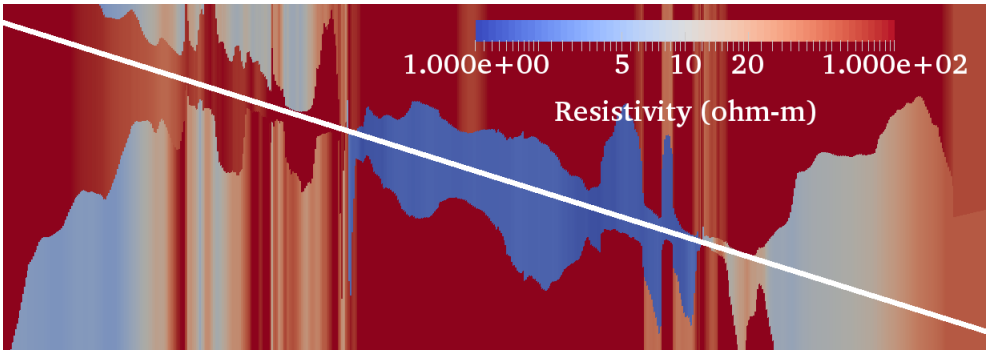

(b) Predicted (inverted) formation

Figure 5.21.: Model problem 1. Comparison between actual and predicted (inverted) formation.

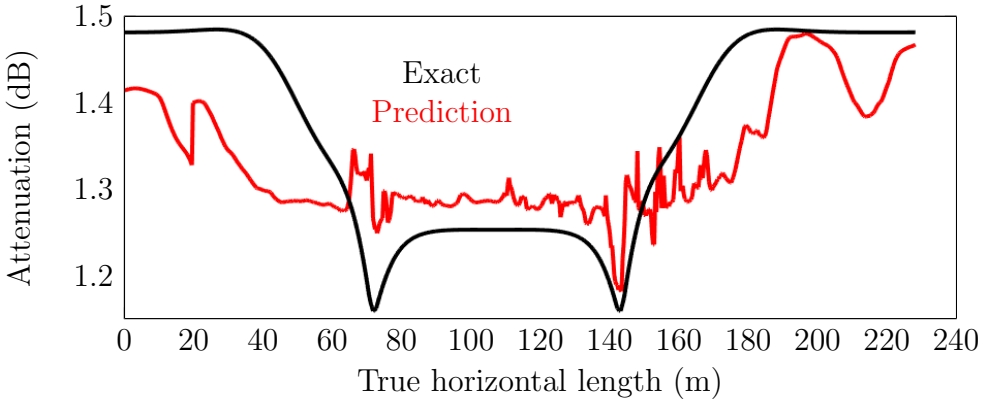

(a) $\mathcal{M}_1$

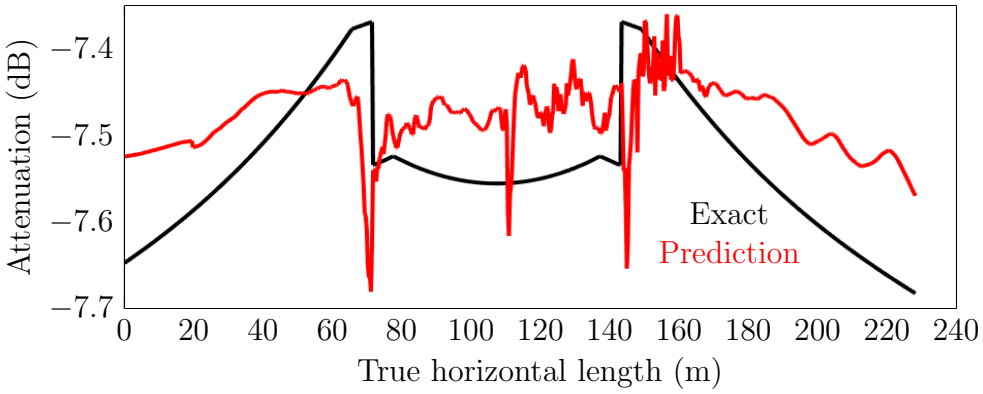

(b) $\mathcal{M}_2$

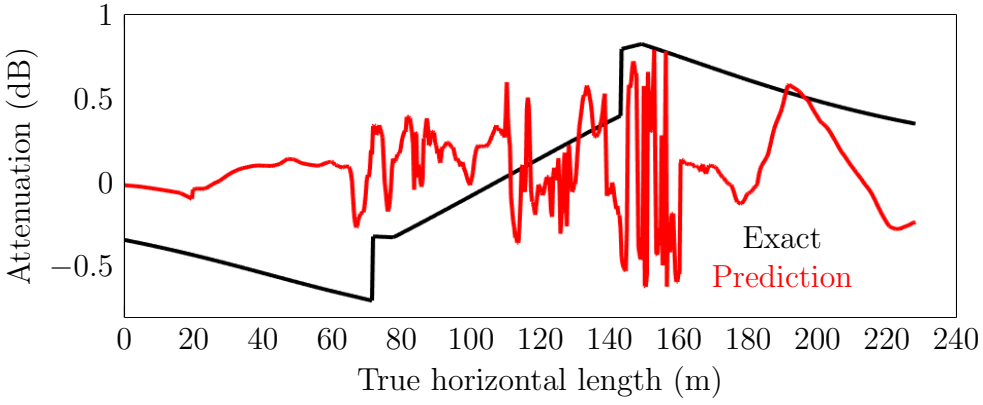

(c) $\mathcal{M}_3$

Figure 5.22.: Model problem 1. Comparison between exact attenuations of the measurements and those corresponding to the predicted (inverted) model using our DNN.

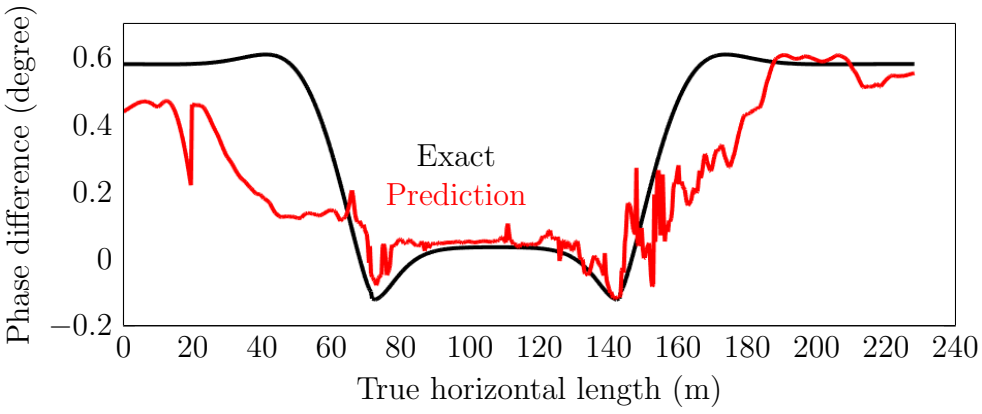

(a) $\mathcal{M}_1$

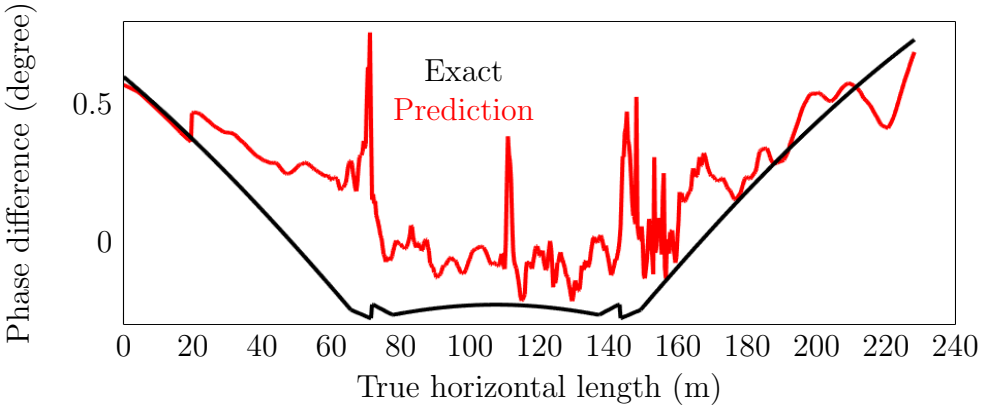

(b) $\mathcal{M}_2$

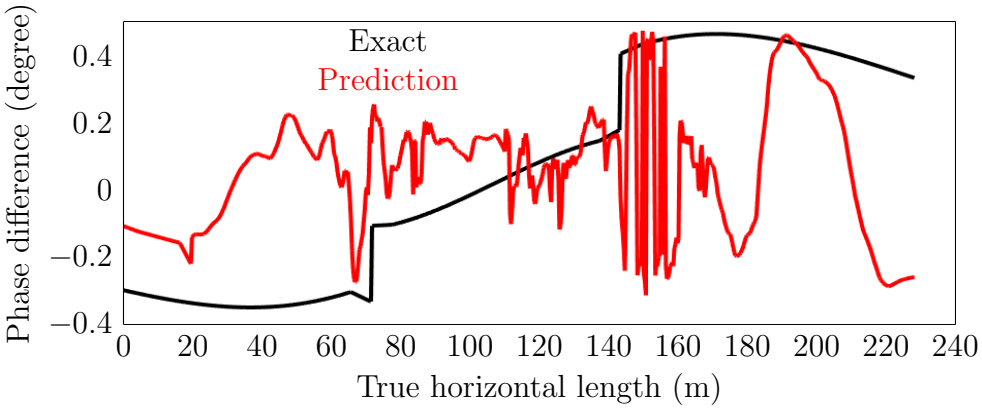

(c) $\mathcal{M}_3$

Figure 5.23.: Model problem 1. Comparison between exact phase differences of the measurements and those corresponding to the predicted (inverted) model using our DNN.

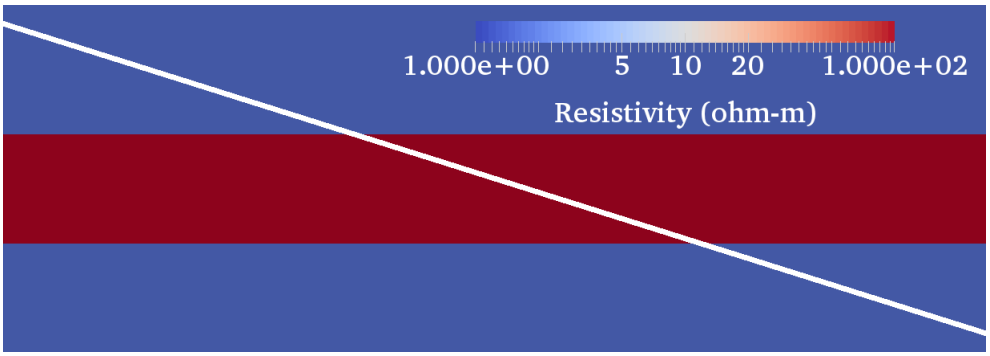

(a) Actual formation

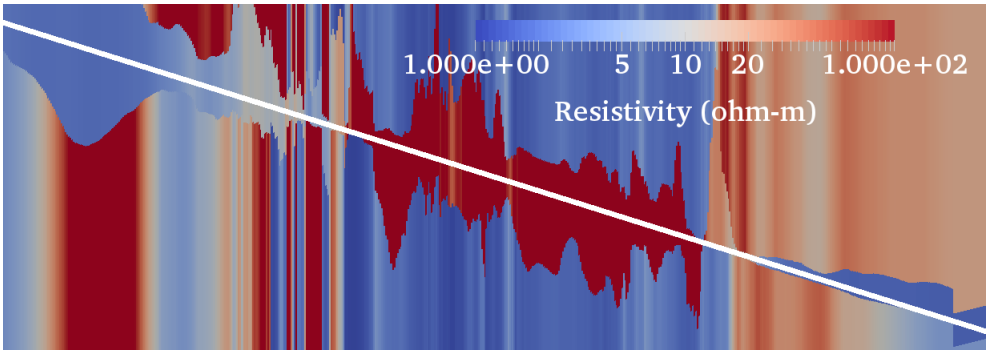

(b) Predicted (inverted) formation

Figure 5.24.: Model problem 2. Comparison between actual and predicted (inverted) formation.

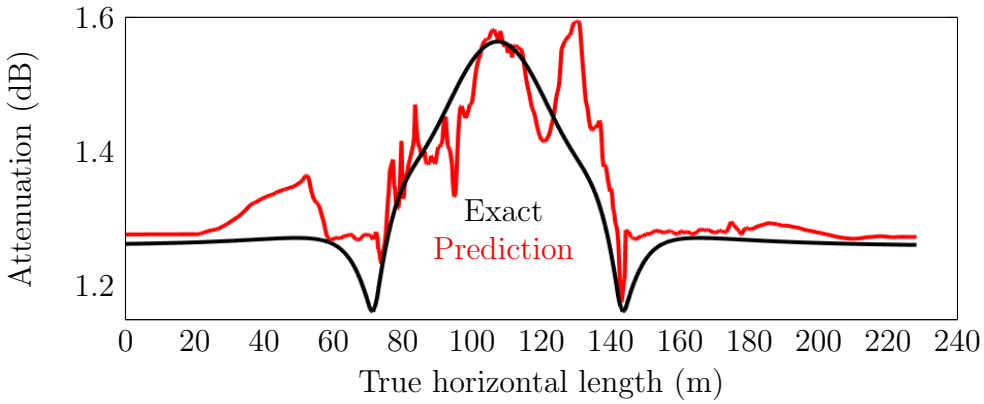

(a) $\mathcal{M}_1$

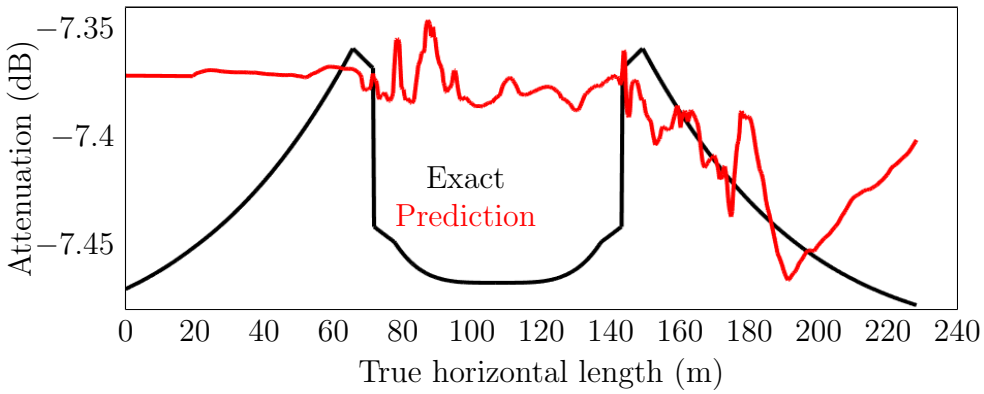

(b) $\mathcal{M}_2$

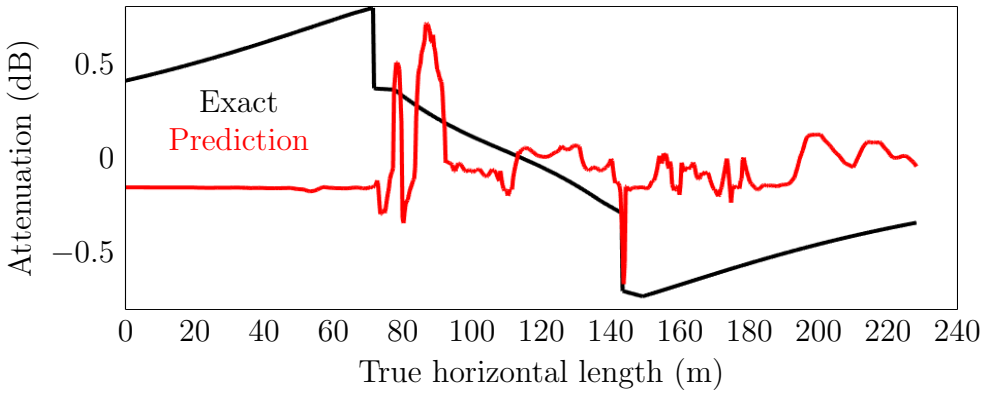

(c) $\mathcal{M}_3$

Figure 5.25.: Model problem 2. Comparison between exact attenuations of the measurements and those corresponding to the predicted (inverted) model using our DNN.

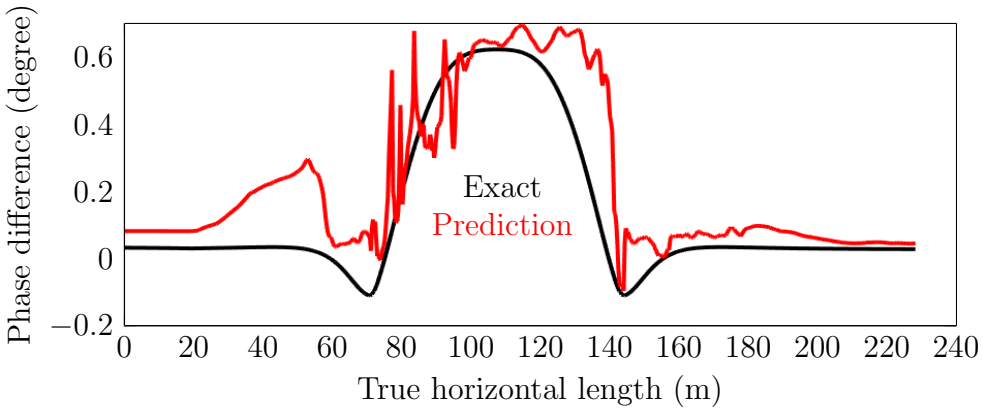

(a) $\mathcal{M}_1$

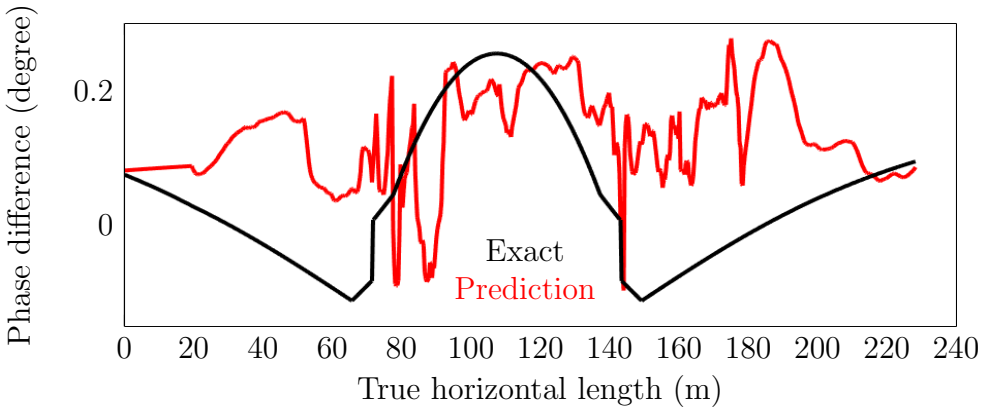

(b) $\mathcal{M}_2$

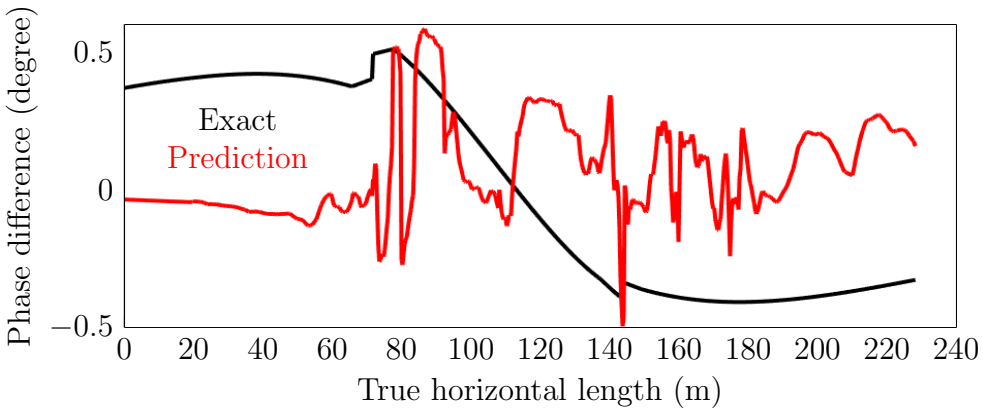

(c) $\mathcal{M}_3$

Figure 5.26.: Model problem 2. Comparison between exact phase differences of the measurements and those corresponding to the predicted (inverted) model using our DNN.

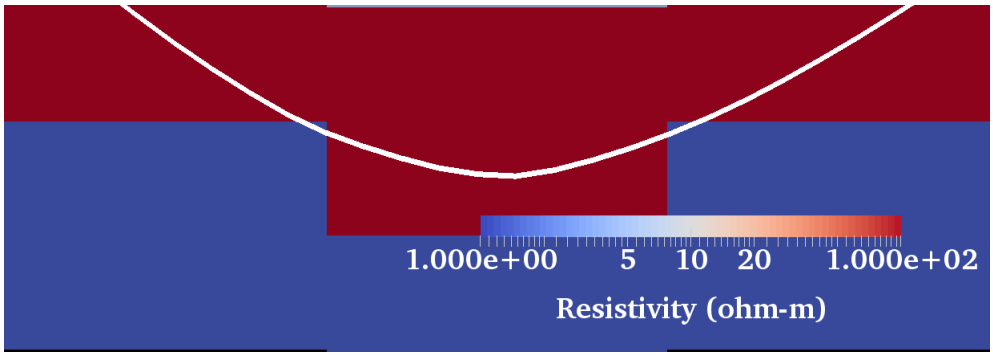

(a) Actual formation

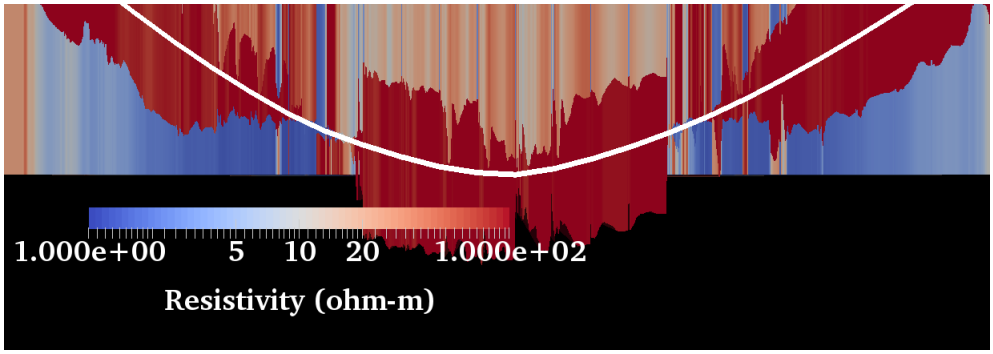

(b) Predicted (inverted) formation

Figure 5.27.: Model problem 3. Comparison between actual and predicted (inverted) formation.

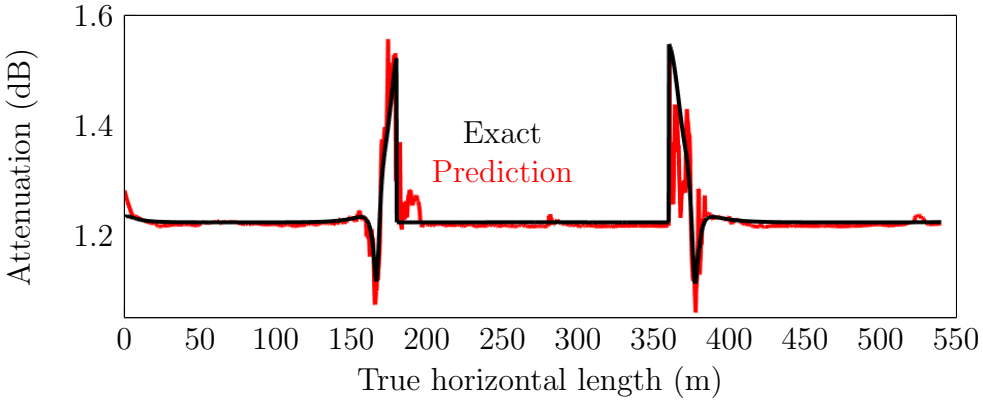

(a) $\mathcal{M}_1$

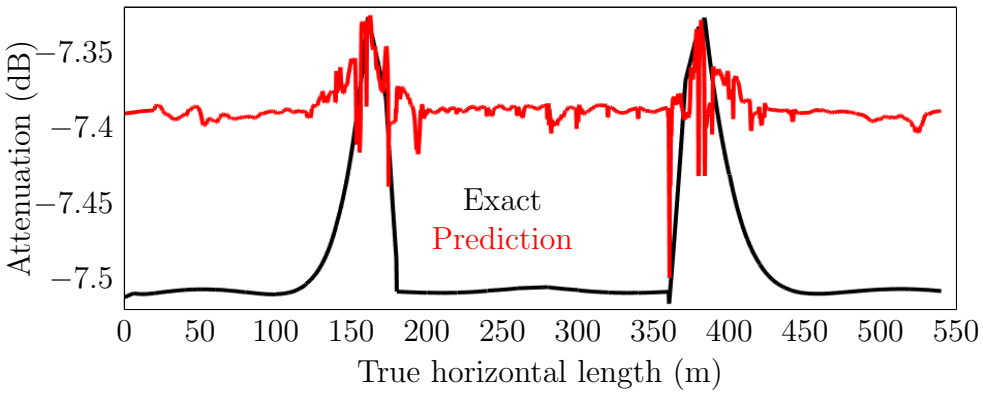

(b) $\mathcal{M}_2$

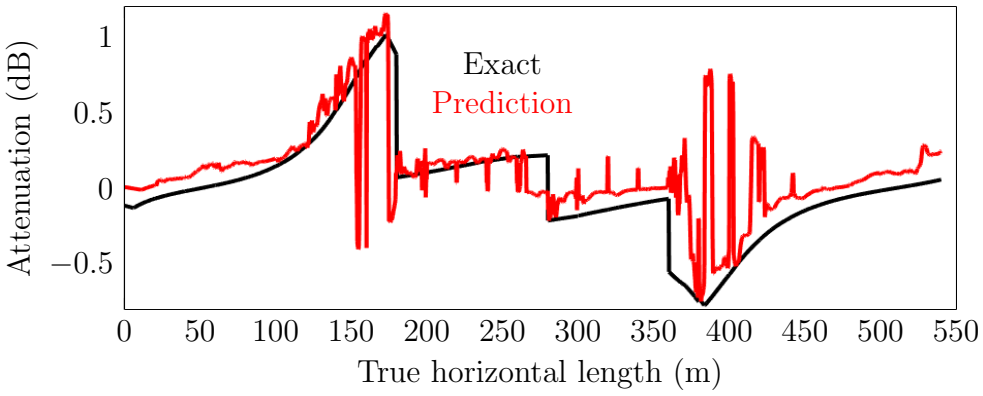

(c) $\mathcal{M}_3$

Figure 5.28.: Model problem 3. Comparison between exact attenuations of the measurements and those corresponding to the predicted (inverted) model using our DNN.

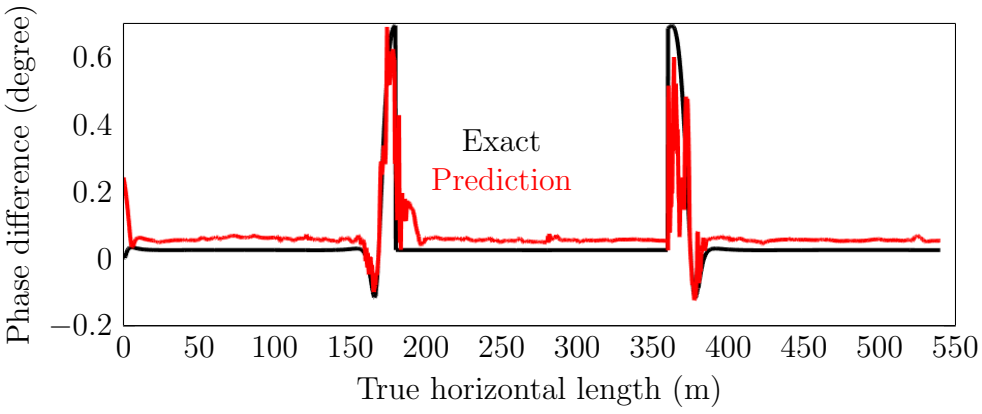

(a) $\mathcal{M}_1$

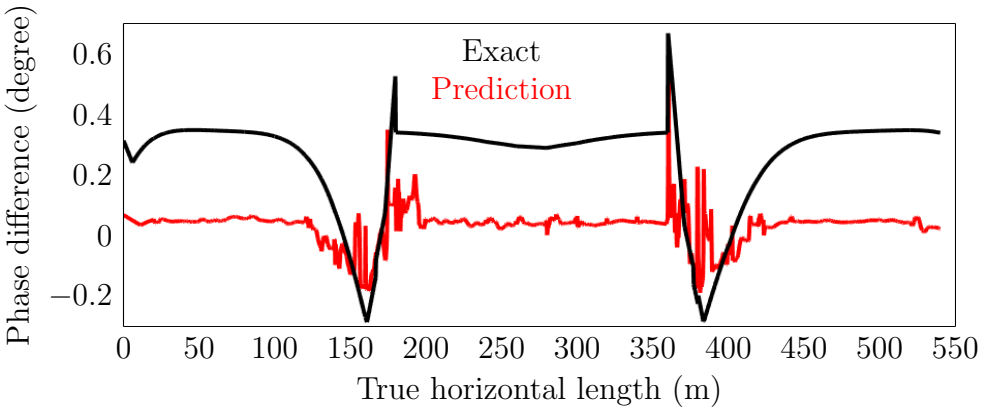

(b) $\mathcal{M}_2$

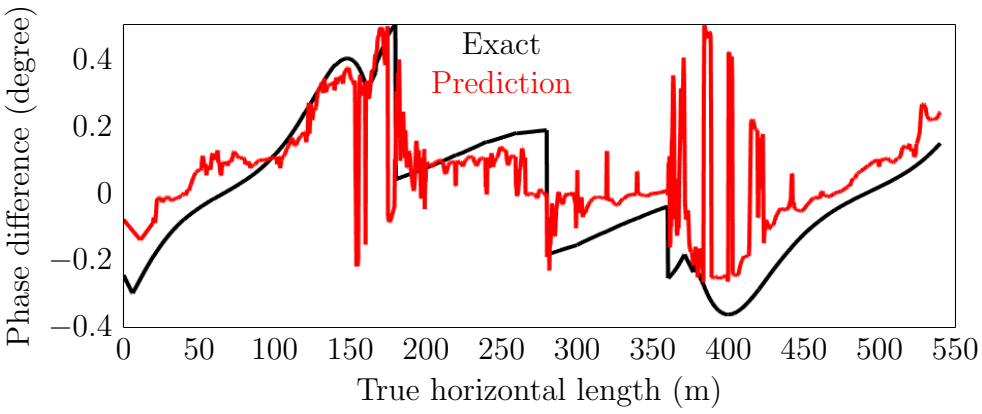

(c) $\mathcal{M}_3$

Figure 5.29.: Model problem 3. Comparison between exact phase differences of the measurements and those corresponding to the predicted (inverted) model using our DNN.

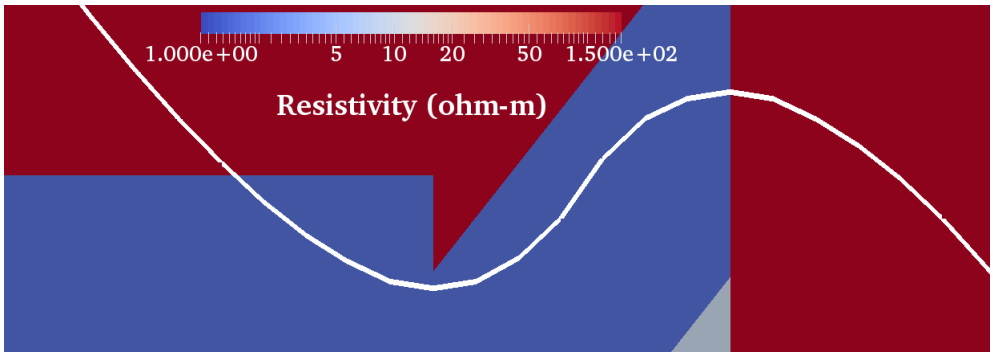

(a) Actual formation

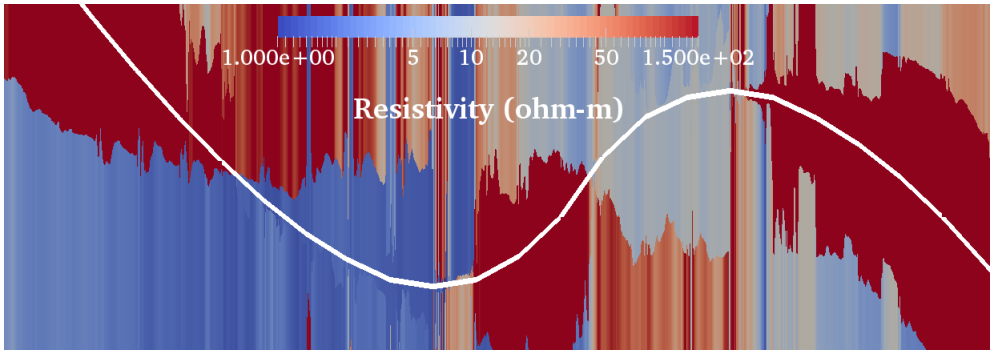

(b) Predicted (inverted) formation

Figure 5.30.: Model problem 4. Comparison between actual and predicted (inverted) formation.

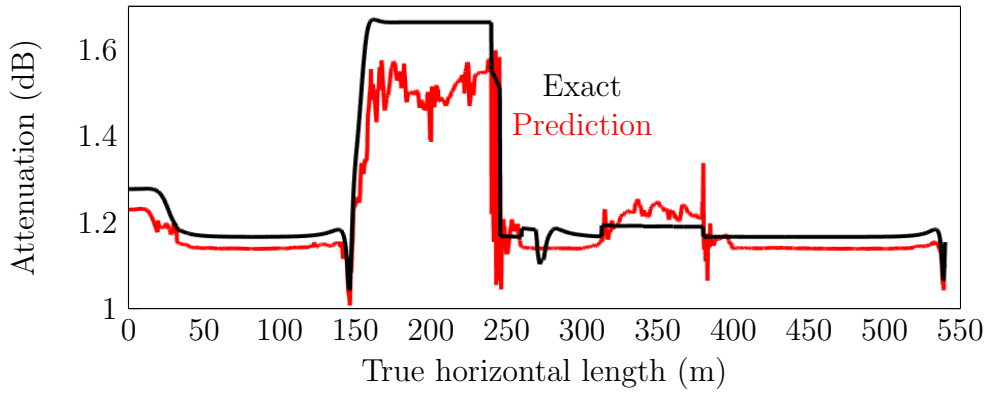

(a) $\mathcal{M}_1$

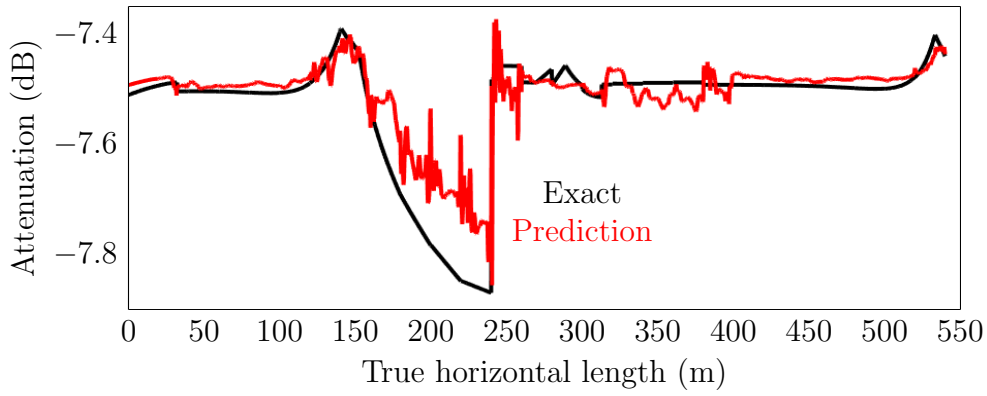

(b) $\mathcal{M}_2$

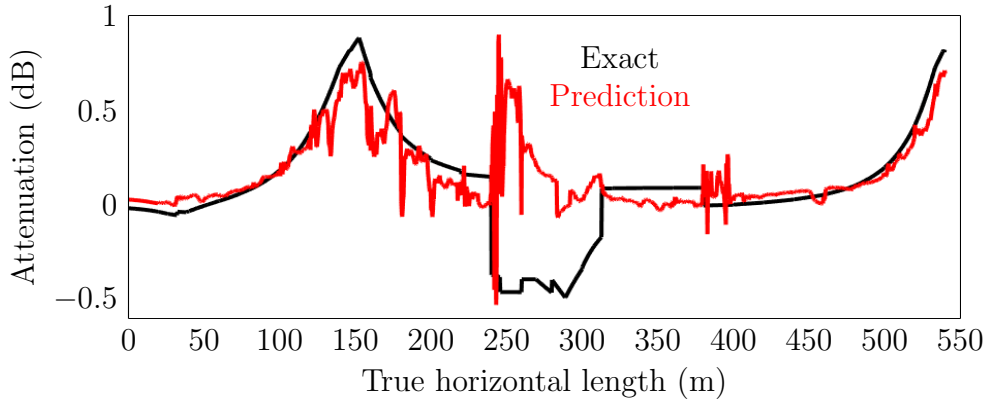

(c) $\mathcal{M}_3$

Figure 5.31.: Model problem 4. Comparison between exact attenuations of the measurements and those corresponding to the predicted (inverted) model using our DNN.

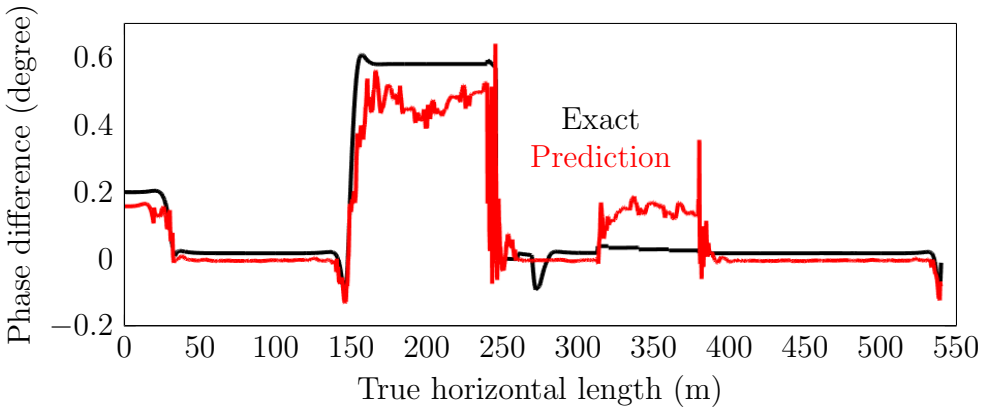

(a) $\mathcal{M}_1$

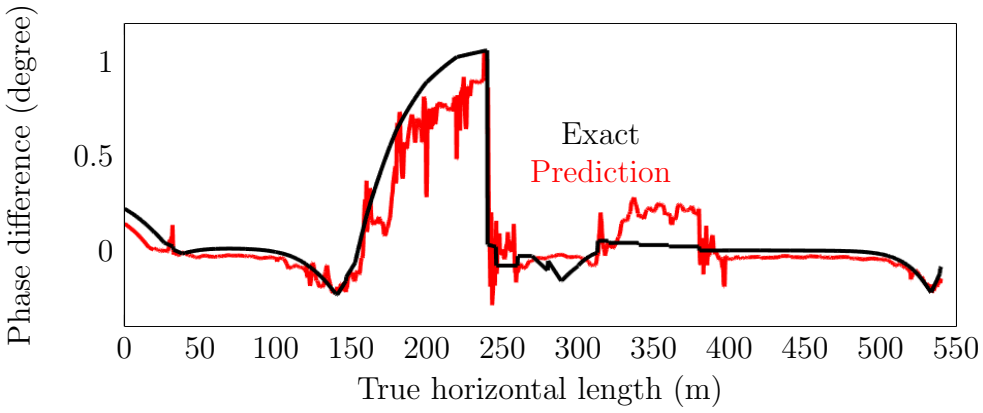

(b) $\mathcal{M}_2$

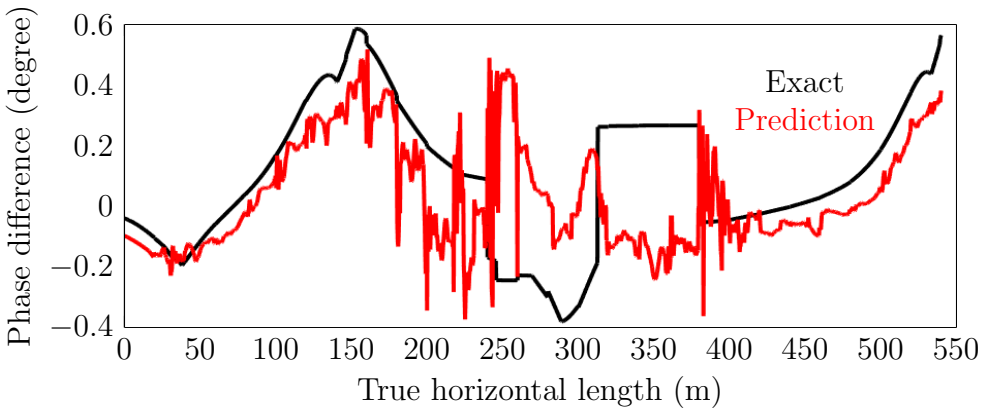

(c) $\mathcal{M}_3$

Figure 5.32.: Model problem 4. Comparison between exact phase differences of the measurements and those corresponding to the predicted (inverted) model using our DNN.

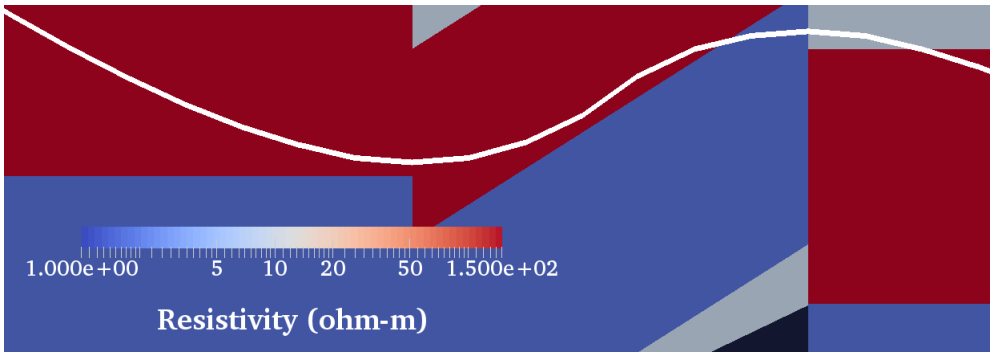

(a) Actual formation

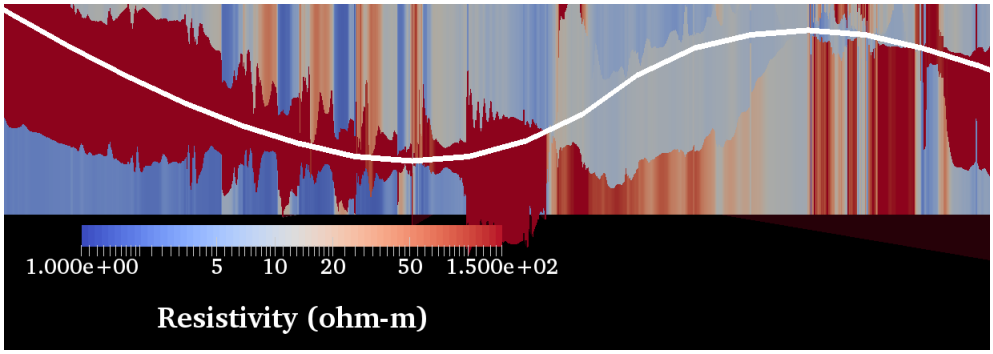

(b) Predicted (inverted) formation

Figure 5.33.: Model problem 5. Comparison between actual and predicted (inverted) formation.

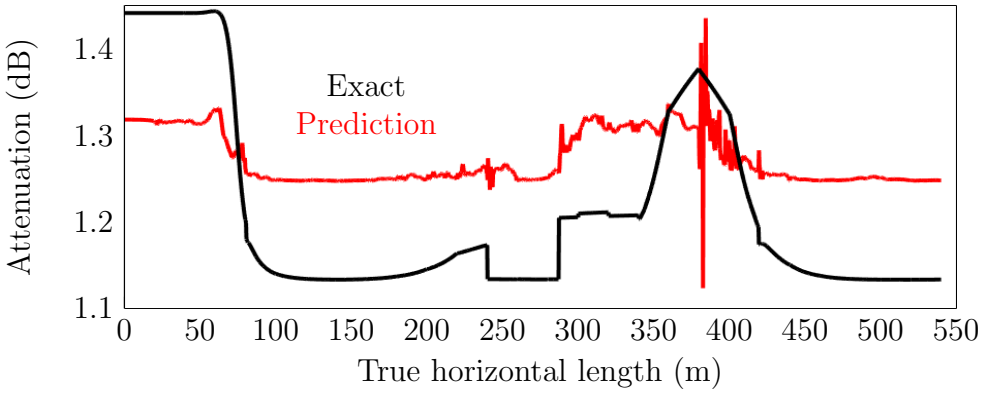

(a) $\mathcal{M}_1$

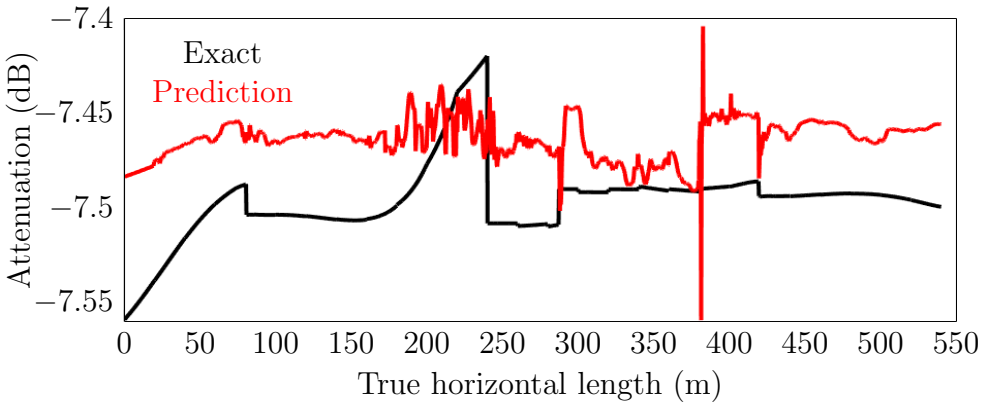

(b) $\mathcal{M}_2$

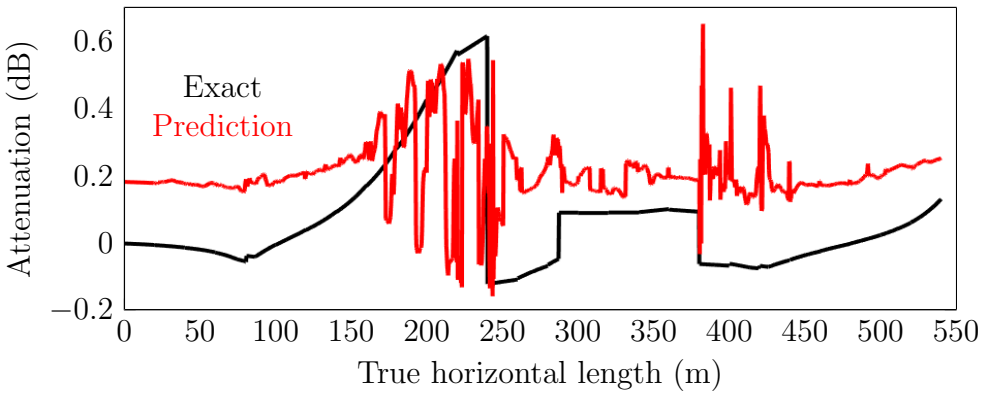

(c) $\mathcal{M}_3$

Figure 5.34.: Model problem 5. Comparison between exact attenuations of the measurements and those corresponding to the predicted (inverted) model using our DNN.

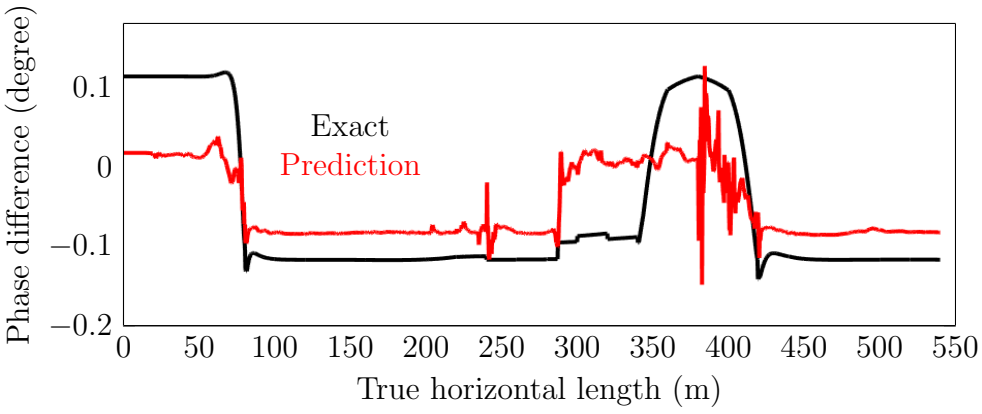

(a) $\mathcal{M}_1$

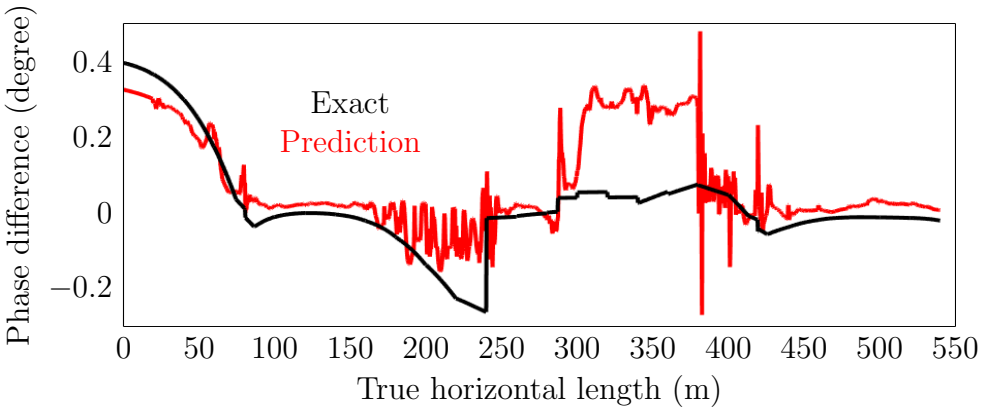

(b) $\mathcal{M}_2$

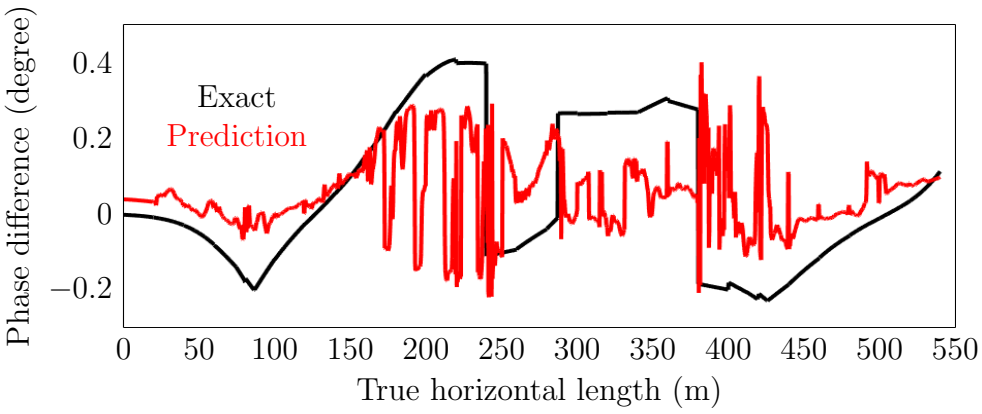

(c) $\mathcal{M}_3$

Figure 5.35.: Model problem 5. Comparison between exact phase differences of the measurements and those corresponding to the predicted (inverted) model using our DNN.

6. Conclusions and Future work

6.1. Conclusions

We proposed a Multiscale Hankel Finite Element Method (Ms-HFEM) for solving Maxwell's equations in a 1D Transversaly Isotropic (TI) media excited by a 3D arbitrarily oriented point dipole. The multiscale Finite Element Method (FEM) pre-computes the fundamental fields, and correction and multiscale basis functions. As a result, this computation is expensive if only a single logging position is studied, but it becomes competitive as the number of logging position grows.

The aforementioned numerical method overcomes the limitations of the existing semi-analytic ones. Besides, we can use an adjoint-state method to compute the derivatives with respect to inversion variables which we use to form the Jacobian matrix needed in a gradient-based inversion method.

Moreover, using the numerical method, we can consider arbitrary resistivity distribution to better map the reservoir and its Oil-Water Transition (OWT) zone. By doing so, we may increase the productivity from the well.

Besides, we can easily extend our numerical solver to other multiphysics problem and models, such as elasto-acoustic, cross-bedded formation.

6.1.1. 1.5D Ms-HFEM

The numerical method produces highly accurate solutions, as our numerical validations experiments show. Additionally, computation of the parametrization derivatives is straightforward by merely considering the adjoint formulation. By using this method, it is possible to consider arbitrary resistivity distributions along the z direction, while semi-analytic methods only allow for piecewise constant material coefficients.

The method we propose is still slower than the semi-analytic one. The most time-consuming part of our method is to compute the primary field. However, in the case of piecewise constant resistivity distribution, we can obtain the fundamental field analytically, which decreases the cost of computing the primary field considerably. Nonetheless, this work employs a full FEM implementation to preserve the generality of the method. This enables us to consider arbitrary

resistivity distributions (other than just piecewise constant ones). Because of the lack of existence of a semi-analytic method that can model the aforementioned case, our methodology is a viable alternative. To use a semi-analytic method, we can approximate the non-constant resistivity distribution using multiple constant resistivity distributions. However, this piecewise-constant representation leads to an extensive error and a bothersome implementation when computing the derivatives to form the Jacobian matrix to perform the inversion.

6.1.2. Derivatives

We have developed an adjoint-based formulation to compute the derivatives of geophysical resistivity measurements with respect to the bed boundary positions and resistivity value of each layer. The formulation is first deduced for 3D Maxwell's equation. Then, we extend the formulation for the case of a 1D Earth model. We verified our formulations by comparing the numerical results with those obtained using an analytical solution for a potential equation and with a finite differences technique for a 1.5D Maxwell's system. Using the adjoint state method, we can compute the derivatives at (almost) no additional cost in time with respect to that needed to solve the forward problem, and we obtain an accurate evaluation of the derivatives.

6.1.3. Applications

Analyzing OWT zones: In an oil reservoir, it is customary to consider, and Oil-Water Contact (OWC) as a planar interface in between the oil and water-saturated rocks. However, in real life models, due to the presence of capillary effect, the interface between oil and water saturated rocks takes the form of an OWT zone. The oil saturation, and consequently resistivity value in an OWT zone decreases almost exponentially as a function of depth. Therefore, to simulate the real-life model problems, we need to be capable of modeling layers with arbitrary resistivity profiles.

Our proposed numerical 1.5D solver can consider layers with arbitrary resistivity distributions, which allows us to naturally simulate a reservoir which contains an OWT zone. The aforementioned physical consideration helps us to perform more realistic simulations and thus more accurately navigate through the reservoir, which may maximize its production.

We demonstrated that considering and OWC model may lead to a significant error in the inversion and navigation. The aforementioned error may direct the instrument towards a partially water-saturated rock. Hence, significantly reducing the posterior production from the reservoir. Considering an OWT

zone and an efficient method which can simulate it is vital to maximizing the reservoir production.

Deep Learning: In this work, we investigated the use of Deep Learning algorithms for inversion of borehole resistivity measurements.

In order to perform the inversion in real time, we require a rapid inversion method. The training stage of a Deep Neural Network (DNN) can be a time-consuming stage which can take 1-3 weeks to find a good approximation. However, we perform the training stage *offline*. Then, the *online* part of the method is faster than all other existing conventional inversion methods. Additionally, using Deep Learning, we can provide a reliable uncertainty quantification map. Thus, there is excellent potential in using Deep Learning for this application. However, exploring all possible venues and make a reliable inversion method using Deep Learning requires a tremendous amount of work and resources.

In addition to the advantages of Deep Learning, there are limitations. In order to train the system, we require a massive number of data. In the case of a 1.5D model problem, rapid solvers exist, which can produce the required data in a reasonable amount of time. However, in the case of 2D and 3D problems, producing the aforementioned training data set is extremely time-consuming. Moreover, because of the complexity of the problem and the number of variables in the case of 2D and 3D model problems, a much bigger data set is required compared to the case of a 1.5D model problem. Hence, more advances are needed to apply Deep Learning for inversion of 2D and 3D problems.

The mathematical knowledge in Deep Learning is limited. Hence, it does not exist a mathematically sound algorithm for the optimal design of the best DNN for a specific problem. Similarly, it is difficult to recognize a poorly designed DNN. Also, using a DNN, we can only compute a discrete version of the inversion function.

6.2. Future work

As future work, we plan to extend our method to other multi-physics problems, e.g., elasto-acoustic problems and to account for other material parameter distributions, such as cross-bedded formations. Also, we will investigate the optimal selection of the primary field. Moreover, we shall also integrate this simulator on an inversion software platform. A trivial parallelization of this software through operating frequencies and transmitters of a logging device and logging positions is straightforward. Additionally, the parallelization of the method through multiscale basis functions, fundamental fields, and correction

basis functions is under development, which will boost the speed of the method.

Furthermore, we shall employ the 1.5D solver as a primary field for 2.5D and 3D simulations to build accurate and fast numerical simulators. Moreover, it will be possible to combine OWT zones with the presence of geological faults.

The results presented in this work for Deep Learning are promising. However, extensive work is still needed in the field to achieve the required accuracy. As future work, we want to produce more advanced DNNs by using different activation functions, regularization, or a different norm for minimization. Furthermore, we want to investigate the use of Deep Learning for the design of measurement acquisition systems. We can use Deep Learning for each instrument configuration we design and observe the sensitivity of the desired design to the inversion variables. We shall also investigate the accuracy of the DNN for noisy data.

7. Main achievements

7.1. Peer-reviewed publications

2018 M. Shahriari, D. Pardo, A. Picon, A. Galdran, and J. Del Ser. ***Deep learning for the inversion of resistivity measurements.*** In progress.

2018 M. Shahriari, D. Pardo. ***Borehole resistivity simulations of oil-water transition zones with a 1.5D numerical solver.*** Submitted to Computational Geosciences, July 2018.

2018 T. Chaumont-Frelet, M. Shahriari, and D. Pardo. ***Adjoint-based formulation for computing derivatives with respect to bed boundary positions in resistivity geophysics.*** Submitted to Computational Geosciences, September 2018.

2018 M. Shahriari, S. Rojas, D. Pardo, A. Rodríguez-Rozas, S. A. Bakr, V. M. Calo, and I. Muga. ***A numerical 1.5D method for the rapid simulation of geophysical resistivity measurements.*** Geosciences, 8(6): 1–28, 2018.

7.2. Conferences talks

2018 M. Shahriari, T. Chaumont-Frelet, and D. Pardo. ***An adjoint-based method to compute derivatives with respect to bed boundary positions in resistivity measurements.*** ICSCG 2018, Prague, Czechia, September 2018.

2018 M. Shahriari, S. Rojas, D. Pardo, A. Rodriguez-Rozas, S. A. Bakr, V. M. Calo, and I. Muga. ***A fast multi-scale finite element method for geophysical resistivity measurements.*** ICSCG 2018, Prague, Czechia, September 2018.

2018 M. Shahriari, D. Pardo, Artzai Picón, Adrián Galdrán, Javier del Ser, and C. Torres-Verdín. ***Deep learning method for the rapid in-***

version of borehole resistivity measurements. Joint Industry Research Consortium on Formation Evaluation (Eighteenth Annual Meeting), Austin, TX, USA, August 2018.

2018 D. Pardo, M. Shahriari, J. A. Rivera, and C. Torres-Verdín. ***Update on the rapid inversion of LWD resistivity measurements in UTAPWeLS.*** Joint Industry Research Consortium on Formation Evaluation (Eighteenth Annual Meeting), Austin, TX, USA, August 2018.

2018 M. Shahriari, S. Rojas, D. Pardo, A. Rodriguez-Rozas, S. A. Bakr, V. M. Calo, I. Muga, and J. Muñoz. ***A fast 1.5D multi-scale finite element method for borehole resistivity measurements.*** ICCS 2018, Wuxi, China, June 2018.

2018 M. Shahriari, T. Chaumont-Frelet, and D. Pardo. ***Adjoint-based formulation for computing derivatives with respect to bed boundary positions in resistivity geophysics.*** Fifth International Congress on Multi-physics, Multi-scale, and Optimization Problems, Bilbao, Spain, May 2018.

2017 D. Pardo, A. Rodríguez-Rozas, Th. Chaumont-Frelet, M. Shahriari, and C. Torres-Verdín. ***Dimensionally adaptive inversion of LWD and deep azimuthal resistivity measurements. Part I: Lastest advances.*** Joint Industry Research Consortium on Formation Evaluation (Seventeenth Annual Meeting), Austin, TX, USA, August 2017.

2017 M. Shahriari, S. Rojas, D. Pardo, and I. Muga. ***An efficient 1.5D Galerkin method for geophysics.*** V-MAD7, Valparaiso, Chile, January 2017.

7.3. Proceedings and extended abstract

2018 M. Shahriari, D. Pardo, Artzai Picón, Adrián Galdrán, Javier del Ser, and C. Torres-Verdín. ***Deep learning method for the rapid inversion of borehole resistivity measurements.*** Joint Industry Research Consortium on Formation Evaluation (Eighteenth Annual Meeting), Austin, TX, USA, August 2018.

2018 D. Pardo, M. Shahriari, J. A. Rivera, and C. Torres-Verdín. ***Update on the rapid inversion of LWD resistivity measurements in UTAPWeLS.*** Joint Industry Research Consortium on Formation Evaluation (Eighteenth Annual Meeting), Austin, TX, USA, August 2018.

2017 D. Pardo, A. Rodríguez-Rozas, Th. Chaumont-Frelet, M. Shahriari, and C. Torres-Verdín. ***Dimensionally adaptive inversion of LWD and deep azimuthal resistivity measurements. Part I: Lastest advances.*** Joint Industry Research Consortium on Formation Evaluation (Seventeenth Annual Meeting), Austin, TX, USA, August 2017.

7.4. Seminars & workshops

2018 J. Omella, D. Pardo, M. Shahriari, M. Lezaun, A. Peña. ***Design optimization of electrical machines: an introduction.*** GKN Driveline, Zumaia, Spain, July 2018.

2018 M. Shahriari, D. Pardo, A. Picon, A. Galdran, J. Del Ser. ***Deep learning for inversion of resistivity measurements.*** Columbia University, New York, USA, July 2018.

2018 M. Shahriari, S. Rojas, D. Pardo, A. Rodriguez-Rozas, S. A. Bakr, V. M. Calo, and I. Muga. ***A fast 1.5D multi-scale method for geophysical measurements.*** P.hD. LIGHT Seminar, BCAM, Bilbao, Spain.

2018 M. Shahriari, S. Rojas, D. Pardo, A. Rodríguez-Rozas, and I. Muga. ***A fast 1.5D numerical solver for electromagnetics.*** AGH University, Krakow, Poland.

2017 M. Shahriari, V. M. Calo, S. Rojas, D. Pardo, and I. Muga. ***Reservoir characterization using dimensionally adaptive and multiscale methods.*** Workshop: "Multiscale Methods and Large-scale Scientific Computing", Changsha, China, August 2017.

2017 M. Shahriari, S. Rojas, D. Pardo, A. Rodríguez-Rozas, and I. Muga. ***A fast 1.5D numerical solver for electromagnetics.*** Workshop: "Geophysical Applications and HPC", Barcelona, Spain, June 2017.

7.5. Poster presentations

2018 M. Shahriari, D. Pardo, A. Picón, A. Galdrán, J. del Ser, and C. Torres-Verdín, *Geosteering using Deep Learning,* Oil & Gas Confernce 2018, Bilbao, Spain, October 2018.

A. Bessel Functions

Bessel functions are solutions of the following ordinary differential equation:

$$x^2y'' + xy' + (x^2 - m^2)y = 0,$$

where m is a parameter. Bessel functions exhibit multiple interesting properties (see, e.g., [1]). In this work, we employ the following ones:

$$\frac{2m}{\xi\rho}J_m(\xi\rho) = J_{m-1}(\xi\rho) + J_{m+1}(\xi\rho), \tag{A.1}$$

$$2\frac{\partial J_m(\xi\rho)}{\partial\,(\xi\rho)} = J_{m-1}(\xi\rho) - J_{m+1}(\xi\rho), \tag{A.2}$$

$$\int_0^{+\infty} J_m(\xi\rho)J_m(\xi_q\rho)\rho\,d\rho = \frac{1}{\xi_q}\delta(\xi,\xi_q). \tag{A.3}$$

Using (A.2) for the derivative of J_{m+1} and multiplying the result by ξ, we obtain:

$$\xi\frac{\partial J_{m+1}(\xi\rho)}{\partial\,(\xi\rho)} = \frac{\xi}{2}J_m(\xi\rho) - \frac{\xi}{2}J_{m+2}(\xi\rho). \tag{A.4}$$

By using (A.1) for J_{m+2}, we have:

$$J_{m+2}(\xi\rho) = \frac{2(m+1)}{\xi\rho}J_{m+1}(\xi\rho) - J_m(\xi\rho). \tag{A.5}$$

By substituting (A.5) into (A.4), we obtain:

$$\frac{m+1}{\rho}J_{m+1}(\xi\rho) + \xi\frac{\partial J_{m+1}(\xi\rho)}{\partial\,(\xi\rho)} = \xi J_m(\xi\rho). \tag{A.6}$$

Utilizing (A.2) for the derivative of J_{m+1}, we arrive at:

$$2\frac{\partial J_{m+1}(\xi\rho)}{\partial\,(\xi\rho)} = J_m(\xi\rho) - J_{m+2}(\xi\rho). \tag{A.7}$$

By substituting (A.7) into (A.6), we conclude:

$$\frac{m+1}{\rho}J_{m+1}(\xi\rho) = \frac{\xi}{2}J_m(\xi\rho) + \frac{\xi}{2}J_{m+2}(\xi\rho). \tag{A.8}$$

B. Deep Learning

B.1. Convolutional Neural Networks

A Convolutional Neural Network (CNN) [47] is a particular kind of neural network built by replacing fully-connected affine layers $\mathcal{N}$ by convolutional operators $\mathcal{C}$ defined by convolution kernels f. Hence, Equation (5.8) becomes:

$$\mathbf{I}_\theta(x) = (\mathcal{C}^{f^{(L)}} \circ \ldots \circ \mathcal{C}^{f^{(l)}} \circ \ldots \mathcal{C}^{f^{(2)}} \circ \mathcal{C}^{f^{(1)}})(x), \tag{B.1}$$

In a discrete setting, at layer l of Equation (B.1), operator $\mathcal{C}^{f^{(l)}}$ is determined by the set of convolutional kernels $f^{(l)} = \{f_s^{(l)}, s = 1, \ldots c_{j+1}\}$. Each of these kernels transforms an input tensor $x^{(l)}$ of dimension $h_l \times w_l \times c_l$ into an output $x_s^{(l+1)}$ of dimension $h_l \times w_l$. Each kernel is defined by a tensor of dimension $M_l \times N_l \times c_l$ that acts on its inputs through a simple convolution-like operation, followed by a non-linear function like the one in Equation (5.9):

$$x_s^{(l+1)}(h, w) = \mathbf{s}\left(\sum_{m=1}^{M_l}\sum_{n=1}^{N_l}\sum_{c=1}^{c_l} f_s^{(l)}(m, n) \cdot x^{(l)}(h + m, w + n, c)\right). \tag{B.2}$$

Application of all the c_{l+1} convolution kernels of $f^{(l)}$ on the input $x^{(l)}$ finally results into an output tensor $x^{(l+1)}$ of dimension $h_l \times w_l \times c_{l+1}$. Each of these convolutional layers $\mathcal{C}^{f^{(l)}}$ is followed by a non-linear point-wise function, and the spatial size of the output from each layer is decreased by a fixed projection operator $\mathcal{P}^{(l)} : \mathbb{R}^{h_l \times w_l} \to \mathbb{R}^{h_{l+1} \times w_{l+1}}$. Typically, $\mathcal{P}^{(l)}$ is defined as a local averaging operation. Eventually the dimensionality of the initial input x is transformed into that of an element of the target space.

B.2. Recurrent Neural Networks

Let us first consider a simple neural network with an input, an intermediate, and an output layer like the one defined in Section 5.2.1 as a directed graph in which nodes store the result of the operations described in Equation (5.8) and edges store the weights of the network W, b, as in Figure B.1a. Computations performed by such a network to obtain an output, given an input x,

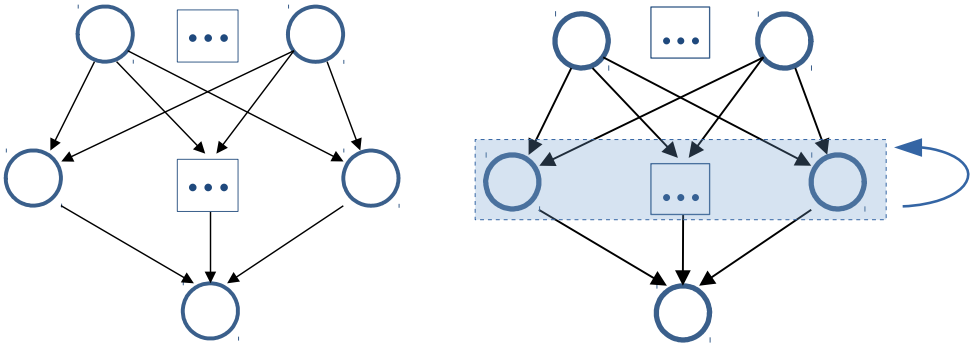

(a) Standard NN (b) Addition of a recurrent connection to (a)

Figure B.1.: Comparison between NN and RNNs

are described as:

$$\begin{aligned} z^{(1)} =& \mathbf{s}(a^{(1)}) = \mathbf{s}(W^{(1)} \cdot x + b^{(1)}), \\ \mathbf{I}_\theta(x) =& \mathbf{s}(W^{(2)} \cdot z^{(1)} + b^{(2)}), \end{aligned} \tag{B.3}$$

where $a^{(1)}$, also known as *activation*, denotes the output of the network at the first layer of this network before passing through the non-linearity $\mathbf{s}$. The critical difference between a regular Neural Network (NN) and a Recurrent Neural Networks (RNNs), as shown in Figure B.1b, is that the graph defining a NN is acyclical, whereas in a RNNs internal cycles are allowed. This introduces a notion of time or sequential dependency into the computations of the network.

In our case, we interpret a data sample as a temporal sequence of length T, $x = (x_1, x_2, ..., x_T)$, and the goal is to predict an output sequence ρ from x. In a RNNs, a regular NN is trained to predict $\rho = \mathbf{I}_\theta(x_t)$ out of x_t for $1 \leqslant t \leqslant T$, but the data is scanned left-to-right, and the previous activation is multiplied by a second set of learnable weights. Hence, the necessary computations within a RNNs for a forward pass are specified by the following two equations:

$$\begin{aligned} a_t &= W_{ax} x_t + W_{aa} a_{t-1} + b_a \\ \mathbf{I}_\theta(x_t) &= \mathbf{s}(W_{\rho a} a_t + b_\rho), \end{aligned} \tag{B.4}$$

where W_{ax} is a matrix of conventional weights between the input and the inner layer, W_{aa} is a matrix holding recurrent weights between the inner layer at time step t and itself at adjacent time step $t+1$, W_{ax} maps the result of the inner layer computations to the output $\mathbf{I}_\theta(x_t)$, and b_a, b_ρ are bias vectors allowing layers within the network to learn an offset. None of the weight matrices depend on the temporal component t and remain fixed, and the transition matrix W_{aa} of the RNNs is reset between processing two independent sequences.

The temporal nature of the process described in Equation (B.4) is better illustrated if operations are unfolded, as shown in Figure B.2. Following this representation, a RNNs can be interpreted not as cyclic, but as a standard network with one layer per time step and shared weights across time steps. It becomes clear that the network can be trained across many time steps using a variant of standard backpropagation algorithm, termed *backpropagation through time* [85, 34].

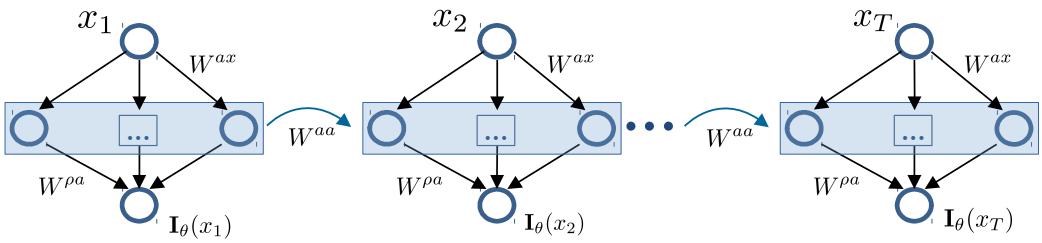

Figure B.2.: RNNs with computations unfolded through time.

From these first principles, many different flavors of RNNs have been successfully applied over time to temporal data. In this work, we make use of two significant advances in the field of RNNs, namely, Long-Short Term Memory RNNs (LSTM), and Bidirectional Recurrent Neural Networks (BRNNs).

LSTM networks [35] are similar to standard RNNs with one inner layer, but each ordinary node in this layer is replaced by a so-called *memory cell*. Each memory cell contains a node with a self-connected recurrent edge of fixed weight one, ensuring that the gradient can be propagated across many time steps without vanishing or exploding. BRNNs, introduced in [72], contain two layers, both linked to input and output. These two layers are different: the first has a recurrent connection from the past time steps while in the second, the direction of recurrent of connections is reversed, performing computations backward along the sequence. More details about both architectures can be found in [51].

B.3. Proposed Neural Network Architecture

The following is a description of the neural network architecture built in this work in the Keras framework [17]:

```
i = Input(shape=input_shape)
x = LSTM(recurrent_output_size)(i)
x2 = Reshape((recurrent_output_size,1))(x)
```

```
a = Conv1D(filters=nb_filter, kernel_size=3, activation='relu',
kernel_initializer=glorot_normal(),padding='same')(x2)
d = Conv1D(filters=nb_filter, kernel_size=3, activation='relu',
kernel_initializer=glorot_normal(),padding='same')(a)
x = Add()([x2,d])
x = MaxPooling1D(pool_length)(x)
a = Conv1D(filters=nb_filter, kernel_size=3,activation='relu',
kernel_initializer=glorot_normal(),padding='same')(x)
d = Conv1D(filters=nb_filter, kernel_size=3, activation='relu',
kernel_initializer=glorot_normal(),padding='same')(a)
x = Add()([x,d])
x = MaxPooling1D(pool_length)(x)
a = Conv1D(filters=nb_filter, kernel_size=3, activation='relu',
kernel_initializer=glorot_normal(),padding='same')(x)
d = Conv1D(filters=nb_filter, kernel_size=3, activation='relu',
kernel_initializer=glorot_normal(),padding='same')(a)
x = Add()([x,d])
x = MaxPooling1D(pool_length)(x)
x= Flatten(input_shape=input_shape)(x)
y =  Dense(num_outputs, activation='sigmoid',
kernel_initializer='glorot_uniform')(x)
```

Bibliography

[1] M. Abramowitz and I. A. Stegun. *Handbook of mathematical functions with formulas, graphs and mathematical tables*. National Bureau of Standard, 1964. (cited in page(s) 121)

[2] I. M. Abu-Shiekah, G. M. Warrlich, P. Goossens, D. M. Alexander, F. Zhu, and A. A. Al-Lamki. Shuaiba transition zone reservoirs: from modeling studies to field development challenges. *Representation of Capillary Pressure Hysteresis in Reservoir Simulation*, 2009. (cited in page(s) 73)

[3] I. Aizenberg, N. N. Aizenberg, and J. P. L. Vandewalle. *Multi-valued and universal binary neurons: theory, learning and applications*. Springer Science & Business Media, 2000. (cited in page(s) xi, 8)

[4] N. M. Al-Musharfi, R. Bansal, M. S. Ahmed, M. Y. Kanj, M. Morys, C. Conrad, and T. J. Parker. Real time reservoir characterization and geosteering using advanced high-resolution LWD resistivity imaging. *Society of Petroleum Engineers*, pages 1–11, 2010. (cited in page(s) vii, 1)

[5] J. Alvarez-Aramberri and D. Pardo. Dimensionally adaptive *hp*-finite element simulation and inversion of 2D magnetotelluric measurements. *Journal of Computational Science*, 18:95–105, 2017. (cited in page(s) vii, 1)

[6] M. Araya-Polo, T. Dahlke, C. Frogner, C. Zhang, T. Poggio, and D. Hohl. Automated fault detection without seismic processing. *Leading Edge*, 36(3):208–214, 2017. (cited in page(s) xii, 9)

[7] A. Aulia, A. Rahman, and J. J. Quijano Velasco. Strategic well test planning using random forest. *Society of Petroleum Engineers*, pages 1 – 23, 2014. (cited in page(s) xii, 9)

[8] S. A. Bakr, D. Pardo, and T. Mannseth. Domain decomposition Fourier FE method for the simulation of 3D marine CSEM measurements. *Journal of Computational Physics*, 255:456–470, 2013. (cited in page(s) vii, 1)

[9] R. Beer, L. C. T. Dias, A. M. V. da Cunha, M. R. Coutinho, G. H. Schmitt, J. Seydoux, and A. B. F. Guedes. Geosteering and/or reservoir characterization the prowess of new-generation LWD tools. *Society of Petrophysicists and Well-Log Analysts*, pages 1–14, 2010. (cited in page(s) vii, 1)

[10] C. Bell, J. Hampson, P. Eadsforth, R. Chemali, T. Helgesen, H. Meyer, C. Peveto, A. Poppitt, R. Randall, J. Signorelli, and T. Wang. Navigating and imaging in complex geology with azimuthal propagation resistivity while drilling. *Society of Petrophysicists and Well-Log Analysts*, pages 1–14, 2006. (cited in page(s) vii, viii, 1, 2, 71)

[11] B. Bhanu and A. Kumar. *Deep Learning for biometrics*. Springer, Switzerland, 2017. (cited in page(s) xii, 9)

[12] S. Bhattacharya, A. P. Byrnes, and P. M. Gerlach. Cost-effective integration of geologic and petrophysical characterization with material balance and decline curve analysis to develop a 3D reservoir model for pc-based reservoir simulation to design a waterflood in a mature Mississippian carbonate field with limited log data. Technical Report no. 2003-31, Kansas Geological Survey, Open-file Report, 2003. (cited in page(s) x, 6, 71, 73)

[13] M. Bittar, J. Klein, R. Beste, G. Hu, M. Wu, J. Pitcher, C. Golla, G. Althoff, M. Sitka, V. Minosyam, and M. Paulk. A new azimuthal deep-reading resistivity tool for geosteering and advanced formation evaluation. *Society of Petrophysicists and Well-Log Analysts*, pages 1–10, 2009. (cited in page(s) vii, viii, 1, 2, 71)

[14] N. Bize-Forest, L. Lima, V. Baines, A. Boyd, F. Abbots, and A. Barnett. Using machine-learning for depositional facies prediction in a complex carbonate reservoir. *Society of Petrophysicists and Well-Log Analysts*, pages 1 – 11, 2018. (cited in page(s) xii, 9)

[15] B. B. Bougher. Machine learning applications to geophysical data analysis. Master's thesis, The University of British Colombia, 2016. (cited in page(s) xii, 9)

[16] R. Chemali, M. Bittar, F. Hveding, M. Wu, and M. Dautel. Improved geosteering by integrating in real time images from multiple depths of investigation and inversion of azimuthal resistivity signals. *Society of Petrophysicists and Well-Log Analysts*, pages 1–7, 2010. (cited in page(s) vii, 1, 2, 71)

[17] F. Chollet. Keras. `https://github.com/fchollet/keras`, 2015. (cited in page(s) 125)

[18] R. L. Christiansen, M. J. Heymans, and J. R. Fanchi. Estimating oil reserves in oil-water transition zones. *Society of Petroleum Engineers*, 2000. (cited in page(s) 73)

[19] S. Constable and L. J. Srnka. An introduction to marine controlled-source electromagnetic methods for hydrocarbon exploration. *Geophysics*, 72 (2):WA3–WA12, 2007. (cited in page(s) vii, 1)

[20] S. Davydycheva. Separation of azimuthal effects for new-generation resistivity logging tools — part 1. *Geophysics*, 75(1):E31–E40, 2010. (cited in page(s) vii, 1, 2, 71, 77)

[21] S. Davydycheva. Separation of azimuthal effects for new-generation resistivity logging tools — part 2. *Geophysics*, 76(3):F185–F202, 2011. (cited in page(s) vii, 1, 2, 71)

[22] S. Davydycheva, D. Homan, and G. Minerbo. Triaxial induction tool with electrode sleeve: FD modeling in 3D geometries. *Journal of Applied Geophysics*, 67:98–108, 2004. (cited in page(s) vii, viii, ix, 1, 2, 6)

[23] S. Davydycheva and T. Wang. A fast modelling method to solve Maxwell's equations in 1D layered biaxial anisotropic medium. *Geophysics*, 76 (5):F293–F302, 2011. (cited in page(s) vii, viii, ix, x, xi, 1, 2, 6, 7, 8, 42)

[24] R. Dechter. Learning while searching in constraint-satisfaction-problems. *Proceedings of the Fifth AAAI National Conference on Artificial Intelligence*, pages 178–183, 1986. (cited in page(s) xi, 8)

[25] L. Demkowicz. Finite element methods for Maxwell's equations. In *Encyclopedia of Computational Mechanics Second Edition*, pages 1–20. American Cancer Society, 2017. (cited in page(s) x, 7, 11)

[26] R. Desbrandes and R. Clayton. Chapter 9 measurement while drilling. *Developments in Petroleum Science*, 38:251 – 279, 1994. (cited in page(s) 41, 76)

[27] G. T. Eigestad and J. A. Larsen. Numerical modelling of capillary transition zones. *Society of Petroleum Engineers*, 2000. (cited in page(s) 72)

[28] A. Erdozain, H. Barucq, D. Pardo, and V. Péron. *Fast inversion of 3D borehole resistivity measurements using model reduction techniques based on 1D semi-analytical solutions*. PhD thesis, Université de Pau et des Pays de l'Adour, Universidad del País Vasco-Euskal Herriko Unibertsitatea, 2016, 2016. (cited in page(s) vii, 1)

[29] M. Ghasemi, Y. Yang, E. Gildin, Y. Efendiev, and V. M. Calo. Fast multiscale reservoir simulations using pod-deim model reduction. *Society of Petroleum Engineers*, pages 1–18, 2015. (cited in page(s) x, 6, 73)

[30] P. W. J. Glover. Archie's law – a reappraisal. *Solid Earth*, 7(4):1157–1169, 2016. (cited in page(s) 71)

[31] T. Habashy and B. Anderson. Reconciling differences in depth of investigation between 2-MHz phase shift and attenuation resistivity measurements. *Paper E presented at the 1991 SPWLA Annual Logging Symposium, Midland, Texas, 16–19 June*, 1991. (cited in page(s) 41, 76)

[32] C. Hegde, S. Wallace, and K. Gray. Using trees, bagging, and random forests to predict rate of penetration during drilling. *Society of Petroleum Engineers*, pages 1 – 12, 2015. (cited in page(s) xii, 9)

[33] C. F. Higham and D. J. Higham. Deep learning: an introduction for applied mathematicians. *Computing Research Repository*, abs/1801.05894, 2018. (cited in page(s) xii, 9)

[34] S. Hochreiter, Y. Bengio, and P. Frasconi. Gradient flow in recurrent nets: the difficulty of learning long-term dependencies. In *Field guide to dynamical recurrent networks*. IEEE Press, 2001. (cited in page(s) 125)

[35] S. Hochreiter and J. Schmidhuber. Long short-term memory. *Neural Computation*, 9(8):1735–1780, 1997. (cited in page(s) 125)

[36] J. J. Hopfield. Neural networks and physical systems with emergent collective computational abilities. *Proceedings of the National Academy of Sciences of the United States of America*, 79(8):2554–2558, 1982. (cited in page(s) 88)

[37] K. Hornik. Approximation capabilities of multilayer feedforward networks. *Neural Networks*, 4(2):251–257, 1991. (cited in page(s) 86)

[38] O. Ijasana, C. Torres-Verdín, and W. E. Preeg. Inversion-based petrophysical interpretation of logging-while-drilling nuclear and resistivity measurements. *Geophysics*, 78 (6):D473–D489, 2013. (cited in page(s) vii, viii, ix, xii, 1, 2, 3)

[39] A. G. Ivakhnenko. *Cybernetic Predicting Devices*. CCM Information Corporation, 1973. (cited in page(s) xi, 8)

[40] K. Key. 1D inversion of multicomponent, multifrequency marine CSEM data: methodology and synthetic studies for resolving thin resistive layers. *Geophysics*, 74 (2):F9–F20, 2009. (cited in page(s) vii, xii, 1)

[41] K. Key. Is the fast Hankel transform faster than quadrature? *Computer Physics Communications*, 77 (3):F21–F30, 2012. (cited in page(s) viii, ix, 2, 6, 41)

[42] A. Kirscha and F. Hettlich. *The mathematical theory of time-harmonic Maxwell's equations*, volume 190. Springer, Switzerland, 2015. (cited in page(s) 11)

[43] J. Chee Leong Kok, J. DeJarnett, D. Geary, and E. Vauter. Successful geosteering in low resistivity contrast reservoirs of the permian basin. *Society of Petroleum Engineers*, pages 1 – 4, 2011. (cited in page(s) vii, 1, 2)

[44] J. A. Kong. *Electromagnetic wave theory*. Wiley-Interscience, 1986. (cited in page(s) 11)

[45] l. Hui, S. Yi-ze, and Z. Xi-fang. Numerical simulation of resistivity LWD tool based on higher-order vector finite element. *Journal of Petroleum Exploration and Production Technology*, 6(3):533–543, 2016. (cited in page(s) vii, 1, 2)

[46] D. J. Lary, A. H. Alavi, A. H. Gandomi, and A. L. Walker. Machine learning in geosciences and remote sensing. *Geoscience Frontiers*, 7(1):3 – 10, 2016. Special Issue: Progress of Machine Learning in Geosciences. (cited in page(s) xii, 9)

[47] Y. Lecun, L. Bottou, Y. Bengio, and P. Haffner. Gradient-based learning applied to document recognition. *Proceedings of the IEEE*, 86(11):2278–2324, 1998. (cited in page(s) 88, 123)

[48] R. Lehe, M. Kirchen, I. A. Andriyash, B. B. Godfrey, and J. L. Vay. Quasi-cylindrical and dispersion-free particle-in-cell algorithm. *Computer Physics Communications*, 203:66–82, 2013. (cited in page(s) ix, 6)

[49] P. Q. Lian, X. Q. Tan, C. Y. Ma, R. Q. Feng, and H. M. Gao. Saturation modeling in a carbonate reservoir using capillary pressure based saturation height function: a case study of the svk reservoir in the y field. *Journal*

of Petroleum Exploration and Production Technology, 6 (1):73–84, 2016. (cited in page(s) x, 6, 73)

[50] L. Liang, J. Zhu, F. Wang, J. Chen, T. M. Habashy, and A. Abubakar. In-situ estimation of relative permeability and capillary pressure from the joint inversion of array resistivity and formation test data. *Society of Petroleum Engineers*, 2017. (cited in page(s) 72)

[51] Z. C. Lipton, J. Berkowitz, and C. Elkan. A critical review of recurrent neural networks for sequence learning. 2015. (cited in page(s) 125)

[52] H. Liu. *Principles and applications of well logging*. Springer Geophysics. Springer-Verlag Berlin Heidelberg, 2017. (cited in page(s) 2, 40)

[53] L. O. Loseth and B. Ursin. Electromagnetic fields in planarly layered anisotropic media. *Geophysical Journal International*, 170:44–F80, 2007. (cited in page(s) ix, 6, 39)

[54] L. Lu, Y. Zheng, G. Carneiro, and L. Yang. *Deep Learning for computer vision: expert techniques to train advanced neural networks using TensorFlow and Keras*. Springer, Switzerland, 2017. (cited in page(s) xi, xii, 9)

[55] F. A. Malekzadeh and M. B. Dusseault. A solution for the transition zone isosats in two-phase primary drainage in the presence of gravity. *Computational Geosciences*, 17 (5):757–771, 2013. (cited in page(s) x, 6, 73)

[56] A. Martí. The role of electrical anisotropy in magnetotelluric responses: from modelling and dimensionality analysis to inversion and interpretation. *Surveys in Geophysics*, 35:179–218, 2014. (cited in page(s) vii, 1)

[57] S. K. Masalmeh and S. Oedai. Oil mobility in transition zone. *presented at the International Symposium of the Society of Special Core Analysts*, 2000. (cited in page(s) 72)

[58] P. R. McGillivray, D. W. Oldenburg, R. G. Ellis, and T. M. Habashy. Calculation of sensitivities for the frequency-domain electromagnetic problem. *Geophysics Journal International*, 116:1–4, 1994. (cited in page(s) 31, 33, 34)

[59] N. R. Morrow and C. C. Harris. Capillary equilibrium in porous materials. *Society of Petroleum Engineers*, 1965. (cited in page(s) 72)

[60] I. Muga and S. Ossandón. A method to compute the surface Green's function of piezoelectric half-space. *Scientia*, 13:84–91, 2006. (cited in page(s) ix, 6)

[61] F. Natterer. Adjoint methods as applied to inverse problems. In *Encyclopedia of Applied and Computational Mathematics*, pages 33–36. Springer Berlin Heidelberg, 2015. (cited in page(s) 6)

[62] J. C. Nédélec. *Acoustic and electromagnetic equations*, volume 144 of *Applied Mathematical Sciences*. Springer-Verlag, New York, 2001. Integral representations for harmonic problems. (cited in page(s) 11)

[63] D. Omeragic, T. Habashy, Y. H. Chen, V. Polyakov, C. Kuo, R. Altman, D. Hupp, and C. Maeso. Reservoir characterization and well placement in complex scenarios using LWD directional EM measurements. *Petrophysics*, 50:396–415, 2009. (cited in page(s) vii, 1, 77)

[64] D. Pardo, M. J. Nam, C. Torres-Verdin, M. G. Hoversten, and I. Garay. Simulation of marine controlled source electromagnetic measurements using a parallel Fourier *hp*-finite element method. *Computational Geosciences*, 15:53–67, 2011. (cited in page(s) vii, 1)

[65] D. Pardo and C. Torres-Verdin. Fast 1D inversion of logging-while-drilling resistivity measurements for the improved estimation of formation resistivity in high-angle and horizontal wells. *Geophysics*, 80 (2):E111–E124, 2014. (cited in page(s) vii, viii, ix, xii, 1, 2, 3, 4, 41)

[66] D. Pardo, C. Torres-Verdín, and M. Paszynski. Simulations of 3D DC borehole resistivity measurements with a goal-oriented *hp* finite-element method. Part 2: through-casing resistivity instruments. *Computational Geosciences*, 12(1):83–89, 2008. (cited in page(s) 52)

[67] R. E. Plessix. A review of the adjoint-state method for computing the gradient of a functional with geophysical applications. *Geophysical Journal International*, 167(2):495–503, 2006. (cited in page(s) 6, 32)

[68] M. Rabinovich, F. Le, J. Lofts, and S.Martakov. The vagaries and myths of look around deep resistivity measurements while drilling. *Petrophysics*, 53 (2):86–101, 2012. (cited in page(s) vii, 1)

[69] G. Richard, M. Monnereau, and J. Ingrin. Is the transition zone an empty water reservoir? inferences from numerical model of mantle dynamics. *Earth and Planetary Science Letters*, 205(1):37 – 51, 2002. (cited in page(s) 73)

[70] S. Rojas, I. Muga, and D. Pardo. A quadrature-free method for simulation and inversion of 1.5D direct current (DC) borehole measurements. *Computational Geosciences*, 20 (6):1301–1318, 2016. (cited in page(s) ix, 6)

[71] D. E. Rumelhart, G. E. Hinton, and R. J. Williams. Parallel distributed processing: explorations in the microstructure of cognition, Vol. 1. pages 318–362. MIT Press, Cambridge, MA, USA, 1986. (cited in page(s) 87)

[72] M. Schuster and K. K. Paliwal. Bidirectional recurrent neural networks. *IEEE Transactions on Signal Processing*, 45(11):2673–2681, 1997. (cited in page(s) 125)

[73] D. J. Seifert, S. Al Dossary, R. E. Chemali, M. S. Bittar, A. A. Lotfy, J. L. Pitcher, and M. A. Bayrakdar. Deep electrical images, geosignal, and real-time inversion help guide steering decisions. *Society of Petroleum Engineers*, pages 1–9, 2009. (cited in page(s) 77)

[74] J. Seydoux, E. Legendre, E. Mirto, C. Dupuis, J. M. Denichou, N. Bennett, G. Kutiev, M. Kuchenbecker, C. Morriss, and L. Yang. Full 3D deep directional resistivity measurements optimize well placement and provide reservoir-scale imaging while drilling. *Society of Petrophysicists and Well-Log Analysts*, pages 1–14, 2014. (cited in page(s) vii, 1)

[75] M. Shahriari, S. Rojas, D. Pardo, A. Rodríguez-Rozas, S. A. Bakr, V. M. Calo, and I. Muga. A numerical 1.5D method for the rapid simulation of geophysical resistivity measurements. *Geosciences*, 8(6):1–28, 2018. (cited in page(s) vii, viii, ix, 1, 2, 6)

[76] R. Streich and M. Becken. Sensitivity of controlled-source electromagnetic fields in planarly layered media. *Geophysical Journal International*, 187:705–728, 2011. (cited in page(s) vii, 1)

[77] A. Tarantola. *Inverse Problem Theory and Methods for Model Parameter Estimation*. Society for Industrial and Applied Mathematics, 2005. (cited in page(s) viii, ix, 3)

[78] A. M. Tehrani and E. Slob. Applicability of 1D and 2.5D marine controlled source electromagnetic modelling. *Geophysical Prospective*, 61:602–613, 2013. (cited in page(s) ix, 6)

[79] C. Vogel. *Computational Methods for Inverse Problems*. Society for Industrial and Applied Mathematics, 2002. (cited in page(s) viii, ix, 3)

[80] G. L. Wang, T. Barber, P. Wu, D. Allen, and A. Abubakar. Triaxial induction tool response in dipping and crossbedded formations. *Society of Exploration Geophysicists*, pages 585–590, 2014. (cited in page(s) vii, x, 1, 2, 6)

[81] Y. Wang, E. T. Chung S. W. Cheung, Y. Efendiev, and M. Wang. Deep multiscale model learning. *arXiv:1806.04830*, 2018. (cited in page(s) xii, 9)

[82] S. H. Ward and G. W. Hohmann. *Electromagnetic methods in applied geophysics: volume 1, theory*. Society of Exploration Geophysicists, 1987. (cited in page(s) 11)

[83] D. Watzenig. Bayesian inference for inverse problems- statistical inversion. *Elektrotechnik & Informationstechnik*, 124:240–247, 2007. (cited in page(s) viii, 3)

[84] W. T. Weller. Reservoir performance during two-phase flow. *Society of Petroleum Engineers*, 1966. (cited in page(s) 72)

[85] P. J. Werbos. Backpropagation through time: what it does and how to do it. *Proceedings of the IEEE*, 78(10):1550–1560, 1990. (cited in page(s) 125)

[86] D. Yu and L. Deng. *Automatic speech recognition: a Deep Learning approach*. Springer, London, 2017. (cited in page(s) xii, 9)

[87] C. Zhang, Q. Wu, X. Wang, and N. Lu. Application of rotary geosteering drilling in deep and thin reservoirs of tarim basin, NW China. *Petroleum Exploration and Development*, 40 (6):801 – 805, 2013. (cited in page(s) vii, 1, 2, 42)

[88] Z. Zhang, N. Yuan, and C. R. Liu. 1-D inversion of triaxial induction logging in layered anisotropic formation. *Progress In Electromagnetics Research B*, 44:383–403, 2012. (cited in page(s) ix, 4, 77)